University of Alberta

Shape-controlled palladium nanoparticles in catalytic hydrogenations

by

Ran Ma

A thesis submitted to the Faculty of Graduate Studies and Research
in partial fulfillment of the requirements for the degree of

Master of Science
in
Chemical Engineering

Department of Chemical and Materials Engineering

Spring 2011
Edmonton, Alberta

Abstract

Monodisperse Pd nanocubes of 20 nm rib length and Pd nanospheres of 3 nm diameter deposited on corundum were used as efficient tool to reveal structure sensitivity of three-phase hydrogenations of unsaturated alcohols. For an olefin alcohol hydrogenation in the kinetic regime, surface (100) atoms of the cubes displayed lower activity than other surface atoms of the spheres. Apparent activation energies of 23 kJ/mol for the cubes and 17 kJ/mol for the spheres confirmed the reaction structure sensitivity. In an acetylenic alcohol hydrogenation, the cubes showed higher selectivity to an olefinic product than the spheres. Apparent activation energy was found as 38 kJ/mol for the cubes and 24 kJ/mol for the spheres. The apparent structure sensitivity in this case was attributed to liquid-solid mass transfer limitations governing the sphere-catalyzed reactions. The study shows the applicability and limitations of the use of nanoparticles for structure sensitivity studies in catalysis.

Acknowledgment

The financial support from the Faculty of Engineering at the University of Alberta and NSERC (Discovery Grant) is highly appreciated. I would like to express my gratitude to my supervisor Dr. Natalia Semagina who has been always helpful and offered me invaluable advice, support, assistance, and guidance through out the project. I'd also like to thank Tong Qiu for BET surface area analysis, Dr. Dimitre Karpuzov (ACSES, University of Alberta) for XPS analysis, Julie Qian (National Institute for Nanotechnology, Edmonton) for recording an HR-TEM image and Shalon McFarlane (University of Alberta) for EDX analysis.

Table of contents

List of figures

List of tables

Nomenclature

a_s	The external specific surface area of catalyst, m^2/g_{cat}
A*p*	Catalyst particle surface area, m^2
Ca	Carberry number
C_b	The bulk concentration of a reagent, mol/m^3
C_{H2}^*	Hydrogen saturation concentration in liquid phase, mol/m^3
$C_{H2,G}$	Hydrogen concentration at gas phase, mol/m^3
C_s	Reactants' concentrations at the catalyst surface, mol/m^3
$C_{Y,b}$ $C_{H2,b}$	Liquid bulk concentration, mol/m^3
$C_{Y,S}$ $C_{H2,S}$	Catalyst surface concentration, mol/m^3
d	Crystal size, nm
d_p	Particle diameter, μm
D	Dispersion
$D_{A,B}$	Molecular diffusivity of component A into component B, m^2/s
D_{eff}	Effective diffusivity, m^2/s
k	Rate constant
K	Equilibrium constant
K	Shape factor, a constant usually taken as 0.9
k_{LS}	The liquid solid mass transfer coefficient, m/s
l	Impeller diameter, *m*
L	Characteristic length, m
M	Molecular weight, g/mol
m_p	Particle mass, g
n	Angular velocity, rad/s
N_s	Number of surface atoms
N_t	Number of total atoms

N_p	The power number
p	Pressure
S	Selectivity
Sc	Schmidt number
Y	Yield
r	Reaction rate, mol $_{H2}$/ mol $_{Pd}$/min
r_{obs}	Observed reaction rate, mol/s·g_{cat}
R	Reaction rate, mol/(gcat·s)
Sh	Sherwood number
t	Time
T	Temperature, K
V	Volume, m^3
V_A	Molar volume of A at its normal boiling temperature, m^3/kmol
w	Mass fraction, %
x	Molar fraction
x_B	Solvent association factor
X	Conversion
*	Active site

Subscripts

A	MBA
E	MBE
Y	MBY
int	Initial
i	Component
H2	Hydrogen
p	Particle

Greek letters

ε	Catalyst porosity
λ	The wavelength of x-rays, nm
β	The line broadening at half the maximum intensity in radians of 2θ
θ	Surface coverage
θ	The Bragg diffraction angle
δ_{G-L}	Gas-liquid diffusion film thickness, m
δ_{L-S}	Liquid-solid diffusion film thickness, m
ρ	Density, g/cm^3
μ	Viscosity, Pa·s

Abbreviations

AA	Ascorbic acid
AAS	Atomic Absorption Spectroscopy
AOT	Sodium bis(2-ethylhexyl)sulphosuccinate
CTAB	Cetyltrimethylammonium bromide
ER	Eley-Rideal mechanism
FID	Flame ionization detector
f.c.c.	Face center cubic
GC	Gas chromatograph
G-L	Gas-Liquid
HR-TEM	High resolution transmission electronic microscopy
IUPAC	International Union of Pure and Applied Chemistry
LH	Langmuir-Hinshelwood mechanism
MBA	2-methylbutan-2-ol
MBE	2-methyl-3-buten-2-ol

MBY	2-methyl-3-butyn-2-ol
PAMAM	Poly(amidoamine)
PEGDE	Pentaethyleneglycol dodecyl ether
PPI	Poly(propylene imine)
PVP	Poly(N-vinyl-2-pyrrolidone)
TEM	Transmission electronic microscopy
TOF	Turnover frequency, s^{-1}
w/o	Water-in-oil
W_M	Wheeler-Weisz modulus
XRD	X-Ray Diffraction
XPS	X-ray photoelectron spectroscopy

Chapter 1. Introduction

In the past decades, nanotechnology has become a popular field for research and development. In particular, heterogeneous catalysis was cited as a successful application that has great benefit for society.[1] The recent advances in nanotechnology coupled with fundamental understanding of the techniques and phenomena, have opened unprecedented opportunities for catalysis. Heterogeneous catalytic reactions are controlled by the atomic-scale structure and composition of the surface and the interaction of surface sites with reactant molecules.[2] Therefore, it is possible to change the performance of a metal catalyst by tailoring its size and shape. The goal is still to prepare catalysts to optimize their properties by custom designed active sites and site environments for perfect selectivity and desirable activity.[1]

Nanoparticles with controlled size and shape have been synthesized successfully and studied in some industrially relevant catalytic reactions.[3-6] Among them, most of the studies were done on size-controlled "spherical" (cuboctahedral) nanoparticles, for which surface statistics is well known.[7] However, the variety of surface atoms of a sphere which include (111) and (100) terrace atoms, edge and vertices atoms makes the correlation between the catalytic activity and specific atoms not always straightforward. It is known that activity can be influenced by nanoparticles' size, but selectivity is most sensitive to the packing of atoms on the surface or the exposed facets of a nanoparticle.[8] Recent studies show that catalytic activity also depends on the particle's shape. A successful example is the use of Pt tetrahedrons in a Suzuki reaction, in which Pt spheres do not display any activity.[9] Therefore, an increased attention has been drawn to the catalytic studies of nanoparticles of controlled shape. The nanoparticle shape determines which crystal facets comprise the surface of a

nanocrystal. If a reaction requires (100) terrace atoms to proceed, the best nanostructure would be a cubic crystal with only (100) atoms as terrace atoms, while (111)-demanding reactions would proceed the most efficiently on tetrahedral particles with only (111) surface atoms. The shape also determines the number of atoms located at the edges or corners, which have critical effect on catalytic performance. A recent study of hydrogenation over Pt nanocubes and nanopolyhedra with tunable size from 5 to 9 nm showed the similar catalytic activity as compared to Pt single crystal for ethylene hydrogenation, but the nanocubes showed significant higher product selectivity as compared to nanopolyhedra during pyrrole hydrogenation.[10] This example shows the importance of size and shape control of nanoparticles for catalytic research.

The hydrogenation of carbon-carbon double and triple bonds is one of the fundamental reactions for synthesis and manufacture of fine and industrial chemicals. Recently, researchers have attempted to study the structure sensitivity and selectivity of catalytic hydrogenation of unsaturated alcohols using spherical palladium nanoparticles. Palladium-based catalysts have been widely used for catalytic hydrogenations due to their extraordinary activity and chemo-selectivity.[11] For example, one study of allyl alcohol hydrogenation on Pd nanoparticles of 1.5-1.9 nm shows that the terrace atoms are active sites,[12] while another indicates defect, not face, atoms as active sites for the particles from 2.6 to 5.1 nm.[13] The latter study also showed that selectivity in the hydrogenation of unsaturated alcohol is extremely sensitive to the particle diameter as selectivity increases with decreasing average particle size.[13]

To the best of our knowledge, structure sensitivity studies of an olefinic and acetylenic alcohol hydrogenation using well-defined nanoparticles of different shapes have not been attempted yet. At the same time, they can result in valuable knowledge on the reaction active sites in the absence of materials and pressure

gaps, which is often difficult to obtain using spherical particles with complex surface composition.[13]

In the present study, we focus on Pd-catalyzed three-phase hydrogenation of 2-methyl-3-buten-2-ol (MBE) to 2-methylbutan-2-ol (MBA) and 2-methyl-3-butyn-2-ol (MBY) to MBE (Fig. 1.1) to study the reaction structure sensitivity under industrially-relevant conditions. The intermediate MBE is the target product for MBY hydrogenation and is used in the production of vitamins A and E and perfumes.

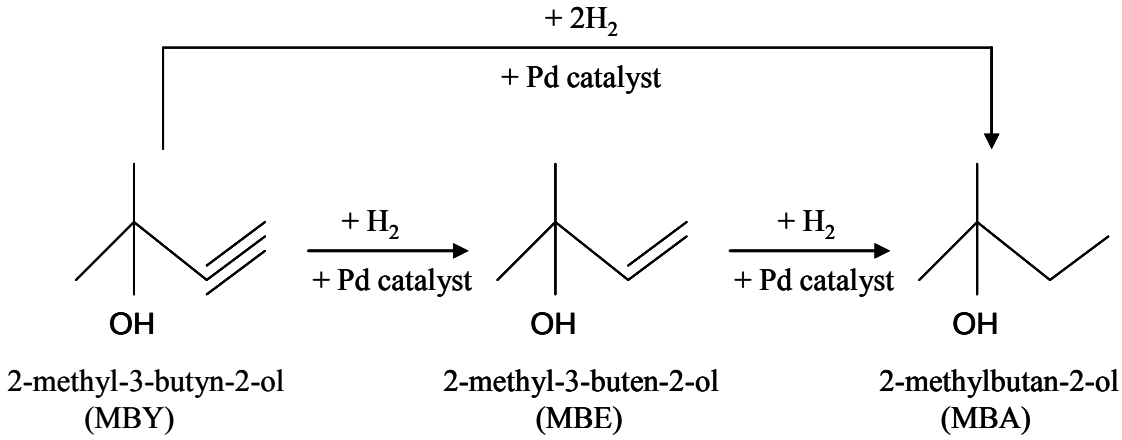

Figure 1.1. Reaction scheme of hydrogenation of MBY and MBE.

Before the catalytic studies, we will aim to synthesize Pd nanoparticles with controlled sizes and shapes, so that the structure-activity correlations can be established. After initial nanoparticle prescreening for shape and size monodispersity, the catalytic studies will be carried out using well-defined Pd spherical and cubic nanoparticles prepared with cetyltrimethylammonium bromide (CTAB) as a stabilizing agent. One stabilizing agent should be selected for both nanostructures as it can affect the catalytic behavior.[14-15] Some

stabilizers may deactivate active sites, e.g., Pt nanoparticles prepared with TTAB exhibit much higher activity than polyvinylpyrrolidone-capped Pt nanocrystals.[16] In order to elucidate the activities of (100), (111) planes and defect (edges and vertices) atoms, cubes of ~20 nm rib size will be used, as ~98% of their surface consists of (100) terrace atoms, along with 3 nm spherical particles that possess well-represented (111), (100) surfaces and defect atoms, as opposed to smaller particles with larger fraction of edges and vertices. The type and relative amount of surface atoms will determine the catalytic behavior of the nanoparticles, which could be optimized for achieving the highest selectivity and activity. As three-phase hydrogenation kinetics can be limited by gas-liquid and liquid-solid mass transfer, the reaction regimes will be addressed to distinguish between intrinsic and apparent structure sensitivity due to the mass transfer limitations.

Chapter 2. Background

2.1 Three-phase catalytic hydrogenations

2.1.1 Structure sensitivity of catalytic reactions

In catalysis, turnover frequency (TOF) corresponds to the number of molecules of reactants converted in unit time over one active site. It is a measure of the intrinsic activity of a catalytic site. If the reaction conditions in kinetic regime are fully described, together with the method of counting of sites, TOF value can provide meaningful comparison between various catalysts. Thus, TOFs must be reported whenever possible in any proper catalytic study.[17]

Structure sensitivity of a heterogeneous catalytic reaction involves a substrate adsorption followed by its chemical transformation on an active site.[5] The information about geometric and electronic properties of surface atoms is necessary to understand nanoparticle physical and chemical properties. The electronic structure refers to nanoparticles valence, band structure, size dependence of these properties, and geometric structure represents the size of the particles, crystallographic phase, and composition.[18] It is believed that the electronic and geometric properties of active sites affect the catalytic behavior. The electronic or "ligand" effect refers to the change of the nature of chemisorption bond when atoms surrounding a metal atom on the surface are replaced by other atoms.[19] Sabatier principle states that the intermediate formed by a reactant at the metal surface must be adsorbed strongly enough to be formed, but not too strong for the product to get dissociated. The relative ratio of various types of surface atoms changes substantially with varying particle size and shape. The geometric or "ensemble" effect implies that the adsorption of reactant sometimes needs multiple atoms with a specific arrangement.[5] TOF is used to

measure the nanostructure activity for structure sensitivity studies. The difficulty in calculating a TOF is not only in measuring the reaction rates in kinetic regime, but in counting active sites. There are several ways to obtain TOF which include using the active particle metal dispersions determined by CO and / or H_2 chemisorptions, or the total surface atom number estimated using metal crystal statistics and particle size found by electron microscopy or X-ray diffraction.[5] For some reactions on metal surface, the catalytic activity only depends on the total number of nanoparticle surface atoms, such reactions are considered as structure insensitive reactions.[17] The TOFs of these reactions are independent of nanoparticle size and shape. For other reactions, the TOF is much greater on certain surface sites, and not all the surface atoms are involved for active site. The activity can be dependent on metal nanoparticle size, crystal plane, or defect structures. These reactions refer as structure sensitive reactions.[17] The TOF for this kind of reaction varies with particle size and shape.

Structure sensitivity was first studied using model catalysts (single crystals) typically under ultra-high vacuum. As an example, n-hexane skeletal rearrangement was studied over different platinum single crystal surfaces, the activity and selectivity of aromatization reactions both change with surface structure.[20] In heterogeneous reactions, the catalyst may contain more than one type of active sites; therefore, the calculated TOF represents the average value of the overall catalyst activity. Recent structure sensitive studies were based on size effect studies using near spherical nanoparticles of different size, since the percentage of surface atom types (terrace, vertex, and edge atoms) varies with changing particle sizes. It is possible to estimate the amount of atoms with different electronic and geometric properties by applying surface statistics. Then TOF can be calculated as per specific atoms. Importantly, such studies can be carried out with real well-defined nanoparticles under industrially-relevant

conditions, i.e., without materials and pressure gaps dominating the catalytic science for decades.

In general, the carbon-carbon double bond is the most readily hydrogenated among the functional groups.[11] The reaction structure sensitivity is still debatable. Some studies of heterogeneously catalyzed hydrogenations of alkenes show their structure insensitivity.[21-23] As an opposite example for alkene hydrogenation, Amiridis et al.[24] investigated the structure sensitivity of propene hydrogenation over bimetallic Au-Pt/TiO_2 catalyst. Comparing catalysts prepared by either co-impregnation or from a heterobimetallic precursor, the initial TOFs differed by 2-3 orders of magnitude indicating the reaction structure sensitivity. Another study of allyl alcohol hydrogenation over Pd nanoparticles 1.5-1.9 nm diameter showed the reaction kinetics depended primarily on the particle's geometric properties[12], indicating the reaction was structure sensitive. The hydrogenation of alkynes is generally considered as structure sensitive reaction. Catalytic hydrogenation of 2-butyne-1, 4-diol was studied over shape-controlled Pd nanoparticles.[15] Cubic Pd nanoparticles stabilized by PVP were compared to spherical particles produced by radiolytic reduction. Pd cubes were more active and selective in the hydrogenation revealed its structure sensitivity. Semagina et al.[25] studied the structure sensitivity of solvent free hydrogenation of MBY over AOT-stabilized Pd nanoparticles of 6, 8, 11, and 13 nm in diameters. They suggested the reaction was structure-sensitive but size-independent, and facet (111) was the active sites as TOF in terms of number of specific atoms on Pd (111) facets remains constant with increasing particle size.

2.1.2 Selectivity in hydrogenations

Various parallel and consecutive reactions occur on the surface of heterogeneous catalysts, deteriorating selectivity to a desired product. The selectivity can be influenced by changing the nature of the catalyst, including its crystallographic orientation. One example is that for reaction with MoO_3, the (010) face is not selective for propene oxidation, but the (100) face gives acrolein.[26]

Hydrogenations of the carbon-carbon triple bonds to the selective formation of double bonds have been addressed since the very early stage of catalytic hydrogenation studies. The intermediate olefins are usually formed selectively as long as acetylene remains accessible due to the stronger adsorption of acetylenes as compared to that of olefins. The strongly adsorbed acetylenes may effectively displace the olefin formed on the catalyst surface to prevent their further hydrogenation to saturated compound[11] and block its re-adsorption. To obtain high selectivity, hydrogenation of olefin must be stopped after complete hydrogenation of acetylenes. It is important to design catalysts with high selectivity for the desired product without sacrificing activity. The reactively adsorbed acetylenes also form multiple bond intermediates and are hydrogenated to saturated compounds directly.[19] Therefore, reaction parameters and the morphological properties of catalyst are critical for the overall selectivity.

2.1.3 Langmuir isotherms

Adsorption of reactants on the surface of the catalyst is an important step in every reaction of heterogeneous catalysis, and is usually described using isotherms, which provide the amount of adsorbate as a function of its pressure (gas, p) or concentration (liquid, C) at constant temperature. The Langmuir isotherm usually describes the dependence of the surface coverage (θ) of an adsorbed gas on the pressure of the gas above the surface at a fixed temperature. The surface coverage may be increased by raising the gas pressure but will be

reduced if the surface temperature is raised.

There are four assumptions for the Langmuir isotherms, although they are not satisfied for many real-life cases, especially in chemisorption.

1. All surface sites have the same adsorption energy for the adsorbate.
2. Adsorbed molecules do not interact with each other.
3. All adsorption occurs through the same mechanism.
4. Only one layer of molecules can be adsorbed at the maximum adsorption (monolayer).

Langmuir adsorption isotherms can be derived for molecular, dissociative and competitive adsorption.

Associative adsorption[27]

If the adsorbed molecules are in equilibrium with the gas phase, the reaction equation may written as

$$A + * \xleftrightarrow{K_A} A*, \quad \text{where} \quad K_A = \frac{k_A^+}{k_A^-} \tag{1}$$

where * represents the active sites on catalyst surface, A represents a molecule, k^+ and k^- are the forward (adsorption) and backward (desorption) rate constants, and K is the equilibrium constant.

At steady state, the surface coverage with A can be expressed as:

$$\frac{d\theta_A}{dt} = p_A k_A^+ (1 - \theta_A) - k_A^- \theta_A = 0 \tag{2}$$

where the first term is due to adsorption and the latter to desorption, θ represents the surface coverage, p is the pressure of a gas (using C for concentration of a liquid). The Langmuir adsorption isotherm for associative adsorption of a single gas molecule (such as CO, NH_3, and NO which do not decompose upon

adsorption) can be written as

$$\theta_A = \frac{K_A p_A}{1 + K_A p_A} \tag{3}$$

Dissociative adsorption[27]

Molecules such as H_2 and O_2 adsorb dissociatively, and in general equilibrium between the adsorbed atoms and the molecules in the gas phase can be assumed. The reaction equation can written as

$$A_2 + 2* \xleftrightarrow{K_A} 2A*, \qquad \text{where} \quad K_A = \frac{k_A^+}{k_A^-} \tag{4}$$

At steady state

$$\frac{d\theta_A}{dt} = p_A k_A^+ (1-\theta_A)^2 - k_A^- \theta_A^2 = 0 \tag{5}$$

and the Langmuir adsorption isotherm for dissociative adsorption can be rearranged as

$$\theta_A = \frac{\sqrt{K_{A_2} p_{A_2}}}{1 + \sqrt{K_{A_2} p_{A_2}}} \tag{6}$$

Competitive adsorption[27]

This section considers the case when there are two distinct species of adsorbates present in the system. If the two species A and B compete for the same adsorption site, the reaction equation can be consider as

$$A + * \xleftrightarrow{K_A} A* \tag{7}$$

$$B + * \xleftrightarrow{K_B} B* \tag{8}$$

And the equilibrium equations are

$$\theta_A = K_A p_A \theta_* \quad , \qquad \theta_B = K_B p_B \theta_* \tag{9}$$

Because $\theta_A + \theta_B + \theta_* = 1$, the respective coverage can be rearranged as

$$\theta_A = \frac{K_A p_A}{1 + K_A p_A + K_B p_B} \tag{10}$$

$$\theta_B = \frac{K_B p_B}{1 + K_A p_A + K_B p_B} \tag{11}$$

2.1.4 Catalytic reactions and mechanisms

A catalytic process is a sequence of elementary steps that form a cycle from which the catalyst exits unaltered. In the case of heterogeneous reactions, the surface chemical reaction is a part of a heterogeneous catalytic process, which also involves reactant and product diffusion and their adsorption and desorption.

The catalytic hydrogenations occur on the surface of the metal catalyst. In the case of alkene hydrogenation, both hydrogen and alkene adsorb on the surface. First, the reactant molecules undergo physical adsorption, during which van der Waals forces of attraction binds the molecule to the surface. If the molecules lose energy upon interaction with the surface, it may be trapped in the weak attractive potential and become physically adsorbed on the surface without dissociation.[27] This step is reversible and desorption can rapidly occur.[26] The physical adsorption reduces the energy of activation of the subsequent chemical adsorption. In the case of dissociative chemisorption of hydrogen molecules, relatively strong H-H bond is broken and replaced with two weak metal-H bonds. The strong bond requires that the H_2 molecule be separated into atoms, and the energy of achieve dissociation is quite high. It would be difficult to achieve chemisorption if the molecule had to first dissociate and then approach the metal atom, but this difficulty disappears when the H_2 molecule is first physically adsorbed and then chemisorbed dissociately.[28] Alkene molecules are adsorbed on the catalyst surface via non-dissociative adsorption. The π bond of alkene breaks and interacts with d-orbitals of the active metal. If a hydrogen atom diffuses close to the bound

carbons, the hydrogen atom forms a bond with one of the carbons of the double bond. Similarly, another hydrogen atom replaces the other carbon-metal bond with a carbon-hydrogen bond. The alkane now dissociates from the metal surface. There is space on catalyst surface for new hydrogen and alkene molecules to go through the whole process again. The hydrogenation of alkynes is similar to the one of alkenes.

In heterogeneous catalysis, there are two main reaction mechanisms which have been proposed: the Langmuir-Hinshelwood (LH) and the Eley-Rideal (ER).[26] In the LH mechanism, two reacting molecules are both adsorbed on the catalyst surface before the reaction take place, whereas in the ER mechanism, only one of the molecules adsorbs and the other one reacts with it directly from the bulk phase without adsorbing. Most reactions have kinetics that is consistent with the first model. The hydrogenations of MBE and MBY on Pd surface are known to follow the LH mechanism.[29] The rate-determining step (RDS), which is the slowest step in a consecutive multi-step reaction mechanism that determines the overall rate for each reaction, is assumed to be the addition of the second hydrogen atom to half-hydrogenated species to comply with typically observed first order to H_2. According to the LH mechanism, the elementary steps of the catalytic reaction between MBE and H_2 can be written as:

(1) $MBE + * \xleftarrow{K_{MBE}} MBE*$

(2) $H_2 + 2* \xleftarrow{K_H} 2(H*)$

(3) $MBE* + H* \xleftarrow{K_{MBE-H}} (MBE-H)* + *$

(4) RDS: $(MBE-H)* + H* \xrightarrow{k_1} MBA* + *$

(5) $MBA* \xleftarrow{1/K_{MBA}} MBA + *$

The rate expression is determined by the RDS [29] as shown in Eq. 12:

$$r_1 = k_1\theta_{MBE-H}\theta_H = \frac{k' K_{MBE} K_H C_{MBE} C_{H_2}}{(1 + K_{MBE}C_{MBE} + K_{MBA}C_{MBA} + K_H^{1/2}C_{H_2}^{1/2})^2} \quad (12)$$

Similarly, the elementary steps of the MBY hydrogenation can be represented as:

(1) $MBY + * \xleftrightarrow{K_{MBY}} MBY*$

(2) $H_2 + 2* \xleftrightarrow{K_H} 2(H*)$

(3) $MBY* + H* \xleftrightarrow{K_{MBY-H}} (MBY-H)* + *$

(4) RDS: $(MBY-H)* + H* \xrightarrow{k_2} MBE* + *$

(5) $MBE* \xleftrightarrow{1/K_{MBE}} MBE + *$

The rate expression is determined by the RDS as:

$$r_2 = k_2\theta_{MBY-H}\theta_H = \frac{k'' K_{MBY} K_H C_{MBY} C_{H_2}}{(1 + K_{MBY}C_{MBY} + K_{MBE}C_{MBE} + K_H^{1/2}C_{H_2}^{1/2})^2} \quad (13)$$

2.1.5 Metal catalyst and support

The platinum group metals (ruthenium, rhodium, palladium, osmium, iridium and platinum) have the widest application because of their high catalytic activity,[2] and they have all been used as hydrogenation catalysts. Particularly, platinum and palladium have been the most widely used catalysts since the earliest stages of the catalytic hydrogenation history.[11] Palladium catalyst is active under very mild conditions. It can be applied in liquid-phase hydrogenation at room temperature and atmospheric pressure of hydrogen. More importantly, palladium appears to be by far the most selective metal to achieve selective semi-hydrogenations.[19] For instance, the selectivity in acetylene hydrogenation decreased with respect to

catalyst metal in the following order: Pd >> Rh ≥ Pt > Ru >> Ir >Os.[11]

Metal catalyst can be employed as both unsupported fine particles per se and supported on a carrier material. Unsupported catalysts are seldom employed due to separation difficulties[11] and high-temperature instability. In the supported catalysts, the support provides high surface area to well disperse the primary catalyst. The support allows the active component to have a larger exposed surface area, and acts as an inert or a secondary catalyst for the reactions. Furthermore, supported catalysts are more stable. In this study, supported catalysts were employed most of the time.

A variety of methods have been employed for preparing supported catalysts depending on the nature of metal catalyst and carrier. These techniques include impregnation, deposition, co-precipitation, ion exchange, and metal vapor deposition.[30] Usually, materials that are thermally stable and chemically relatively inert can be used as support. In some catalysts, strong metal-support interactions may occur. As an example, ZnO has been used as support for Pd catalyst, and PdZn alloy was formed during the catalyst high-temperature reduction, resulting in suppressed MBE hydrogenation during MBY hydrogenation.[31] For the structure sensitivity studies, strong metal-support interactions should be avoided to evaluate intrinsic activity of the active metal. The supports which do not form alloy phase with Pd are Al_2O_3, Kieselguhr, SiO_2, zeolite, and activated carbon. α-Al_2O_3 was chosen as the catalyst support for this study, which is also non-porous, so that internal mass transfer limitations can be excluded.

2.1.6 Catalyst deactivation in liquids

According to IUPAC,[32] catalyst deactivation is a phenomenon when the conversion in a catalytic reaction performed under constant conditions decreases

with time of run or time on stream. Catalyst deactivation is a result of a number of unwanted chemical and physical changes. The main causes of catalyst deactivation in liquid phase reaction are particle sintering, metal and support leaching, deposition of inactive metal layers or polymeric species, and poisoning by strongly adsorbed species.[33] They may occur separately or in combination, but the net effect is always the removal of active sites from the catalytic surface.

Sintering. Most liquid reactions are carried out at relatively low temperature, sintering due to temperature driven migration and coalescence of metal particles on support is unlikely for supported metal catalysts.[33] However, sintering may occur close to room temperature through atomic migration process (Ostwald ripening).[33] According to IUPAC, Ostwald ripening is the dissolution of small crystals or sol particles and the redeposition of the dissolved species on the surfaces of larger crystals or sol particles. The main consequence of Ostwald ripening is the disappearance of most of the smallest crystals, and the number of crystals decreases while the mean size increases. Ostwald ripening is a spontaneous process that occurs because larger crystals are more energetically favored than smaller crystals.[34] Small crystals are kinetically favored while large crystals are thermodynamically favored. Small particles can be formed easily as nuclei; however, a large number of small particles have more interfacial area than one large particle with the same volume. Moreover, atoms on the surface are energetically less stable than the ones already well ordered and packed in the interior. As the system tries to lower the overall energy, atoms on the surface of small particles will tend to detach from it, and diffuse into the solution. As more small particles do this, the concentration of free atoms in solution eventually reaches supersaturation, and then the free atoms have a tendency to condense on the surface of larger particles.[34] Thus, large particles grow at the expense of

dissolving smaller particles, which is the process of Ostwald ripening. Previous studies[14, 35] have showed Pd nanoparticles grew larger after the first cycle of reaction due to the Ostwald ripening in C-C coupling reactions.

Leaching of active phase. This is the main cause of catalyst deactivation in liquid phase reactions. For metal catalysis, the leaching of nanoparticles from the support, or metal atoms from the nanoparticles mainly depends on the reaction medium and surface metal properties. Sometimes, the loss of metal from catalysis is mainly due to support leaching, i.e. partial support dissolution.[33]

The leaching of Pd atoms and/or ions is a key issue in C-C coupling reactions, such as Heck, Suzuki, and Sonogashira reactions. As contrary to Ostwald ripening process, a study showed the particle size decreased during the reaction indicating that Pd atoms and/or ions are leaching out of the clusters.[36] Many studies proposed the leached Pd species are the true catalysts in Pd supported nanoparticle catalyzed C-C coupling reactions.[36-40] When the substrate is consumed, these leached homogeneous species can re-cluster to form new (smaller) particles. It was also proposed that Pd leaching from Pd nanoparticles in solution provides the basis for a homogeneous mechanism followed by recombination of these atoms with Pd nanoparticle reservoir.[38] Alkyne and alkene hydrogenations on metal surfaces, however, are known to be heterogeneously catalyzed.

Deposition of inactive metal or polymeric species. Noble metals can be deactivated by the deposition of a less active or totally inactive metal. Polymeric or oligomeric species formed in secondary reactions tends to deposit on catalyst surface.[33] In the hydrogenation of alkynes, their dissociative adsorption leads to the formation of polymeric C_4 species. Dimer was reported as byproduct for the

solvent free semi-hydrogenation of MBY in a few recent studies.[25, 29, 41] Commercial catalysts are deactivated as a result of the adsorption of oligomers on the surfaces and the consequent blocking of active sites in Pd.[42]

Poisoning. Poisoning occurs due to the chemisorption of impurities on the active sites leading to the loss of catalyst activity. Strongly adsorbed species covers the total metal surfaces and poisons them irreversibly, whereas partial coverage of metal surface by weakly adsorbed species often result in a selectivity enhancement.[33] A study showed that the poisoning effect of halogen ions led to a decrease of the catalytic activity and deactivation of the polymer-anchored palladium catalyst.[43]

2.1.7 Solvent effects

In general, the choice of solvent can have significant effect on the performance of a catalyst. It has been found that a polar solvent enhances adsorption of the non-polar reactant while a non-polar solvent enhances the adsorption of a polar reactant.[44] In this study, MBE and MBY are both polar substrates, and the reaction medium water and ethanol are also polar solvent. However, hydrogen dissolves in ethanol much better than in water. The major difference between aqueous and most organic solvent systems is the low solubility of H_2 in water. Table 2.1 lists the solubility of H_2 in water and organic solvents. To run a hydrogenation reaction at the same concentration of dissolved hydrogen as in the organic solvents in Table 2.1 under atmosphere pressure, 2-5 times higher pressure is needed for an aqueous system. Finally, dissociation of water always results in a certain concentration of H^+ expressed as the pH of the solution. Some catalysts and substrates also show acid-base behavior which will influence the catalytic reactions.[45]

Table 2.1. Solubility of H_2 in water and in organic solvents[46] (adapted from ref.[45]).

Solvent	10^3 $[H_2]$/M	Temperature / ^oC
Water	0.81	20.0
Methanol	3.75	20.0
Ethanol	2.98	20.0
Ethyl acetate	3.4	21.0
Benzene	2.94	20.0
Toluene	3.5	20.0
Chlorobenzene	2.46	21.2

2.1.8 Mass transfer limitations

In heterogeneous catalytic reactions, the overall rate may get affected by the rate of diffusion. In this case, the rate of reaction is less than that potentially achievable, and the selectivity of the reaction usually diminished in many applications. Heterogeneous catalysts are usually supported on porous materials, and the stagnant fluid in the pores is usually the major diffusion resistance to transport between the ambient stream and the interior of the porous materials.[47] Transport limitations are likely to occur if the catalyst is very active. It is important to understand both internal and external mass transfer of the system in order to study the intrinsic kinetics of the reaction.

The transfer of mass from the bulk fluid phase to the external surroundings can be described by the film model.[48] In the case of three phase hydrogenation reaction, the external mass transfer implies the dissolution of the gas in the solvent and the transfer of reagent from liquid bulk phase to the catalyst surface. The film model assumes the existence of a stagnant layer of thickness δ along the external surface of the catalyst and the gas-liquid interface, and the complete

resistance to mass transfer is located in this stagnant layer.[48] Therefore, it can be assumed that the concentration change only occurs at the phase interface.

Fig. 2.1 shows the concentration profile of reactants in the three phases according to the film model. The G-L mass transfer includes the dissolution of pure hydrogen in ethanol solvent and diffuse through the G-L diffusion film towards the liquid bulk concentration. As hydrogen is supplied continuously to the reaction, its bulk concentration is considered at steady state. The G-L mass transfer mainly depends on the stirring speed and the diffusivity of hydrogen. The liquid-solid mass transfer involves hydrogen and all the other reagents in the reaction diffuse towards the catalyst surface, and depends on the diffusion layer around the catalyst. A recent study on hydrogenation of phenyl acetylene over palladium catalysts in heptane reported that diffusion of hydrogen through the liquid to the catalyst was the main mass transfer resistance in the solvent.[49]

Internal mass transfer is the diffusion of molecules between ambient stream and the interior of the pores of the catalyst support. To characterize the internal mass transfer, one has to know the characteristics of the pore system.

Due to the mass transport phenomena, the observed reaction rate is not necessarily the same as its intrinsic rate. Since mass transfer limitations have significant effect on both catalytic activity and selectivity, mass transfer effects should be addressed when investigating the reaction kinetics in a laboratory-scale catalytic reactor. Stirring speed test and Carberry number can be used to estimate the importance of the external diffusion (gas-liquid and liquid-solid) resistance, whereas Wheeler-Weisz modulus is typically used for internal mass transfer limitation study (see details in section 4.3.1). Both methods are based on the ratio of the observed rate and the maximum mass transfer rate. The Carberry number represents the extent of external mass transport limitation and ranges from zero to unity, corresponding to insignificant and total external mass transportation

limitations.[50] A value of the Carberry number less than 0.05 indicates that the external mass transfer limitation can be neglected. Wheeler-Weisz modulus represents the extent of pore diffusion limitation and ranges from zero to infinity corresponding to insignificant and total pore diffusion limitation, respectively.[50] When the Wheeler-Weisz criterion less than 0.15, the kinetics of reaction is not influenced by the diffusion of the reagent into the pores of the catalyst[51].

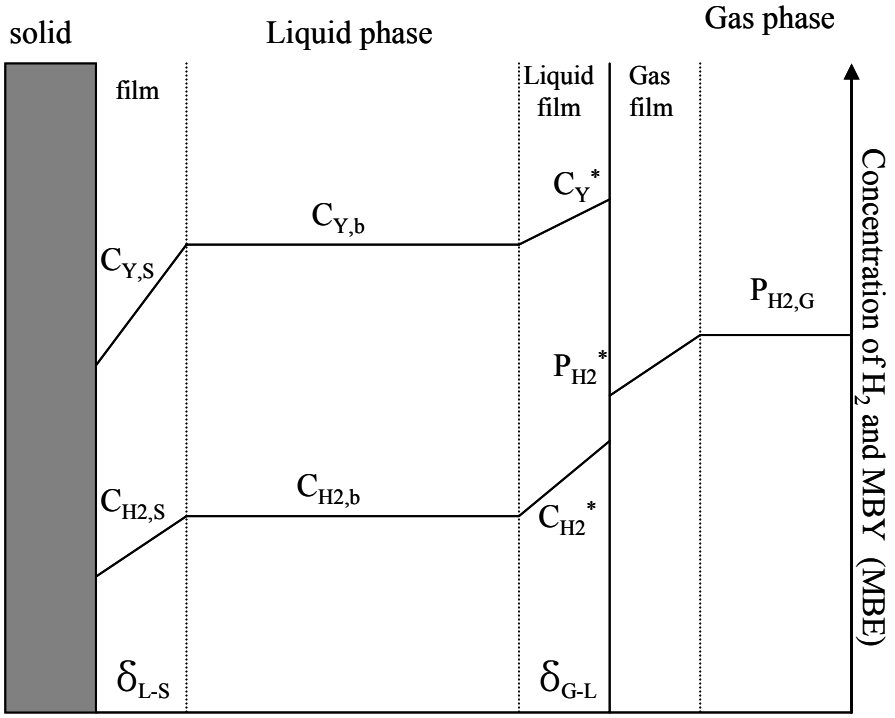

Figure 2.1. Concentration profiles from gas phase to the catalyst surface (external mass transfer) during three phase catalytic hydrogenations of MBY (MBE).

2.2 Nanoparticle synthesis and stabilization

Nanocrystals are crystals with at least one dimension between 1 and 100 nm.[52] Nanoparticles whose particle size deviates less than 10% from the average value are generally addressed as “monodisperse”. A deviation from the mean particle size of approximately 20% is described as showing a “narrow size distribution”.

Synthesis method is crucial to prepare nanoparticles with defined properties. In general, there are two methods to obtain nanoparticles, which are “top-down” and “bottom-up”. The top-down method is to start with a bulk material and then break it into smaller pieces using mechanical, chemical or other form of energy[53] and subsequent stabilization of the resulting nanosized metal particles using protecting agents. As an example, high energy ball milling has been used for generation of magnetic,[54] catalytic,[55] and structural[56] nanoparticles. The technique is already a commercial technology, but contamination is a serious problem from ball-milling processes. The bottom-up method of wet chemical nanoparticle preparation relies on the chemical reduction of metal salts, electrochemical pathways, or the controlled decomposition of metastable organometallic compound.[57] At present, many synthetic methods are used to obtain well-defined metallic nanoparticles following the bottom-up approach.[3-6, 58] In this thesis, the focus is on the solution phase synthesis of nanoparticles, particularly the metal salt reduction method in the presence of stabilizers.

2.2.1 Nucleation and growth mechanisms

The chemical growth of nanoclusters involves a stepwise process of nucleation, growth, and agglomeration. This mechanism was first proposed by Turkevich which is essentially still valid today [59-60] and refined later by modern

data. It was assumed that the mechanism for particle formation was an agglomeration of zero valent nuclei in the seed, or alternatively, the collision of already formed nuclei with reduced metal atoms. In general, two types of mechanisms are considered for the nucleation process, in the presence of reducing agent and/or surfactants. The first one is proposed by LaMer and coworkers, studying solution-phase synthesis of monodisperse sulfur colloids.[61-62] They developed a mechanistic scheme for the formation of clusters in homogeneous solutions (Fig. 2.2). In a typical reaction, the metal salt is reduced to zero-valent metal atoms first. Precipitation of a solid phase from the solution must be involved during the nanoparticle formation. Thus, to initiate the nucleation, the concentration of the metal atoms in the solution must reach a point of supersaturation. Further growth of nucleus is spontaneous but limited by the diffusion of precursor to the nuclei surface.[61] When the concentration is below the critical threshold, nucleation stops and the particles grow by taken up remaining atoms to the existent nucleus. The short nucleation period is a prerequisite for producing monodisperse particles. If the growth time is almost the same for all the particles, a uniform size distribution can be achieved. If nucleation and growth processes overlapped, the growth periods will be different between particles, resulting in non-monodisperse particles. Therefore, it is pivotal to separate nucleation and growth in time. Xia and coworkers proposed that nucleation process depends on the explicit route to atoms, and LaMer mechanism is valid if the precursor compound is decomposed instead of reducing to zero-valent atoms.[8]

In addition, particles can also grow through secondary growth. After particles grow to a stable size, they can grow by aggregation with smaller unstable nuclei and not by collisions with other stable particles.

The second mechanism was proposed by Finke et al. for transition metal

nanoclusters formed under hydrogen and related reducing agents.[63] They proposed a four step, double autocatalytic mechanism by which transition metal nanoclusters nucleate, grow, and agglomerate (self-assemble) under reductive conditions.[64] In this mechanism (Fig 2.3), a slow continuous low level nucleation (A→B), which is far from supersaturation, takes place followed by a fast, autocatalytic surface growth (A+B→2B). The fast autocatalytic growth step consumes the available A once the step starts, thereby shutting off the nucleation step. The nucleation and growth step will be separated as needed to achieve near monodisperse nanoparticles. The third step is bimolecular agglomeration (B+B→C), and following by the final step of autocatalytic agglomeration of small nanoclusters with larger, bulk metal clusters (B+C→1.5C).

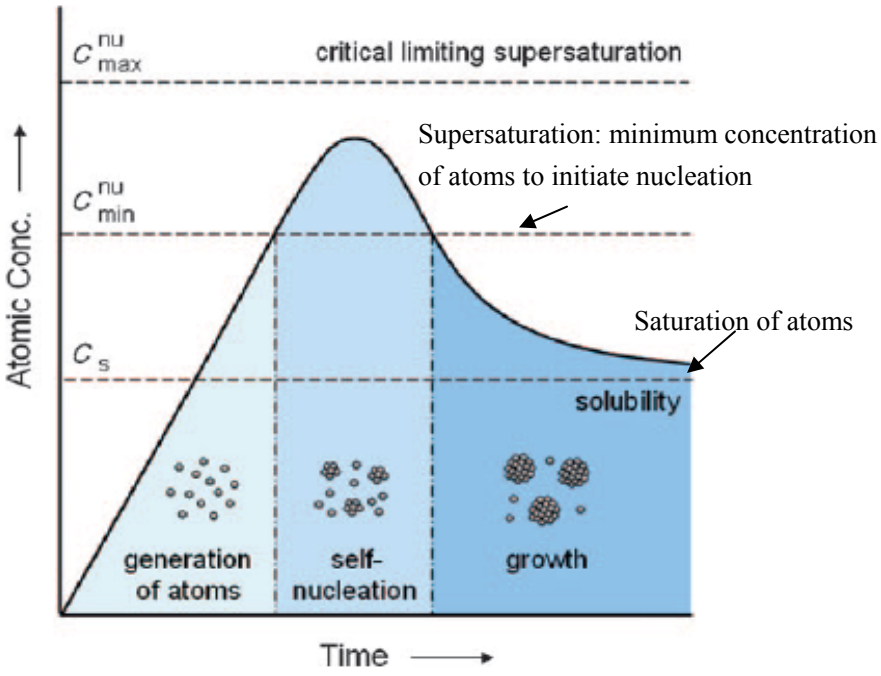

Figure 2.2. Schematic representation of atomic concentration against time, illustrating the generation of atoms, nucleation, and subsequent growth (adopted from ref. [8, 61] with permission from [8, 61]).

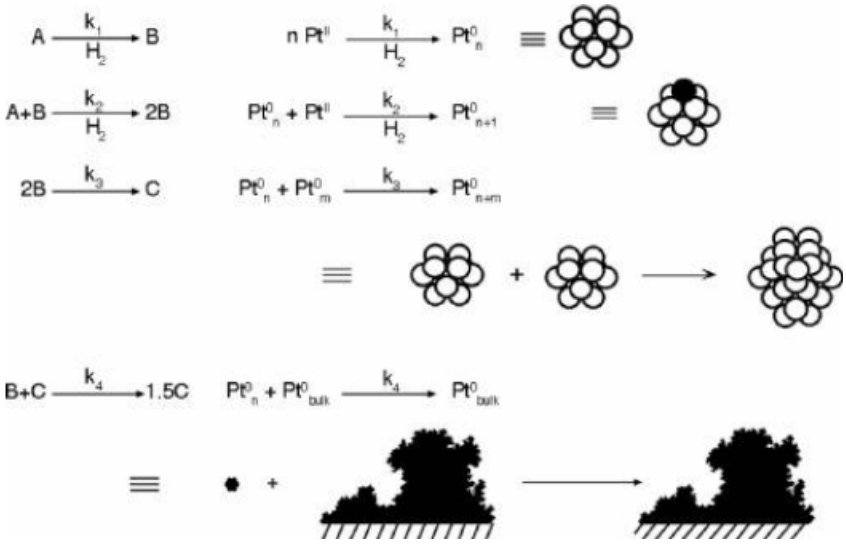

Figure 2.3 Double autocatalytic mechanism for the metal nanocluster formation (adapted from ref. [64] with permission).

2.2.2 Metal nanoparticle stabilization

High surface energy and large surface curvature make nanoparticles thermodynamically unstable[65]. To prevent aggregation into large particles and finally produce stable nanoparticles, these nanoparticles have to be stabilized during reaction. Basically, there are three types of nanoparticle stabilization: in electrostatic stabilization (Fig. 2.4), anions and cations from the starting materials remain in the solution, interact with the metal surface and form an electrical double layer around nanoparticles. This results in a Coulombic repulsion between individual particles and prevents agglomeration.[66] In steric stabilization (Fig. 2.4), aggregation is prevented by large molecules firmly adsorbed on the metal surface.[66] These large adsorbates provide steric barrier between particles. A third type is electrosteric stabilization which combines both steric and electrostatic effects. Some common protective agents (mostly steric) used to cap transition metal nanoparticles in colloidal solution are polymers, surfactants, dendrimers, and ligands.

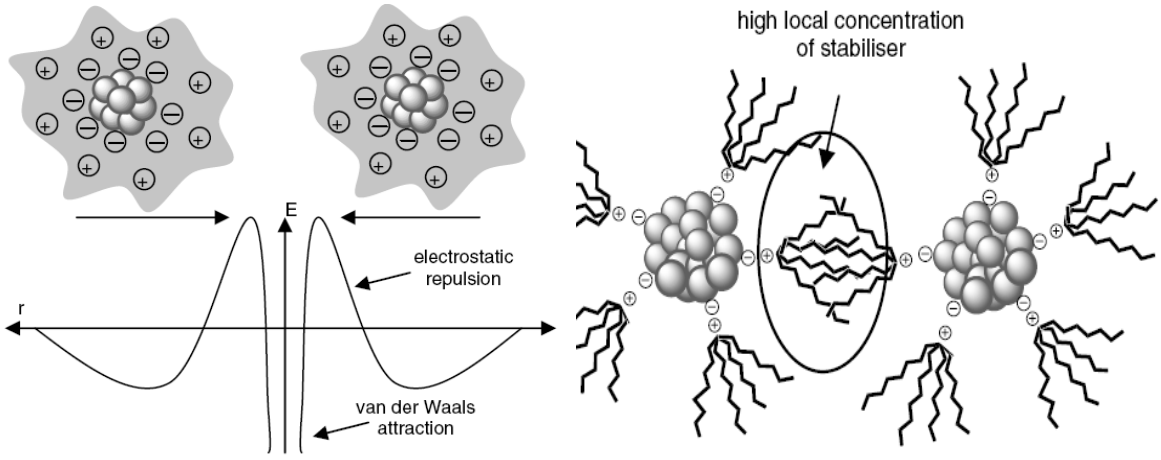

Figure 2.4 Electronic stabilization (left) and steric stabilization (right) of metal nanoparticles (adapted from ref. [67] with permission).

Linear Polymers

Steric stabilization is usually accomplished by using bulky organic molecules as the protecting agents such as polymers and surfactants. Polymers are adsorbed on the surface of nanoparticles. They form many weak bonds with the nanoparticles surface instead of forming less strong bonds at specific sites. These weak bond barriers prevent close contact of the metal particle centers. Poly(N-vinyl-2-pyrrolidone) (PVP) has been successfully used to stabilize and control size of transition metal nanoclusters (Fig. 2.5). Hirai et al.[68] showed the carbonyl groups of PVP partly coordinate to the surface Pd atoms. The amount of PVP used in solution is expected to affect the growth process of Pd nanoparticles. Therefore, the size of Pd nanoparticles can be changed by varying the polymer concentration. The PVP-Pd nanoparticles with mean diameter range from 17 to 30 Å were synthesized in one step by changing the amount of PVP and/or the concentration of alcohol.[69] Increasing the amount of PVP made the size of Pd nanoparticles smaller; however, the nanoparticles' lower limit was determined by

the alcohol used. PVP-stabilized nanoparticles have been tested for catalytic process. Decrease the nanoparticle size down to 3 nm improved the catalytic activity in the Suzuki reaction, which suggests that the low-coordination-number vertex and edge atoms on the particle surface are the active catalytic sites.[35]

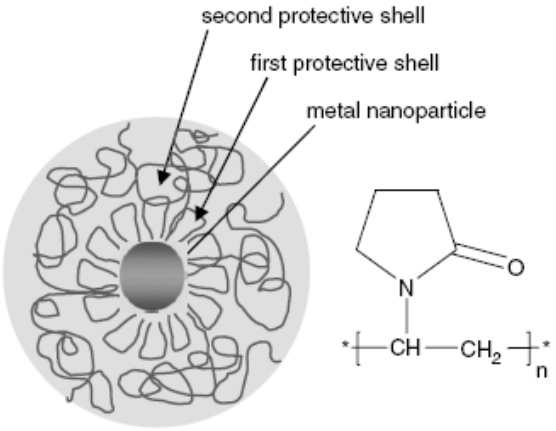

Figure 2.5. Model of PVP-stabilization of metal nanoparticles (adapted from ref. [67] with permission).

Surfactants, Micelles, and Microemulsions

Surfactants acting as colloidal stabilizers not only help to control the particle growth to yield a fairly monodispersed size distribution, but also efficiently preventing their aggregation into large particles. Some commonly used surfactants are hexadecyltrimethylammonium bromide (CTAB), sodium bis(2-ethylhexyl)sulphosuccinate (AOT), and pentaethyleneglycol dodecyl ether (PEGDE). A wide range of surfactants of the cationic, anionic, and non-ionic type have been applied successfully as colloidal stabilizers to yield isolable nanometal colloids that can be redispersed to form highly concentrated metal solutions in either organic or aqueous media.[57] In nonaqueous media, surfactants such as tetraoctylphosphineoxide and oleic acid have been used to grow cobalt nanorods.[70] In aqueous media, surfactant CTAB (Fig. 2.6) has been one of the

most popular molecules in the synthesis of nanoparticles.[71-73] CTAB plays the role of capping and structure-directing agent,[74] which also can be eliminated easily from the metallic surface. Nikoobakht and El-Sayed proposed that the auto-organization of the CTAB molecules in a bilayer horizontal manner at the surface of the growing nanoparticle would enhance the anisotropic growth.[71, 75] Then different structures of seed such as single crystal, multiply twinned crystal would grow to cubes and rods at the presence of CTAB.[8]

CTAB can alter the growth rate through selective chemisorption. A face-centered cubic (fcc) single crystal can evolve from cube to cuboctahedron and then to octahedron by increasing the ratio of (111) to (100) facet areas.[76] The capping agent may significantly affect the relative growth rates of different facets through their interactions with the metal surfaces. Thus, the facet with a slower growth rate may expose more on the nanocrystal surface. As known, the Br^- from CTAB adsorbs preferentially on (100) facets, blocks them from subsequent growth, promoting their formation.[8, 76-77] Therefore, nanocubes which are enclosed by six (100) facets can be promoted by introducing CTAB as a capping agent.

The nucleation and growth steps of nanoparticles can be better controlled by applying “seed-mediated” approach which uses seeds as nucleation sites for the anisotropic growth.[72] The synthesis of anisotropic Au or Ag nanorods using seed-mediated approach was successful. CTAB coats the nanorod surface as a bilayer (Fig. 2.7) to prevent aggregation, it also aid the nanorod growth by selective adsorption on (100) faces[78]. Berhault et al.[71] have shown that increase the concentration of CTAB drastically decreases the rate of reduction of Pd precursor. The slow reduction allows a better kinetic controlled growth regime, favoring the formation of nanorods.

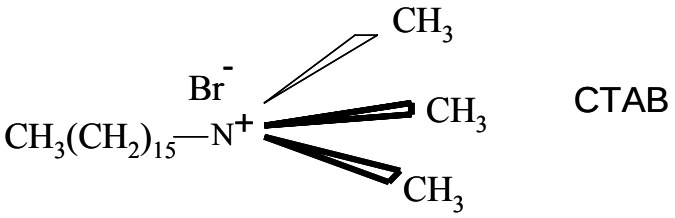

Figure 2.6. Structures of surfactants Hexadecyltrimethylammoniumbromide (CTAB) (Modified from ref.[79] with permission).

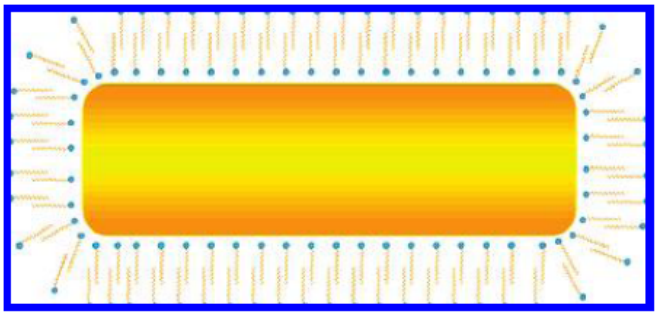

Figrure 2.7 A nanorod created by a CTAB bilayer. The circles represent the ammonium head groups and the zigzags are the hydrocarbon tails of the CTAB (adapted from ref. [78] with permission).

The development of microemulsion methods for nanoparticle preparation is of great interest since this system allows formation of small metal nanoparticles with narrow size distribution as well as bimetallic particles of controlled composition. Microemulsion is a thermodynamically stable liquid mixture of water, oil and surfactant, frequently in combination with a co-surfactant. Depending on the concentration of water and oil, microemulsions can be defined as three types: water-in-oil (reverse), oil-in-water and bicontinuous microemulsions.[80] The size of different droplets in the microemulsion system varies from 10 to 100 nm depending on the type of surfactant.[80] The synthesis of

inorganic nanoparticles is usually carried out in w/o microemulsions which consist of small reverse micelles (Fig. 2.8). In the hydrophilic interior of these micelles, a certain amount of metal salt can be dissolved and serve as metal precursors for the final metal particles. Nanoparticles can be prepared by mixing two microemulsions carrying the appropriate reactants respectively, the metal precursor and the reducing agent (Fig. 2.9). Another method is adding the reducing agent directly to the microemulsion containing the metal precursor. In both cases, the reactants interchange during the collision of the water droplets just during the mixing process. The reaction of nucleation and growth takes place inside the droplet, which controls the final size of the particle. After the particles grow to final size, the surfactant molecules stabilize and protect them against further growth. The surfactant sterically prevents the nuclei from growing too fast which controls the rate of particle growth.

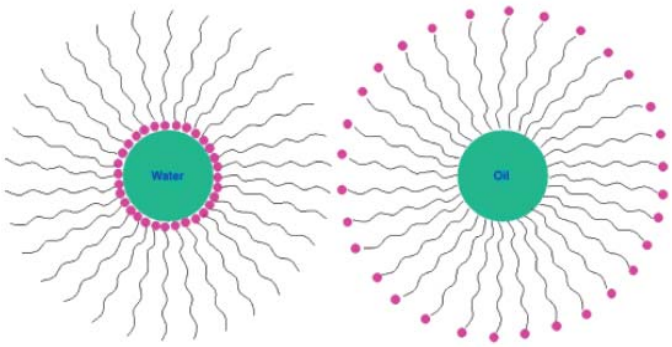

Figure 2.8. Reverse micelle and normal micelle structures (adapted from ref. [65] with permission).

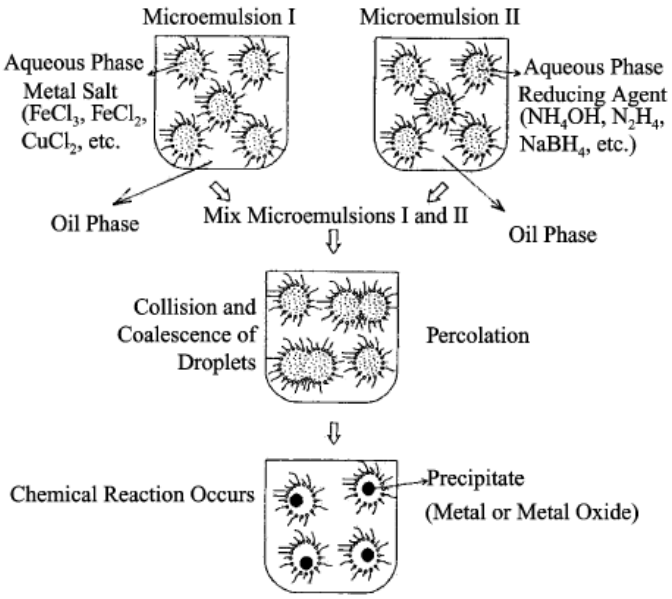

Figure 2.9. Formation of metal nanoparticles from mixing w/o microemulsions (adapted from ref. [81] with permission).

The final particle size depends on the nature of a surfactant, metal precursor, reducing agent, their concentrations, pH, temperatures, and presence of a co-surfactant.[5] The final size of the nanoparticle is mainly influenced by the water-to-surfactant ratio. Generally, increasing the ratio will increase the size of the droplets in microemulsions which leads to bigger metal particles. Lisiecki and Pileni[82] have prepared copper nanoparticles in water/AOT/cyclohexane microemulsions. The size of the Cu particles increased from 2 to 10 nm with the increasing of water to surfactant ratio from 1 to 10. The use of co-surfactant also plays a role on size control of nanoparticles. Palladium nanoparticles have been synthesized in the cationic w/o microemulsions of water/CTAB, n-butanol/isooctane by Wang et al.[83] It was found that the average diameters of the Pd nanoparticles increased from 3.95 to 8.12 nm with the increase of n-butanol (co-surfactant)/CTAB weight ratio from 0.75 to 1.25, respectively.

A variety of catalytic nanomaterials have been produced successfully from

microemulsions and used in a wide range of catalytic applications, such as transition metals (Pt, Pd, Cu, Co etc.), single metal oxides (ceria, CeO_2; titania, TiO_2 etc), mixed metal oxides of for example perovskite ($LaMnO_3$) and finally metal coated by metal oxide (e.g. Pt–TiO_2).[84]

Dendrimers

Dendrimers are repeatedly branched macromolecules with shapes resembling molecular cauliflowers. Their structure and chemical properties can be designed by modifying the core, branched chains, and the terminal functional groups.[85] Poly(amidoamine) (PAMAM) and poly(propylene imine) (PPI) dendrimers are the two commercially available families of dendrimers (Fig.2.10). Nanoparticles are introduced inside the dendrimers. The dendrimer first acts as a molecular template to prepare the metal nanoparticles, then as a stabilizer to prevent agglomeration. The nanoparticles are synthesized by complexing metal ions within dendrimers and then reducing those ions to zerovalent metal atoms.[86] The advantage of using dendrimers is not only their loose binding of the nanoparticle surface, but also a precise and predictable number of Pd atoms exist in the Pd nanoparticle catalyst or precatalyst.[87] Li and El-Sayed[88] discussed the effect of dendrimer (PAMAM) on the size and stability of Pd particles in their study of catalytic activity. The Pd nanoparticles were produced at mean diameters of 3.6 ± 0.8 nm and 1.4 ± 0.4 nm with the respect molar ratios of [Pd^{2+}]/[dendrimer] of 5 and 10. They also proposed that high generation dendrimers had compact structures and expected to provide effective protection action for the prepared metal particles.

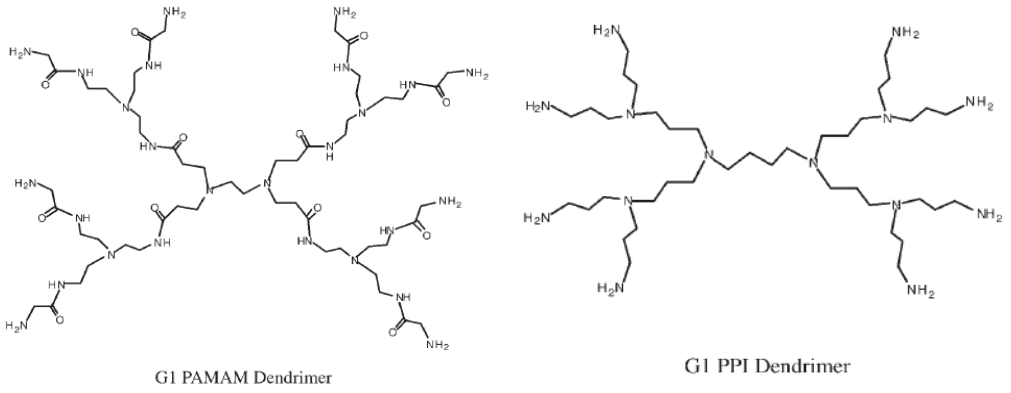

Figure 2.10. Two families of commercial dendrimers as their first generation (G1) (adapted from ref.[89] with permission).

Ligands

Nanoparticles can be protected by a shell of appropriate ligands to prevent aggregation and so to save the individual properties of the single particle. Some commonly used ligand stabilizers for metal nanocluster size control are polyoxoanions, 1, 10-phenanthroline, tetraalkylammonium salts, etc. The first ligand-stabilized Au13 clusters were described by Schmid as early as 1981,[90-91] while the first Pt_{13} cluster is achieved via the decomposition of dimethyl(1,5-cyclooctadiene) platinum(II) in the presence of trialkylaluminium 24 years later.[92] Toshima et al. prepared ligand stabilized noble metal nanoclusters by various chemical methods.[93] The mean diameters of palladium, platinum, rhodium and Pd/Pt nanoclusters stabilized by various ligands range from 1.3 to 3.2 nm if prepared in a single step reaction, and 2.2 to 4.0 nm if prepared by stepwise growth method.

2.2.3. Nanoparticles with shape control

The properties of a metal nanocrystal are determined by a set of physical parameters including its size, shape, composition, and structure. Theoretically,

one can modify the properties of a metal nanoparticle by controlling any of the parameters, but the properties are highly sensitive to the specific parameters. A lot more examples clearly showed the importance of shape control to achieve efficient utilization of nanoparticles. Therefore, great effort has been put to the synthesis of nanoparticles with controlled shapes.[71, 77, 94-96]

Nanospheres

Transition metal nanospheres mostly show a face centered cube (f.c.c.) structure in the form of cuboctahedrons (Fig. 2.11) with the faces enclosed by (111) and (100).[97] Nanospheres are the most studied nanoparticles since thermodynamics imposes that metal atoms nucleate and grow preferably into a spherical shape.[5] Development of colloidal techniques or synthesis of nanospheres with controlled size has been studied a lot in the past decades. Examples of preparing nanospheres and size effect of spherical nanoparticles have been discussed in previous sections.

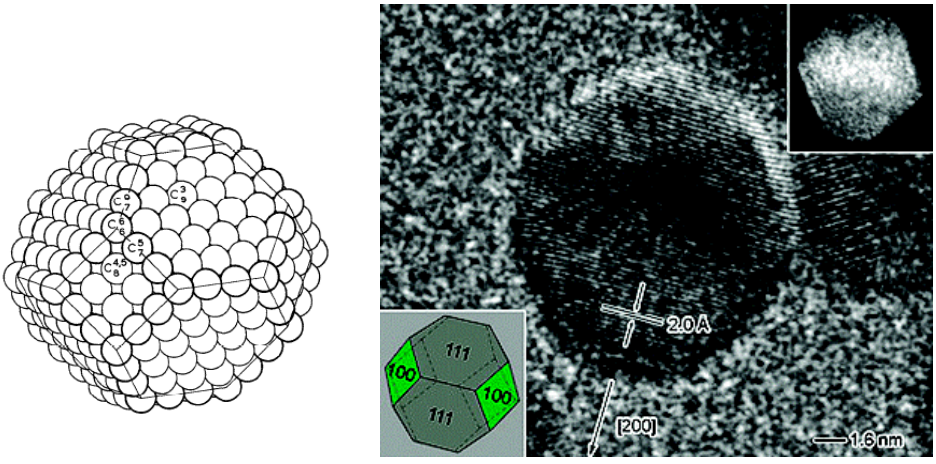

Figure 2.11. F.C.C. cuboctahedron (left, adapted from ref.[7] with permission) and HRTEM image of a Pd cuboctahedron (right, adapted from ref.[98] with permission).

Nanocube

A model of nanocube is shown in Figure 2.12 with all the faces are enclosed by (100) facets. Figure 2.12 also shows a transmission electronic microscopy (TEM) image of gold nanocubes. Gold nanoparticles were prepared based on the Au seeds and subsequent addition of seed solution to the growth solution which contains CTAB, $HAuCl_4$ and ascorbic acid (AA).[77] The morphology and dimensions of the Au nanoparticles depend on the concentrations of the seed particles, CTAB, and reactants in growth solution. These factors were found to be interdependent, thus yielded various shapes with different combinations. It was shown that CTAB molecules bind more strongly to the (100) than the (111) faces.[8, 76-77] Since (100) faces are blocked by Br^-, the reaction favors the deposition of Au^0 on to the (111) faces. The growth continues by metal deposition on (111) faces, thus the crystal elongates along (100) faces. The formation of (100) is preferred and high cube yield is achieved.[77]

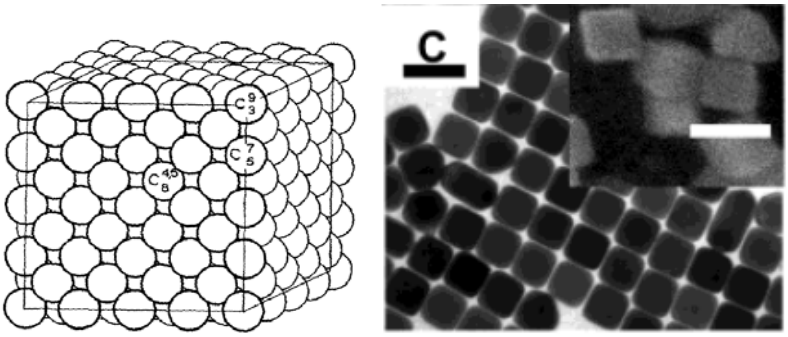

Figure 2.12. F.C.C. cube (left) (adapted from ref.[7] with permission) and TEM image of cubic Au nanoparticles (adapted from ref. [77] with permission) (right). Scale bar=100nm.

Nanotetrahedrons

Figure 2.13 shows an f.c.c. structure tetrahedron with all the faces are enclosed by (111) facets and a TEM image of triangular Au nanoparticles. Gold nanotetrahedrons were synthesized successfully using the seed-mediated technique similar to that of Au nanocubes described above with a different seed concentration.[77] The synthesis method involves addition of Au nanoparticles as seeds to the aqueous growth solutions containing desired quantities of CTAB, $HAuCl_4$, and ascorbic acid. With higher seed concentration, as compared to the above cube synthesis, the major products obtained were triangular outlines instead of cubic ones. However, the synthesis of Pd tetrahedrons using colloidal method is still a challenge.

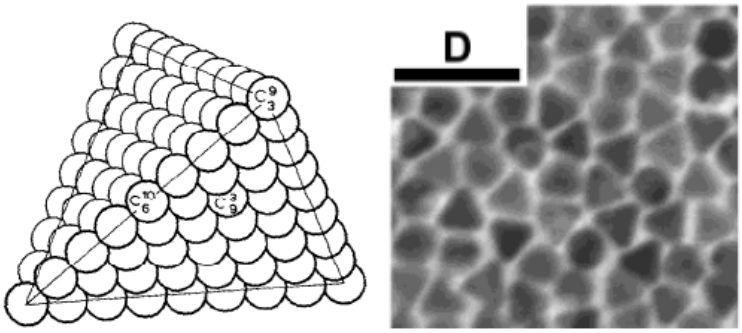

Figure 2.13. F.C.C. tetrahedron (left) (adapted from ref.[7] with permission) and TEM image of Au tetrahedrons (right) (adapted from ref.[77] with permission). Scale bar=100nm.

Nanorods

The structure model and TEM images of nanorods are shown in Figure 2.14. Gole and Murphy[99] proposed a three step seed-mediated approach to produce gold nanorods with different aspect ratios. The seed solution was mixed with the growth solution which contained CTAB, metal precursor and ascorbic acid. A portion of the mixed solution was then added to another growth solution. Upon repeating the procedure, gold nanorods with different aspect ratio could be

obtained with the use of different size of seeds. It was found that increasing the seed size results in lower nanorod aspect ratio. The chemisorption of bromide on the seed surface was believed to alter the order of free energies of different facets and promote the formation of (100) and (110) facets.

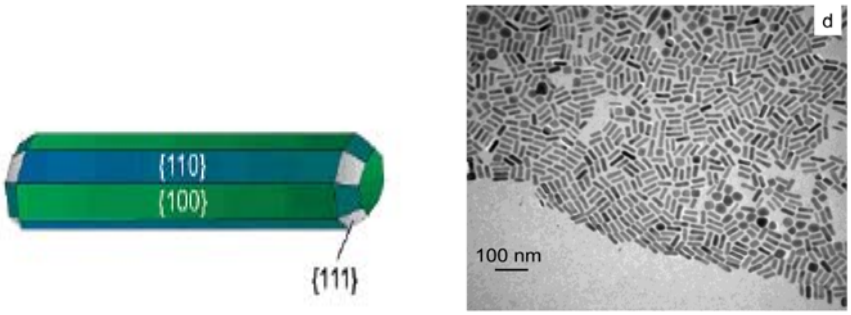

Figure 2.14. An illustration of nanorods with octagonal cross-section and side surfaces enclosed by (100) and (110) facets (left) (adapted from ref.[97] with permission), and TEM image of Au nanorods (right) (adapted from ref. [94] with permission).

2.3 Concluding remarks from the background review

As seen from the above literature review, many catalytic reactions are structure sensitive including industrially relevant hydrogenations. Metal nanoparticles with controlled size and shape can be used to reveal the structure sensitivity of reactions. It is important to have monodispersed particles which differ only in particle size and/or shape in order to identify the structure sensitivity. Recent achievements in nanotechnology have allowed synthesizing such nanoparticles; in particularly, the colloid preparation techniques provide catalytic metal particles with size or structure variation without other perturbations.[5] Mass transfer limitations have significant effect on both catalytic activity and selectivity in three phase hydrogenations, thus it is important to study the catalytic behavior under kinetic regime. Stirring speed test and Carberry number can be used to estimate the influence of the external diffusion limitations, whereas

Wheeler-Weisz modulus can be calculated for internal mass transfer limitation. From the literature search, structure sensitivity studies of an olefinic and acetylenic alcohol hydrogenation using well-defined nanoparticles of different shapes have not been attempted yet. They can result in valuable knowledge on the reaction active sites in the absence of materials and pressure gaps.

As shown in the literature review, there are many factors that can directly influence the morphology of the nanoparticles. To study structure sensitivity of a reaction, the nanoparticles from one synthesis have to be well-defined in shapes and monodispersed with narrow size and shape distribution. It is also important to use the same stable agent as different stabilizers may affect the catalytic behavior. CTAB was chosen for the study as the surfactant usually plays the most important role in shape-controlled nanoparticle synthesis. It was known that Br^- from CTAB adsorbs preferentially on the (100) facets, promote their formation and enhance anisotropic growth. Different strategies reviewed above can be used to produce nanoparticles with different shapes. Spherical nanoparticles can be prepared using fast metal salt reduction in the presence of stabilizers and microemulsion methods. Typically, the metal salt ion is reduced to zero-valent Pd atoms, which subsequently aggregate to from nuclei. After the nucleation stage, each type of seed can still grow into a nanocrystal with several possible shapes. It is believed that further growth of seeds may selectively enlarge one set of crystallographic facets at the expense of others to yield the final shapes.[76] Single crystal seeds can evolve into octahedrons, cuboctahedrons, or cubes, depending on the ratio of growth rate along the [111] and [100] directions.[76] Seed-mediated synthesis is widely used to obtain different shapes. Varying the concentration of seed solution or CTAB, metal salt and reducing agent concentrations in the growth solution, various shapes can prepared with different combinations.

Chapter 3. Experimental section

3.1 Nanoparticle synthesis

Materials: Dihydrogen tetrachloropalladate(II) (H_2PdCl_4, 5% w/v, Acros Organics), cetyltrimethylammonium bromide (CTAB, ≥98%, Sigma Aldrich), sodium borohydride ($NaBH_4$, ≥98.0%, Sigma Aldrich), ascorbic acid (≥99.0%, Sigma Aldrich), ammonium solution(28.0%-30.0%, Sigma Aldrich), hydrazine hydrate ($H_4N_2 \cdot H_2O$, 35wt.% solution in water, Sigma Aldrich), acetone (>99.7%, Fisher Scientific), methanol (>99.8%, Fisher Scientific), extra-dry isooctane (99.8%, Fisher Scientific), n-butanol (99.8%, Fisher Scientific), sodium hydroxide (NaOH, >98.7%, Fisher Scientific), and aluminum oxide (corundum, α-Al_2O_3, 99%, 100 mesh, Sigma Aldrich) were used as received. Milli-Q water was used throughout the study.

3.1.1 Spheres of different size

3.1.1.1 Synthesis of CTAB-stabilized Pd spherical nanoparticles

Synthesis of CTAB-stabilized Pd nanoparticle (seed)

S1. Pd spheres were synthesized according to the method developed for Au seeds[94] by reducing H_2PdCl_4 with sodium borohydride in the presence of CTAB as a capping agent. 25 mL of an aqueous 1.0 mM H_2PdCl_4 solution was mixed with 50 mL of an aqueous 0.15 M CTAB solution at room temperature. 0.01 M $NaBH_4$ solution was freshly prepared in ice bath, and then 6 mL was added all at once following by stirring for 5 min. The solution turned dark immediately after adding $NaBH_4$, indicating particle formation. The solution was left at room

temperature for 1 h for complete reduction. For the catalytic studies, the nanoparticles were deposited on α-Al_2O_3. 3 g of the support was added to the colloidal dispersion, followed by at least triple volume of acetone to precipitate nanoparticles on the support. After stirring for 1 h, the resulting catalyst was copiously washed with methanol to remove CTAB and unreduced Pd precursor, and dried at room temperature.

Preparation of growth solution

The growth solution was prepared by mixing 50 mL of an aqueous 0.5 mM H_2PdCl_4 solution with 50 mL of an aqueous 0.16 M CTAB solution while stirring.

Seed-mediated Growth

Four sets of reactions were conducted following both one step and the step by step seeding scheme to prepare different sized spherical Pd nanocrystals. Seeding growth methods involves the growth of small seeds into larger particles, and employs subsequently prepared larger particles as seeds for later stage particle enlargement. A weak reducing agent ascorbic acid was used to prevent secondary nucleation during the growth stage. The synthesis procedure was adopted from Jana's method for gold nanoparticle synthesis.[72] Following the seeding growth approach, gold nanoparticles of diameters 5-40 nm were prepared with 10-15% standard deviation in diameter. The method can also be scale up to produce 10-100 mg of Au nanoparticles.

a) In set A (*S2*), 15 mL of growth solution was mixed with 0.1 mL of freshly prepared 0.1 M ascorbic acid solution. Next, 5.0 mL of seed solution was added while stirring. The color turned brown in a few minutes. Stirring was continued for a further 10 min for complete reduction of the palladium salt. In the case of Au nanoparticles, set A yielded spherical particles with a diameter of 5.5±0.6 nm.[72]

b) In set B (*S3*), 18 mL of growth solution and 0.10 mL of 0.1 M ascorbic acid solution were mixed and 2.0 mL of seed solution was added under vigorous stirring. Stirring continued for additional 10 min. The final color of the solution was brown. The particles prepared here were used as seeds in set C 30 min after preparation. Set B is similar to set A, use the same seed solution but more growth solution to obtain larger particle as compared to set A. In the case of Au nanoparticles, set B yielded spherical particles with a diameter of 8.0±0.8 nm.[72]

c) In set C (*S4*), 18 mL of growth solution and 0.1mL of 0.1 M ascorbic acid solution were mixed, and 2.0 mL of seed solution from set B was added under vigorous stirring. Stirring continued for additional 10 min. The final color of the solution was light brown. Based on the step by step seeding method, the subsequently prepared nanoparticles from set B were employed as seeds to get larger particles. In the case of Au nanoparticles, set C yielded spherical particles with a diameter of 17±2.5 nm.[72]

d) Set D (*S5*) was the scale up procedure of set A. The growth solution contained the same CTAB concentration but 2 times more H_2PdCl_4 (1.0 mM). 15 mL of growth solution was mixed with 0.2 mL of freshly prepared 0.1 M ascorbic acid solution. Next, 10.0 mL of seed solution was added while stirring. Stirring was continued for additional 10 min. The seeding procedure is similar to set A but doubles the amount of seeds and ascorbic acid to obtain more nanoparticles. In the case of gold nanoparticles, set D could scale up to produce 2-20 mg of spherical Au nanoparticles.[72]

3.1.1.2 Synthesis of Pd spherical nanoparticles in water-in-oil microemulsions

Synthesis of Pd nanoparticle in water-in-oil microemulsions

S6. Palladium nanoparticle seeds were synthesized by the reduction of

$Pd(NH_3)_4Cl_2$ with hydrazine in the cationic water-in-oil (w/o) microemulsions by following the method developed by Wang et al.[83] CTAB and n-butanol acted as the surfactant and co-surfactant. The aqueous 0.01 M $Pd(NH_3)_4Cl_2$ solution was prepared by adding ammonium solution to H_2PdCl_4 to adjust the pH to 9. Then 0.01 M $Pd(NH_3)_4Cl_2$ or 0.05 M N_2H_5OH solution was mixed with CTAB, n-butanol and isooctane to prepare two microemulsion solutions. The microemulsion composition was 20: 40: 40 respective to the weight percent of water/CTAB, n-butanol/isooctane. Then same amount of two w/o microemulsion solutions were mixed together rapidly to prepare palladium nanoparticle seeds. The final microemulsion was 100 ml and turned dark in about 1 min. The seeds were prepared at n-butanol to CTAB weight ratio of 1. It took approximately 30~60 min for the nanoparticles to complete reduction at room temperature. The synthesis procedure developed by Wang allowed synthesis of Pd spherical particles with average diameter of 5.75±1.33 nm.[83]

S7. Pd nanoparticles were also prepared by a similar microemulsion method developed for platinum.[100] The microemulsion composition was 17.2 : 14.2 : 68.6 respective to the weight percent of CTAB/water/n-butanol. Then 0.2 ml of H_2PdCl_4 was mixed with the microemulsion at room temperature. Hydrazine in the amount of 2% of total volume was used to reduce the metal salt. The microemulsion turned black in 1 min and was left for 30 min for complete reduction. The synthesis procedure developed for platinum allowed synthesis of Pt spherical particles with diameter ~4.0 nm.[100]

After complete reduction, S6 and S7 were centrifuged at 8500 rpm for 20 min followed by methanol wash to purify the seeds from excess surfactant. Then the Pd seeds were redispersed in water after centrifugation. Such method was showed to wash efficiently Pd nanoparticles prepared in w/o microemulsions stabilized by aerosol OT (AOT) without agglomeration.[25] For the supported

catalyst, the solution was centrifuged to reduce the volume to 2 ml. The concentrated solution was impregnated onto 5 g of Al_2O_3, washed with methanol and dried at room temperature.

3.1.2 Seed-mediated synthesis of Pd nanocrystals

The Pd nanoparticles synthesized previously (*S1* and *S6*) were used as seeds solutions to prepare palladium nanoparticles with different shapes. The microemulsion was used as seed directly without separating the nanoparticles. All the seeds were used between 2 and 24 h after its preparation. Nanoparticles with shapes of cube and hexagon were synthesized by varying the concentration of ascorbic acid and seed solution according to Sau and Murphy's[77] method for Au nanoparticles.

Nanohexagons (S8): The growth solution was prepared by mixing 162 mL of an aqueous 0.25 mM H_2PdCl_4 solution with 32.0 mL of an aqueous 0.1 M CTAB solution while stirring. Then 6.0 mL of 0.1 M ascorbic acid solution and 10.0 μL of the seed solution were added in order, followed by gentle mixing. Solution turned brown from orange after stirring for 24 h. In the case of Au system, hexagons around 70 nm (distance between opposite sides) could be synthesized at ~80% yield using gold seed prepared the same method as S1.[77]

Nanocubes (S9): The growth solution was prepared by mixing 136.0 mL of an aqueous 0.29 mM H_2PdCl_4 solution with 40.0 mL of an aqueous 0.08 M CTAB solution while stirring. Then 24.0 mL of an aqueous 0.05 M ascorbic acid solution was added immediately, followed by 10.0 μL of the seed solution under mixing. The solution turned dark brown from orange after stirring for 24 h. In the case of Au system, cubes with ~66 nm average edge length could be synthesized at ~85% yield using gold seed prepared the same method as S1.[77]

Nanorods (S10): Nanorod was prepared following Sau and Murphy's[94]

method for Au nanoparticle. The growth solution was prepared by mixing 2.3 mL of an aqueous 3.43 × 10^{-2} M H_2PdCl_4 solution with 190 mL of an aqueous 0.1 M CTAB solution while stirring. Then 6.0 mL of 0.1 M ascorbic acid solution and 1.67 mL of the seed solution were added in order, followed by gentle mixing. The solution was left undisturbed for at least 5 hours. The synthesis procedure developed for Au allowed synthesis of Au rods with dimension of 50 (±6) × 10 (±2) at a yield of 55(±17) % using gold seed prepared the same method as S1.[94]

For the supported catalyst, the solution from seed-mediated method (S8-S10) was centrifuged at 8500 rpm for 30 min to reduce the volume to 2 ml. The concentrated solution was impregnated onto 0.5~2.5 g of Al_2O_3, washed with methanol to remove CTAB surfactant and dried at room temperature.

3.1.3 Direct synthesis of Pd nanoparticles-nanocubes (S11)

Pd nanocubes were prepared using a method of Niu et al.[101] 5 mL of 10 mM H_2PdCl_4 solution was added to 100 mL of 12.5 mM CTAB solution under stirring. Then the solution was refluxed at 368 K for 5 min following by adding 0.8 mL of freshly prepared 100 mM ascorbic acid solution. The color of the solution turned brown in 10 s after adding reducing agent. The reaction was allowed to proceed for 30 min. For the supported catalyst, the solution was centrifuged at 8,500 rpm for 30 min to reduce the volume to 2 ml. The concentrated solution was impregnated onto 2.7g of Al_2O_3, washed with methanol to remove CTAB surfactant and dried at room temperature. Nearly monodispersed Pd nanocubes with edge length ~20 nm can be produced by following this synthesis procedure.[101]

3.2 Catalyst characterization techniques

Transmission electron microscopy (TEM)

TEM and HRTEM studies were performed on a JEOL 2100 and JEOL 2200 FS transmission electron microscopes operating at 200 kV. Electron diffraction patterns were obtained at JEOL 2010 TEM at 200 kV. Typically, the samples were prepared by dropping the colloidal dispersion of metal nanoparticles onto a holey carbon supported Cu grid (400 mesh) and evaporating the solvent at room temperature. For some supported catalysts, the catalyst was suspended in ethanol, and then redispersed under ultrasonic bath for 2 min to leach out the nanoparticle for TEM studies. For each sample, at least 150 particles were counted. Particle size distribution and corresponding statistical analysis were studied using ImageJ software.

For the corundum-supported catalysts, the TEM samples were prepared by grinding the catalyst with mortar and pestle. The fine powder was then dispersed into ethanol, following by placing a drop of solution on the holey carbon copper grid and dry at room temperature.

Atomic Absorption Spectroscopy (AAS)

The Pd loading on the catalyst before and after reaction was determined by atomic absorption spectroscopy (AAS) via Varian 220 FS instrument with an air-acetylene flame. The samples were prepared by dissolving the catalyst in approximately 1~2 mL hot nitric acid, and then diluted in water. The standard solutions were prepared as 0.5 ppm, 1.0 ppm, 3.0 ppm, 5.0 ppm, 10.0ppm, and 15.0ppm. Each standard solution was also prepared with 1 mL of nitric acid and kept for use within half a year.

X-ray photoelectron spectroscopy (XPS)

XPS analysis also known as Electron Spectroscopy for Chemical Analysis (ESCA) was performed at Kratos Axis 165 X-ray photoelectron spectrometer to measure the elemental composition of the catalyst surface. The sample was irradiated with soft X-ray photons (1-2 keV), and energy spectrum was measured to estimate the composition. XPS was done on two different catalysts, nanospheres and nanocubes, supported on $\alpha-Al_2O_3$.

BET

Measurement of gas adsorption isotherms are widely used for determining the surface area and pore size distribution of solids. BET surface area and pore volume were measured using Autosorb-1-MP from Quantachrome Instruments using nitrogen.

X-Ray Diffraction (XRD)

XRD measurements were performed on a Bruker AXS diffractometer using a monochromatized Cu-Kα radiation source (λ = 1.5406 Å). The diffractometer is equipped with a HiStar general area 2-dimensional detection system (GADDs) with a sample detector distance of 15 cm. The samples were obtained following the standard preparation described previously without deposition onto $\alpha-Al_2O_3$ and washing out all the CTAB surfactant (CTAB was partially removed). The concentrated Pd solution was dried at room temperature for XRD analysis.

3.3 Catalytic hydrogenations

3.3.1 Experimental procedure and setup

2-Methyl-3-buten-2-ol (MBE, 97%, Acros Organics), 2-Methyl-3-butyn-2-ol (MBY, 98%, Acros Organics) and ethanol (Ricca Chemical Company, 90.5% vol. ethyl alcohol, 5% isopropyl alcohol, and 4.5% methyl alcohol, Ricca Chemical Company) as a reaction solvent were used as received. Hydrogen of ultra high purity 5.0 was purchased from Praxair.

The hydrogenation reactions were carried out in a semi-batch stainless steel reactor (300 mL autoclave, Parr Instruments 4560 Mini Bench Top Reactor) equipped with a high temperature fabric heating mantle and a gas burette for the constant hydrogen pressure supply. There are also thermocouple, internal cooling coil, dip tube for gas entrance and sampling, and hollow gas entrainment impellers installed inside the reactor. A pressure gauge is furnished with the reactor. Figure 3.1 shows the reactor setup.

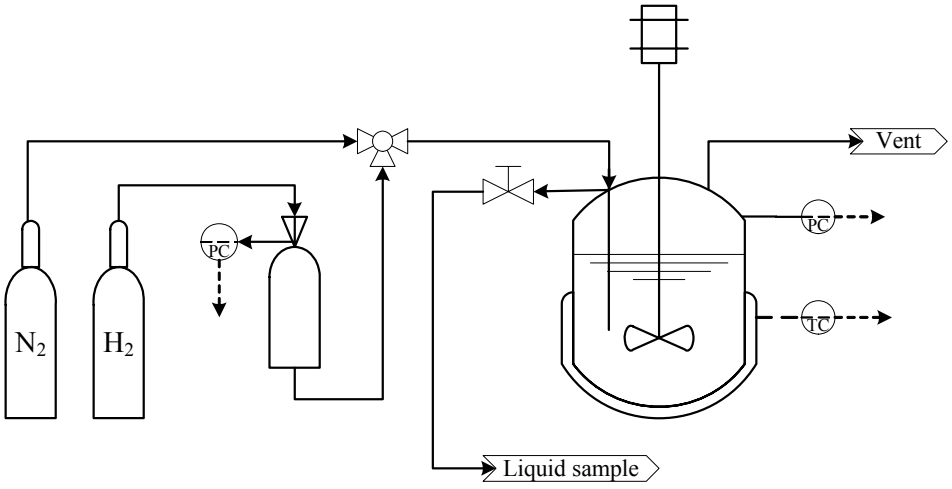

Figure 3.1. Experimental setup for catalytic hydrogenation study.

MBE hydrogenation

After loading the autoclave with 200 mL ethanol which contains 0.04 M MBE and catalyst, the reactor was purged with nitrogen and stirred for half an hour to reach a steady operating temperature. Catalyst quantity corresponded to 8,300 MBE-to-Pd molar ratio. Then the reactor was purged with hydrogen and pressurized. The reactor was operated at 0.45 MPa absolute pressure and a temperature range of 303-323 K. The stirring speed was set to 1200 rpm (unless indicated otherwise) since the manufacture indicates that the gas entrainment impellers operate best in the 800 - 1200 rpm range.

During the reaction, hydrogen pressure inside burette and temperature inside the reactor were recorded all the time. The reaction rate was determined from the hydrogen consumption in the gas burette. The product composition was confirmed off-line by gas chromatography (GC) analysis. The experiments were repeated from 2 to 5 times to ensure reproducibility. Reported errors correspond to one standard deviation.

MBY hydrogenation

The procedure for MBY hydrogenation is similar to that of MBE. During the reaction, the pressure in the reactor was maintained constant at 0.45 MPa absolute pressure. Ethanol was used as a reaction medium containing 0.041 M of MBY in 200 mL. Catalyst quantity corresponded to 10,600 MBY-to-Pd molar ratio. Hydrogen pressure inside gas burette and temperature inside autoclave was always recorded during a reaction. Liquid samples of the reaction mixture were taken via a liquid sampling valve at certain hydrogen conversion during a reaction and later analyzed in GC. In average, 10 samples were taken for each reaction, and the product composition was confirmed by GC analysis. The experiments

were repeated 2 or 3 times to ensure reproducibility. Reported errors correspond to one standard deviation.

3.3.2 Gas chromatography analysis and data treatment

The composition of reaction mixture was analyzed by gas chromatography. The same GC analysis method was used for samples from both MBE and MBY hydrogenations. The samples were analyzed non-dilute using Varian 420-GC with flame ionization detector (FID) and a 30 m Stabilwax (Crossbond Carbowax –PEG, Restek, USA) 0.32 mm capillary column with a 0.25 μ coating. Helium (ultra-high purity 5.0) was used as carrier gas with a pressure of 100 kPa and flow rate 25 mL/min. Injector and flame ionization detector temperatures were set to 473 K and 523 K, respectively. For each run, 1 μm of sample was injected to the column and the total analysis time for each sample is 11 min. The oven temperature was initially held at 323 K for 4 min, then increased to 473 K at a ramp rate of 30 K/min and maintained at 473 K for 2 min. The split ratio was set to 50 during the analysis. By testing with standard solutions, a typical chromatogram shows peaks at retention time of 2.72 min, 3.12 min, and 5.67 min which represent of component MBA, MBE, and MBY in the samples, respectively. The GC response factors were all assumed to be 1 for all the three components (unpublished results from Semagina and Kiwi-Minsker, 2006, Swiss Federal Institute of Technology).

MBE hydrogenation

A typical GC analysis result for samples from MBE hydrogenation reaction is shown in Fig.3.2. The conversion of component MBE was defined in terms of mass fraction as:

$$X_E = 100 - w_E \tag{14}$$

The initial activities were considered as the consumption rate of hydrogen at approximately 10% conversion of MBE. They were calculated by obtaining the slope of the hydrogen consumption graph.

$$r = \frac{\Delta[mol \quad of \quad H_2]}{\Delta[\min][molPd]} \tag{15}$$

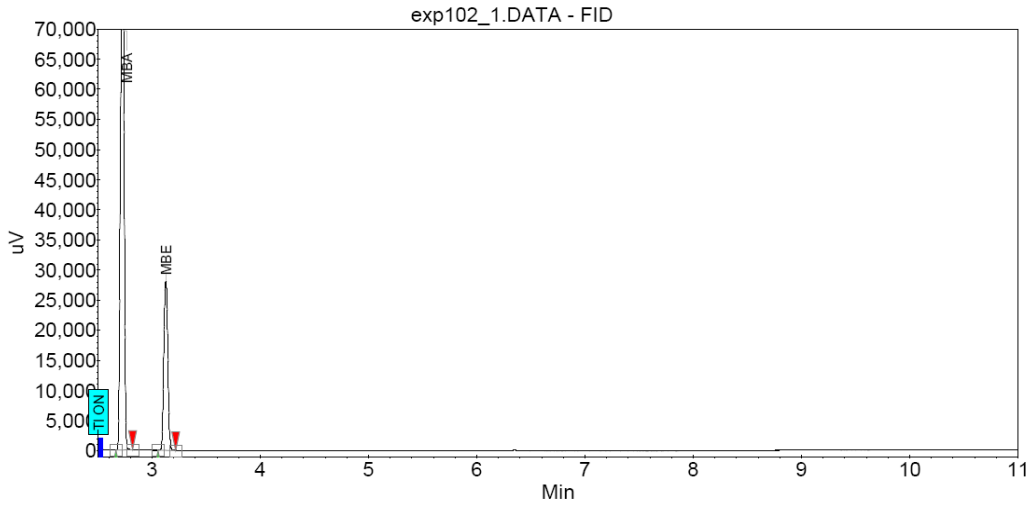

Peak results :

Index	Name	Time [Min]	Quantity [% Area]	Height [uV]	Area [uV.Min]	Area % [%]
1	MBA	2.72	73.55	90506.6	3443.2	73.551
2	MBE	3.12	26.45	28237.6	1238.2	26.449
Total			100.00	118744.2	4681.4	100.000

Figure 3.2. Typical GC analysis result for MBE hydrogenation.

MBY hydrogenation

A typical GC analysis result of samples taken during MBY hydrogenation is shown in Fig. 3.3. Generally, the GC analysis result for the sample taken during a MBY semi-hydrogenation reaction shows three components were detected at retention time of 2.72 min, 3.12 min, and 5.67 min which identifies MBA, MBE,

and MBY in the samples, respectively. No other byproducts or impurities were found during all the sample analysis, where as dimers were reported as byproduct for the solvent free semi-hydrogenation of MBY.[25] Probably, this is due to low concentration of MBY and use of ethanol as a solvent. The mass fraction of each component was calculated from the area under corresponding peak using mathematical function of integration, i.e. wt% = area%. The conversion, selectivity, and yield were defined in molar basis and calculated from the mass fraction. The molar mass of MBY, MBE, and MBA were used as 84.12, 86.13, and 88.13 g/mol in the study, respectively. The molar fraction of each component was calculated according to the following equation,

$$x_i = \frac{\frac{w_i}{M_i}}{\sum_i \frac{w_i}{M_i}} \cdot 100 \qquad \text{where i = A, E, and Y.} \tag{16}$$

Conversion of component MBY was defined as:

$$X_Y = 100 - x_Y \tag{17}$$

Selectivity to component j (MBE or MBA) can be represented as:

$$S_j = \frac{x_j}{100\% - x_Y} \tag{18}$$

Yield was defined as the product of conversion and selectivity:

$$Y_j = X_Y \cdot S_j \tag{19}$$

The initial molar concentration of MBY is calculated as:

$$C_{Y,init} = \frac{w_{Y,init}}{M_Y \cdot V} \tag{20}$$

The initial reaction rate was calculated based on the consumption of alkyne up to 20% conversion:

$$r_{init} = \frac{(C_{Y,init} - C_{Y,20\%conv}) \cdot V_L}{t_{20\%conv} \cdot n_{cat}} \tag{21}$$

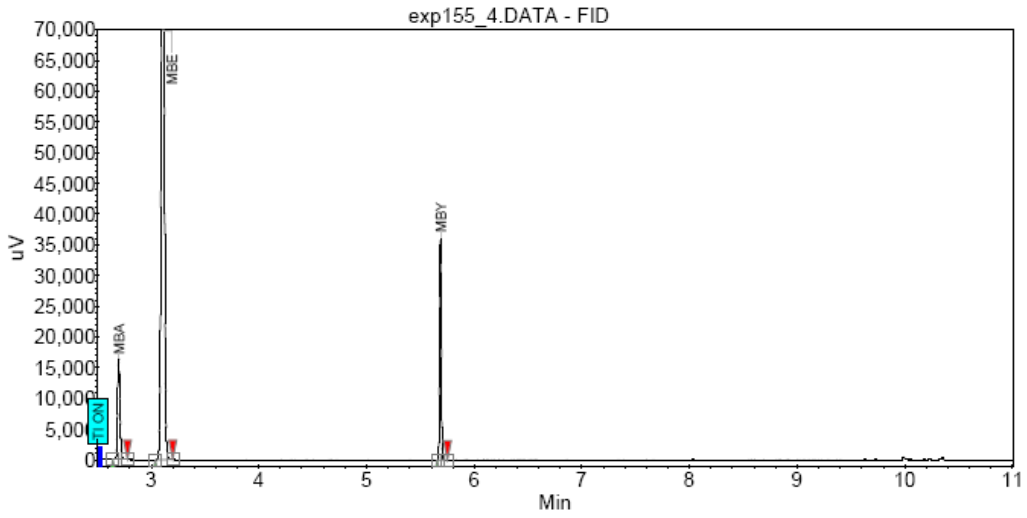

Peak results :

Index	Name	Time [Min]	Quantity [% Area]	Height [uV]	Area [uV.Min]	Area % [%]
1	MBA	2.70	9.14	16491.7	420.2	9.136
2	MBE	3.10	77.88	114149.7	3581.8	77.883
3	MBY	5.69	12.98	36170.0	597.0	12.981
Total			100.00	166811.4	4599.0	100.000

Figure 3.3. Typical GC analysis result of a sample from MBY semi-hydrogenation.

Chapter 4. Results and discussions

To establish structure sensitivity of MBE and MBY hydrogenation over Pd catalysts, well-defined monodisperse in shape and size nanoparticles prepared with the same stabilizer should be applied. As shown in the literature review, there is a variety of methods to produce such nanoparticles, however, many of them were not developed for palladium. In addition, the nanoparticles synthesized in liquid phase should be isolated from the synthesis solution without agglomeration. Thus, our first task was to apply known methods reported for a variety of metal nanoparticles to prepare Pd nanostructures, which could be further isolated without agglomeration for structure-sensitivity studies.

4.1 Nanoparticle synthesis and isolation

4.1.1 Spheres of different size (S1-S7)

Nanoparticles S1. Spherical nanoparticles (also known as "seeds"[99]) were synthesized in the presence of CTAB by fast reduction with sodium borohydride. The diameters of the spheres are around 3.0±0.4 nm (Fig. 4.1). Similar gold seeds were reported to have size of 4 nm and smaller.[99] The important feature is that majority of the nanoparticles are single crystalline, and no multiple-twinned particles were observed by HR-TEM (Fig. 4.1b). Similar single crystals were reported for CTAB-stabilized $NaBH_4$-reduced gold nanoparticles with less than 5% of twinned nanoparticles.[102] The crystallinity of a seed is mainly determined by the reduction rate. When the reduction of Pd precursor and the generation of Pd atoms are extremely fast (as in the case of sodium borohydride as a reducing agent), most seeds become single crystals due to their rapidly increasing size.[76]

The shape of the nearly spherical particle is considered as cuboctahedron which has the smallest surface area to minimize the total interfacial free energy. Palladium is relatively unique as compared to other metals such as Ag; it's very difficult to form twinned seeds which are favored at small size for Pd. For example, the icosahedral and decahedral seeds are preferentially formed with the number of atoms $N<309$ and $309<N<561$, respectively.[76] The multiple twinned seeds will evolve into single crystal cuboctahedrons as they grow in size rapidly, since the low surface energy of (111) facets can no longer compensate for the excessive strain energy.[76] As shown by simulations, cuboctahedral seeds are favored for Pd if the number of atoms is greater than 561.[76, 103] Another theoretical study[104] indentifies that icosahedral is the most stable structure at small size of palladium, and the critical size for stable Pd cuboctahedrons is 1415 atoms. The size of the formed seeds in the present study is 3.0 nm which corresponds to 1289 atoms according to the crystal statistics.[7] Only 4% of seeds have less than 561 atoms, which allow concluding that the synthesized Pd seeds can be considered as cuboctahedrons. Repeated synthesis showed reproducible nanoparticles (Appendix A). Thus, the nanospheres S1 can be used for structure-sensitivity studies.

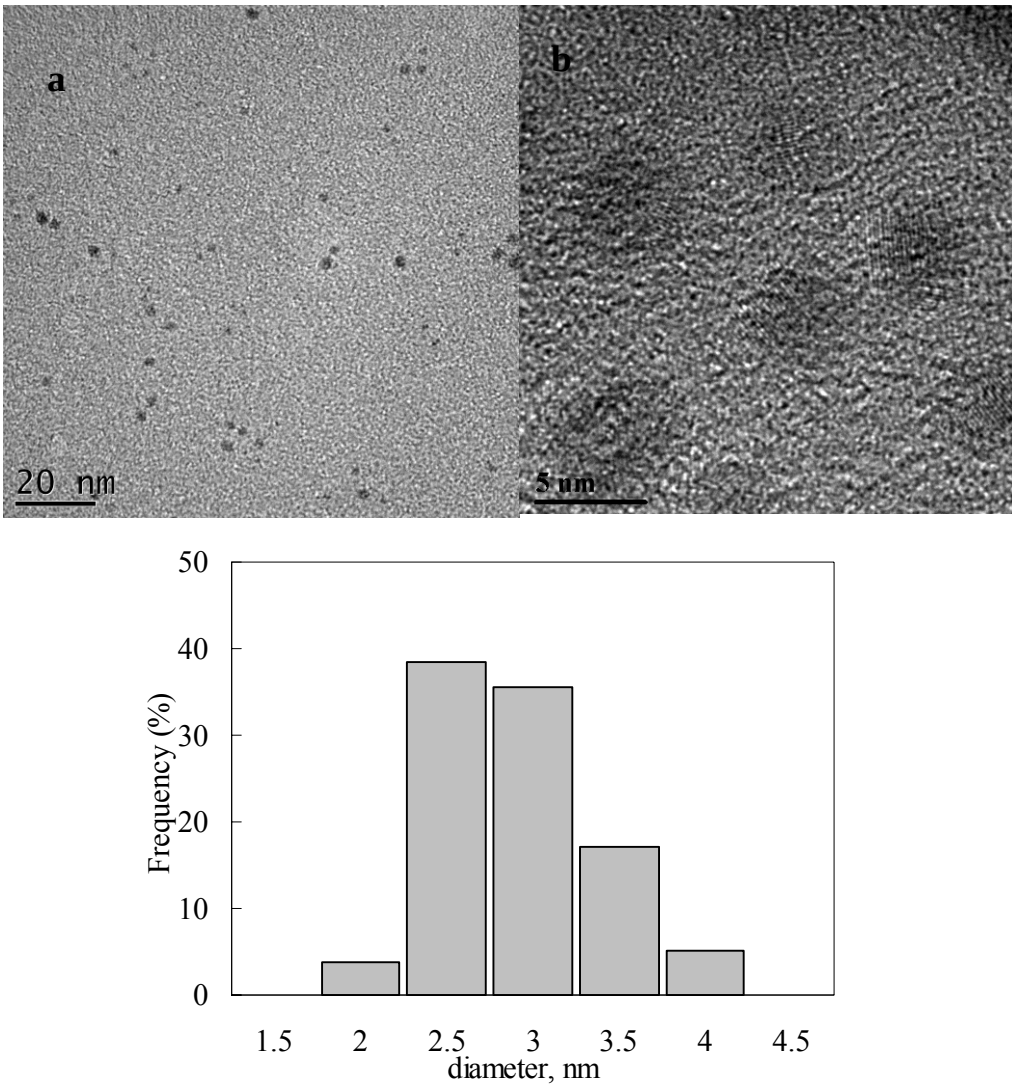

Figure 4.1. TEM (a) and HR-TEM (b) images of spherical (cuboctahedral) nanoparticles with corresponding size distribution histogram.

Nanoparticles S2-S5. Precise control of particle size is essentially required to obtain high performance materials. Seeding growth method was successfully used small nanoparticles as "seeds" for later stage particle enlargement.[72, 99, 101] In the present study, the Pd seed was synthesized by a fast reduction with borohydride. In the growth step, a weak reducing agent ascorbic acid and surfactant were used

to inhibit further nucleation. Figure 4.2 shows the TEM images of larger Pd nanoparticles with an obvious size increase from set A (S2) to C (S4) under the same scale. Set A (S2, average size ~ 6.7 nm) and B (S3, average size ~14 nm) were prepared from one-step seeding but varying seed to metal precursor ratio. The size of nanoparticles increased, but most of the particles in Set A and Set B were not spherical. The expected sizes for the Sets A and B based on the procedure developed for Au spheres are of 5.5±0.6 nm and 8.0±0.6 nm, respectively.[72] The difference could be attributed to the metal nature influencing the rate of nucleation and reduction. Set C (S3) was prepared using solution from set B as seed. The particle size increased to about 16.4 nm; however, a lot of seeds (small particles around 2-3nm) were observed at the same time. In the case of Au system, from which the method was adopted, nearly monodispersed spherical particles with diameter of 17±2.5 nm were produced and no seeds were reported. The big Pd particles in set C (S4) had a similar size comparing with Au particles but the shape was not spherical. Set D was prepared following the same procedure as Set A but with increased metal precursor concentration in the growth solution. In the case of gold nanoparticle, the method allowed to increase the quantity of produced spherical Au nanoparticles (2-20 mg).[72] In the present study, more Pd nanoparticles were obtained, but particles' size varies in a wide range from 3.8 nm to 13.6 nm and seeds were also formed during the growth step. Consequently, this particular seeding growth approach was not successful for larger Pd nanoparticles with uniform size and shape distribution, and the produced nanoparticles S2-S5 are not suitable for structure-sensitivity studies.

Repeated synthesis of S2 showed reproducible nanoparticles (Appendix A). The consecutive growth steps for S3-S5 were not repeated since the first step already failed to produce spherical nanoparticles.

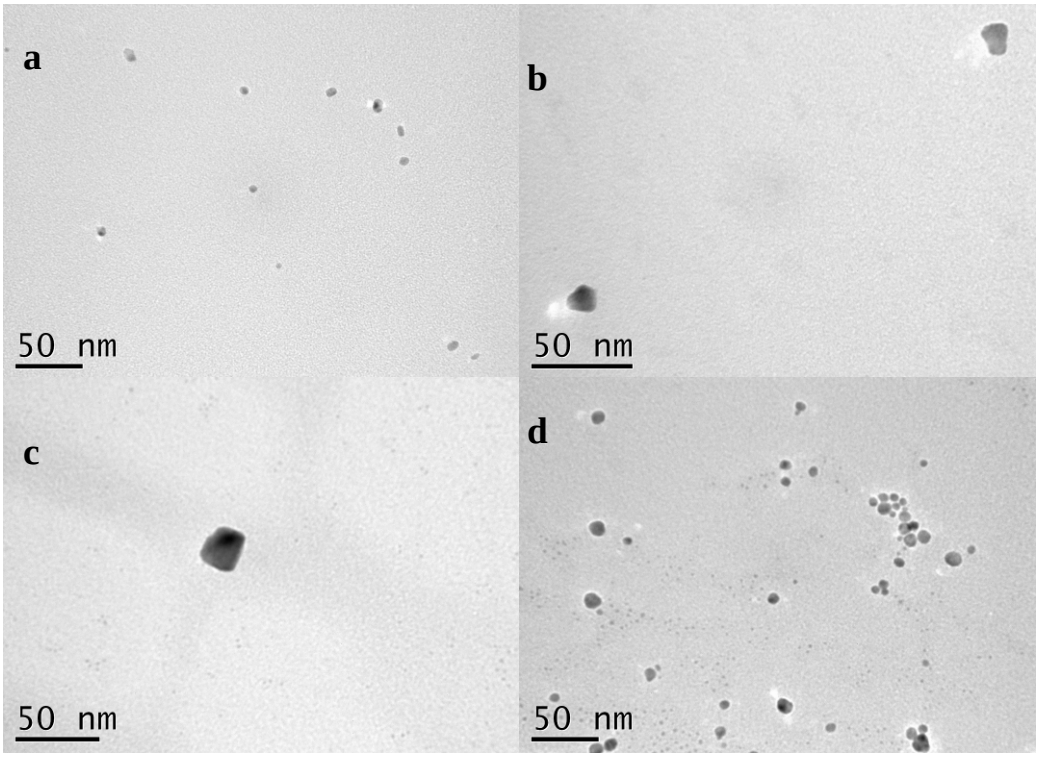

Figure 4.2. TEM images of larger palladium nanoparticles prepared from seeding growth method: set A (a), set B (b), set C (C), and set D (d).

Nanoparticles S6. Typical TEM images of Pd nanoparticles prepared in w/o microemulsion systems are shown in Fig 4.3. Hydrazine was used as reducing agent in both systems. S6 particles were expected to be spherical with size of 5.75±1.33 nm in diameter following the method developed by Wang et al.[83] (The size was reported for nanoparticles dispersed in microemulsion, not for isolated ones). For TEM imaging, *S6* particles were isolated from the microemulsion, deposited on corundum and desorbed from the support under ultrasonic treatment. Most likely, during the washing procedure the particles formed agglomerates of around 40~80 nm. As nanoparticle-containing microemulsions constitute a thermodynamically stable system, the difficulty of isolating nanoparticles from microemulsion without agglomeration is still a challenge in nanoparticle

preparation.[80] When the S6 nanoparticles were used without purification from microemulsion components in the current study, they allowed synthesis of nanoparticles of different shapes as reported below (section 4.1.2) confirming that only isolated nanoparticles agglomerate. Repeated synthesis of S6 showed reproducible nanoparticles (Appendix A). The S6 nanoparticles, thus, are not suitable for structure-sensitivity studies.

Nanoparticles S7 were prepared using a known w/o microemulsion technique for platinum with expected sphere size of 4.0 nm in diameter. The TEM sample was prepared using microemulsion directly. Comparing with *S6*, smaller particles (10~20nm) were obtained along with some big agglomerates, and the particles/agglomerates were polydispersed in size and shape. Both methods were repeated several times, monodispersed particles could not be obtained. The difference between S7 and expected size and shape was likely due to metal nature (rate of its nucleation and reduction). Repeated synthesis of S7 showed reproducible nanoparticles (Appendix A). The nanoparticles are not suitable for structure-sensitivity studies.

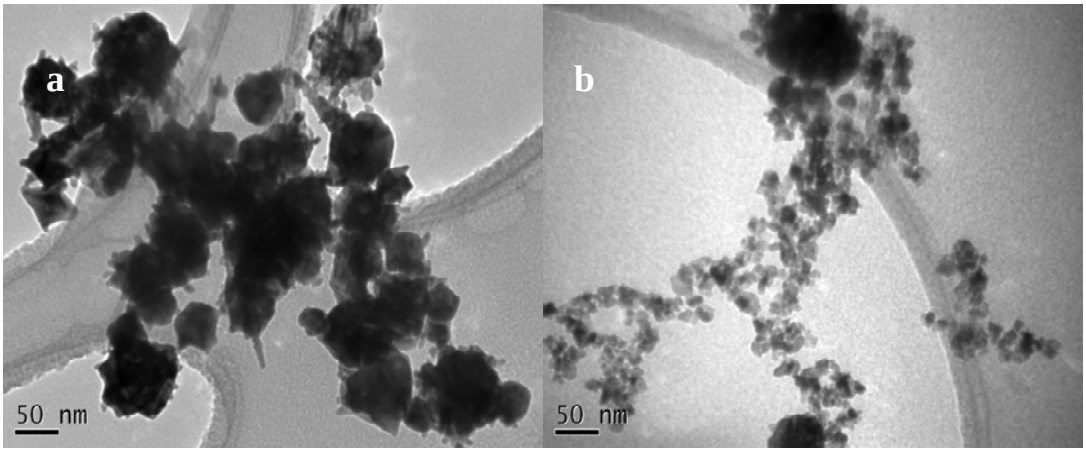

Figure 4.3. TEM images of Pd nanoparticles prepared from microemulsion methods: S6 (a), S7(b).

4.1.2 Seed-mediated synthesis of Pd nanocrystals (S8-S10)

Nanoparticles S8 were prepared following seed-mediated approach for Au system but using nanoparticles formed in microemulsion as seeds S6.[77] Fig 4.4 shows that the obtained particles were mostly anisotropic with a variety of shapes including rods, cubes, triangle, multiply twinned, and some other shapeless particles. Seeds S1 were not used as in an earlier study using Pd precursor and seeds S1, Berhault et al.[71] proved that a similar experimental protocol lead to the formation of a wide variety of Pd nanoparticles with morphology similar to these nanoparticles formed here. The surface statistics of nanoparticles cannot be easily applied since the morphology of most nanoparticles was not clear, so these particles are not suitable for structure-sensitivity studies.

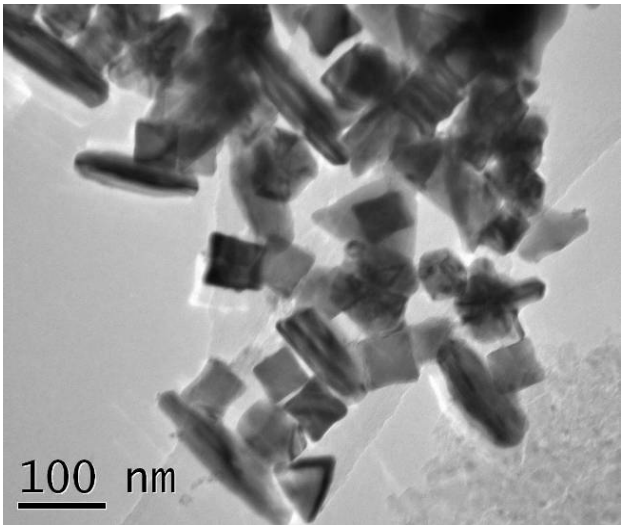

Figure 4.4. TEM images of Pd nanoparticles prepared from seed-mediated synthesis of nanohexagon S8: seed from microemulsion method (*S6*).

Nanoparticles S9 were prepared following the seed-mediated method using two different seed solutions S1 and S6, respectively (Fig 4.5). The hypothetical particle shape was cube with ~66 nm average edge length at ~85% yield obtained for Au using seed prepared the same method as S1.[77] In the case

of Pd nanoparticles produced from seeds S1 and S6, polyhedric particles were obtained with size between 50~110 nm. Moreover, these nanoparticles were not monodispersed. The obtained particles were prepared the same as the above "nanohexagons", except less ascorbic acid was used. Therefore, decreasing the concentration of AA led to more isotropic spheres-like particles. Again, no cube nanoparticles were observed which could attribute to the metal nature. The particles are not suitable for structure-sensitivity studies.

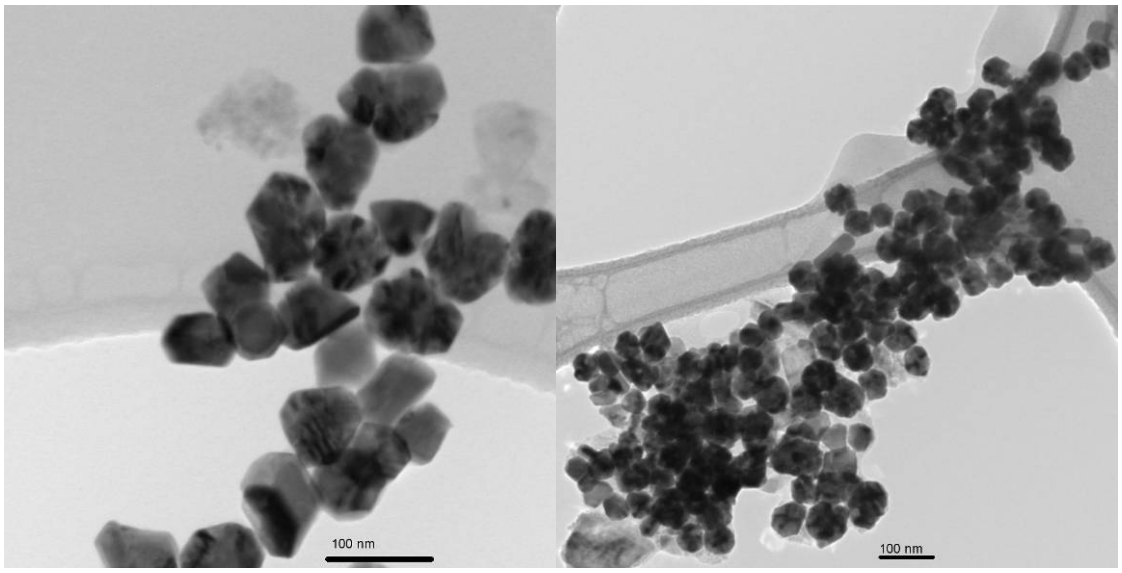

Figure 4.5. TEM images of Pd nanoparticles prepared from seed-mediated synthesis of cubes: seed from S1 (left), seed from S6 (right).

Nanoparticles S10 were prepared following the seed mediated method of Au nanorods.[94] The expected particles using S1 as seeds are nanorods with dimension of 50 (±6) × 10 (±2) at approximately 55 % yield. This seed-mediated approach applied to Pd led to a very low yield of rods (very few nanorods ~50 nm long were observed during TEM analysis) and tetrahedrons (~20 nm) as shown in Fig 4.6. The majority of particles were multiply twinned particles (~25 nm) and seeds (~3 nm) as can be seen. Again, the big difference of nanoparticle size and

shape with the expectation is likely due to the metal nature. In this case, 1.67 mL seed solution was used for synthesis which was over 100 times more than the seed solution used for cube and hexagon preparation. For palladium synthesis, it is possible that the excess seeds in the sample did not go through the growth step. In addition, multiply twinned particles may be prepared under the same condition with less seed solution, or by removing the seeds under centrifugation.

Since the same seed-mediated approach in the three syntheses (S8-S10) resulted in a variety of poorly defined nanoparticles, repeated syntheses of S8-S10 were not performed. Thus, none of the particles synthesized via seed-mediated growth are applicable for structure-sensitivity studies.

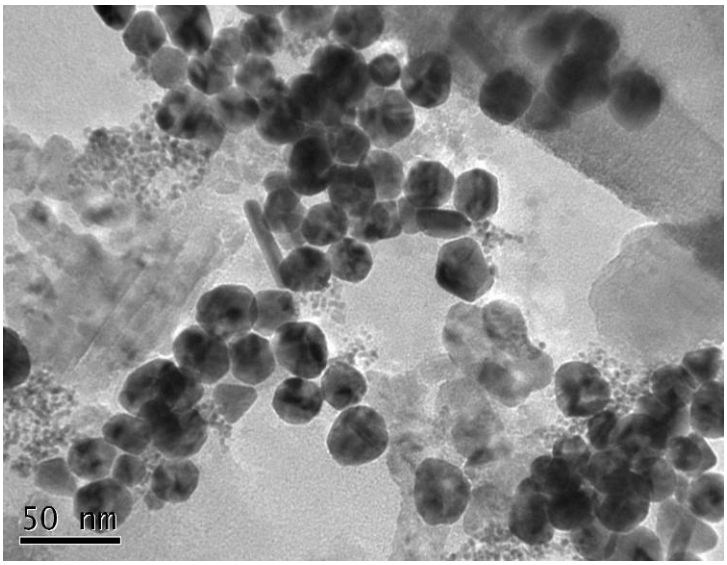

Figure 4.6. TEM images of Pd nanoparticles prepared from seed-mediated synthesis of nanorods S10: seed from S1.

4.1.3 Direct synthesis of Pd nanoparticles: nanocubes (S11)

Palladium nanocubes S11 were synthesized by reduction of H_2PdCl_4 with

ascorbic acid in the presence of CTAB at 95 ^{o}C.[101] Solution turned dark in 10 s after adding AA, indicating formation of particles. Synthesized samples of Pd cubes demonstrate high degree of shape monodispersity (Fig. 4.7). The image was obtained for the nanoparticles intentionally desorbed under ultrasound from corundum to verify their stability. More than 95% of all the particles are nanobars with the aspect ratio of 1.2±0.1 and long edge length of 19±2.2 nm (due to the low aspect ratio, further referred to as "cubes"). Electron diffraction patterns reveal *d*-spacing values of 0.19, 0.22, 0.14, and 0.116 nm corresponding to (200), (111), (220), (311) planes of f.c.c. Pd crystals[105], respectively. Other 5% are presented by nanobars with higher aspect ratio (~8), multiply-twinned particles, and tetrahedral particles of similar size (from 15 to 25 nm). No agglomerates (> 30 nm) or smaller particles (<10 nm) were observed, which allows applying surface statistics of the cubes to represent the surface atom statistics of the whole sample. The reduction process was fast, single crystal seeds would form as mentioned in the seeds section and then grew into cubes.[76] The synthesis was reproducible in nanoparticle size as the previous study reported cube size of 22 nm.[101] It has reported that during Pd[8, 97] or Au[77] nanocrystal growth in the presence of CTAB as a capping agent, the bromide ion binds more strongly to (100) faces than (111) faces. In the case of Pd nanocubes, the adsorbed Br^{-} decreases the growth rate of (100) faces. The face with a slower growth rate will exposed more on the nanocrystal surface. The fast formation and deposition of Pd^{0} onto the (111) faces leads to their disappearance and formation of (100) faces, thereby producing cubic shapes.

The nanoparticles S11 are suitable for structure sensitivity studies due to well defined shape and high degree of monodispersity. Repeated synthesis of S11 showed reproducible nanoparticles (Appendix A).

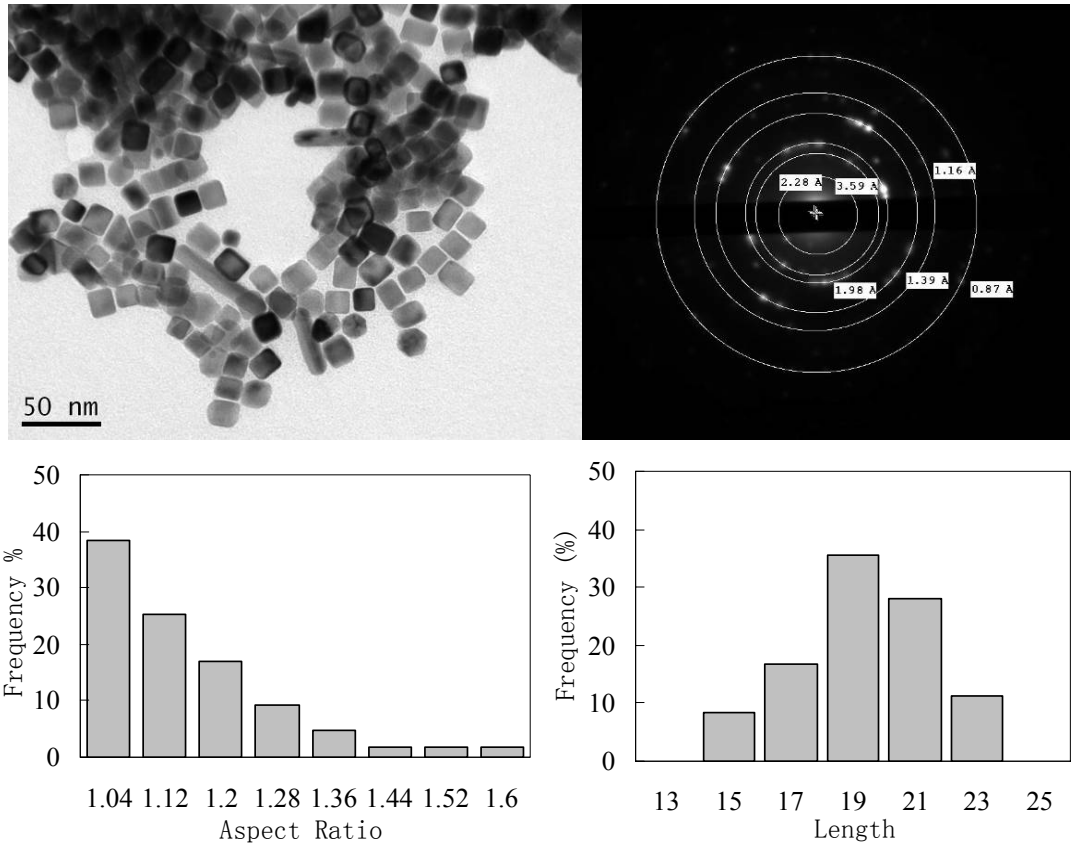

Figure 4.7. Palladium cubes S11: TEM (a) and electron diffraction (b) images; histograms of aspect ratios (c) and rib length distribution (d) for cubes.

4.1.4 Catalyst selection for structure sensitivity study

Similar to other noble metals, synthesis of Pd nanostructures with well controlled size and shapes has been a challenging task. A variety of nanoparticles were synthesized following existing methods for the same or different metal systems. The identification of structure sensitivity would be both impossible and useless if the synthesis method is not reproducible for generating metal nanoparticles with narrow size and/or shape distribution onto supports on a small scale and under controlled conditions. Among the synthesized nanoparticles, some samples are agglomerated or mixed with different shapes and wide size range; more importantly, most samples do not show well defined shapes, and surface

statistics can not be applied. The use of different metal precursors, stabilizer, or preparation condition may lead to catalysts that are intrinsically from each other besides in particle size and shape.[15, 25] Consequently, the sphere (S1) and cube nanoparticles (S11) synthesized in the presence of CTAB are chosen for the catalytic hydrogenation study. The monodispersed sphere and cube nanoparticles with well-defined shapes make the application of surface statistics easy and accurate. The well defined (100) facets on Pd nanocube surface make the Pd nanocube an ideal material for understanding the influence of the nanocrystal facets on catalytic performance. In order to elucidate the activities of (100), (111) planes and defect (edges and vertices) atoms, cubes of ~20 nm rib size will be used, as ~98% of their surface consists of (100) terrace atoms, and 3 nm spherical particles that possess well-represented (111), (100) surfaces and defect atoms. The catalytic reactions will be performed using supported nanoparticles due to easy heterogeneous catalyst handling.

4.2 Characterization on selected catalysts (S1 and S11)

More analysis was done on the selected sphere (S1) and cube (S11) catalysts before and after the catalytic reactions.

4.2.1 TEM analysis

TEM results of the unsupported spheres and cubes nanoparticles were discussed in section 4.1. Fig. 4.8 shows the TEM images of the cubic and spherical nanoparticles on the α-Al_2O_3 support. The nanoparticles do not show any obvious agglomeration and/or shape and size change on the support. Washing and depositing step did not make nanoparticles agglomerate. The nanoparticles are not distributed uniformly on the support, which however does not pose any restrictions for the structure-sensitivity studies as they will be performed at

temperatures low enough to prevent sintering of neighboring nanoparticles.

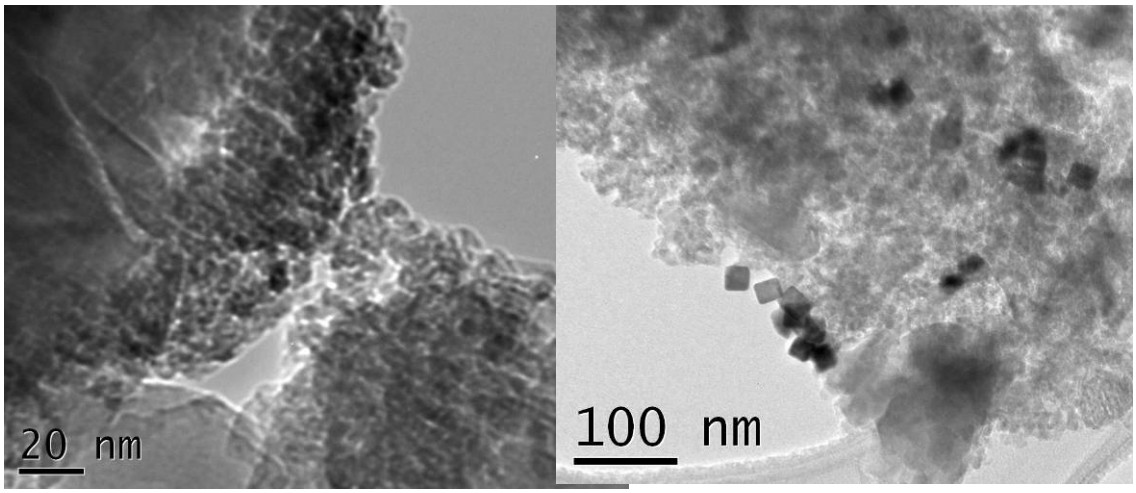

Figure 4.8 TEM image of nanoparticles on support: Sphere (left), cube (right).

As cubic shape is not as thermodynamically favorable as the spherical one, and cubes are more prone to Ostwald ripening as compared to the spheres, the nanocubes were observed after a catalytic reaction after intentional ultrasound-assisted desorption. Fig. 4.9 demonstrates the TEM image with corresponding size distribution histograms of Pd nanocubes after one 1-hr catalytic hydrogenation of MBE at 313 K. The cubic particles were preserved in the catalyst, and no spherical particles were observed. The edge length aspect ratio of cubes changed from 1.2±0.1 to 1.1±0.1, and the cube rib length from 19±2 nm to 19.6±2 nm. As no more particles with aspect ratios of 1.4-1.6 were observed, these findings indicate the transformation of nanobars with low aspect ratios to cubes during the catalytic reaction. These changes are not as dramatic as were observed for an electron-transfer reaction with cubes,[106] probably due to the shorter reaction time and reaction nature. As the reaction rates at 1 hr reaction time were found to have the same values as the rates at 10% conversion, the surface statistics of the cubes after 1 hr reaction were used to calculate TOFs.

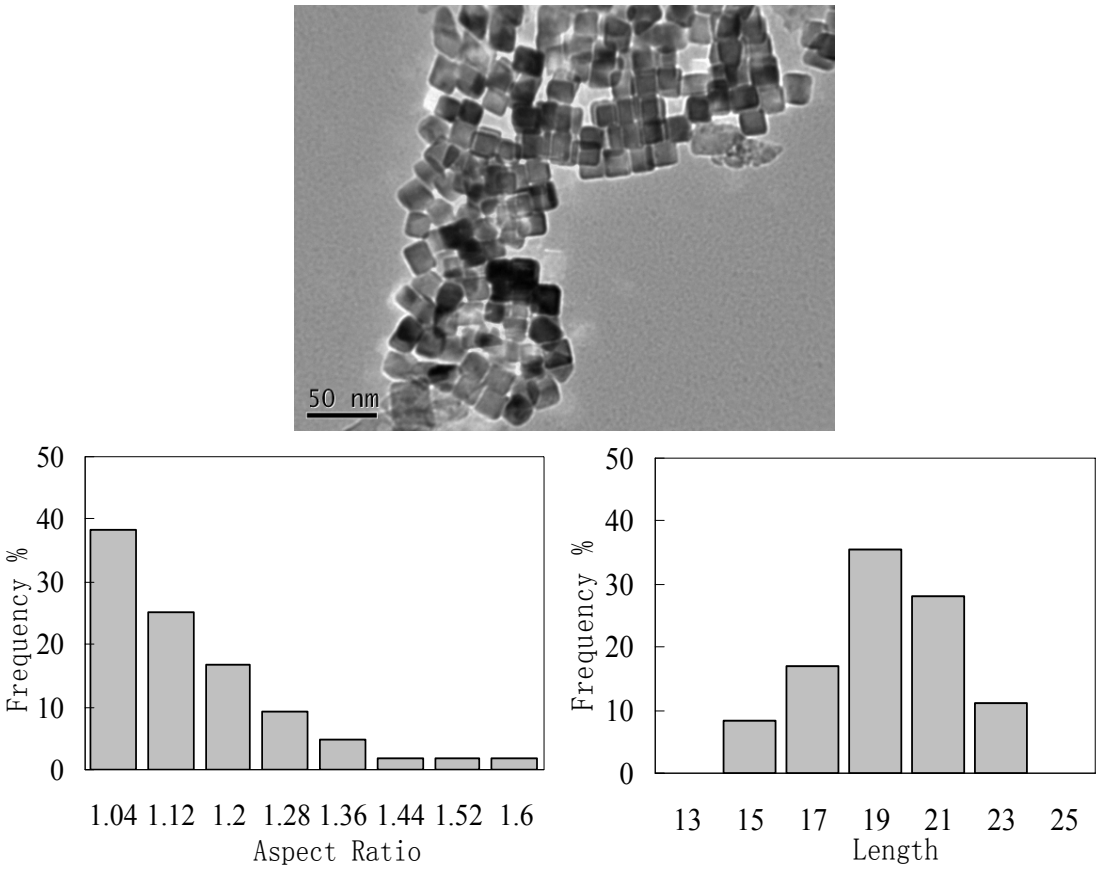

Figure 4.9. TEM image with corresponding size distribution histograms of Pd cubes after one 1-hr catalytic reaction at 313 K.

4.2.2 AAS analysis

Table 4.1 shows the AAS results of catalysts used for MBE and MBY hydrogenations. Based on the atomic absorption analysis, the Pd loadings on the cube-supported and sphere-supported catalyst were estimated as 0.11 ±0.02 wt% and 0.0195 ±0.0005 wt%, respectively, depending on the catalyst batch. The cube-supported catalyst has a higher loading but the dispersion of the cubes is ~6-fold lower than that of the spheres. As a result, the different loading of Pd catalysts yielded approximately the same surface Pd atom loading, which allowed similar kinetics and effects of mass transfer.

Pd loading of both catalysts after reactions was also tested to determining the leaching of nanoparticles during MBE hydrogenation reaction. The AAS result showed 34±9 % of Pd leached during the reaction with cubes, and 42% during the reaction with spheres. Although the supported catalyst was washed with methanol several times before the reactions, leaching problem still occurs during reactions. The reactant MBE is an amphiphilic molecule which could promote leaching of the surfactant-stabilized nanoparticles.[6]

MBY hydrogenation is known to proceed with almost an order of magnitude higher rate than MBE hydrogenation over Pd catalysts, so for the MBY hydrogenation lower loadings would be beneficial to decrease probability of liquid-solid mass transfer limitations. For the MBY hydrogenations, the cubic and spherical supported catalysts were washed copiously with hot ethanol, which resulted in lower loadings (Table 4.1) but were less prone to leaching during the reactions. As seen, for MBY hydrogenations, the Pd loadings on the cube-supported and sphere-supported catalyst were estimated as 0.041±0.00004 wt% and 0.027±0.00001 wt%, respectively. The catalyst after one hour reaction was also tested by atomic absorption to check the leaching during MBY reaction. The result showed no significant Pd leached (3.3±0.03%) during the reaction with cubes, and around 12±0.008% of Pd leaching during the reaction with spheres.

Table 4.1. AAS result for catalyst used in MBE and MBY reactions.

Supported catalyst	Loading wt% (MBE)	Leaching % (MBE)	Loading wt% (MBY)	Leaching % (MBY)
Cube	0.11 ±0.02	34±9	0.041±0.004	3.3±2.5
Sphere	0.0195 ±0.0005	42	0.027±0.001	12.0±0. 8

4.2.3 XPS and BET analysis

The surface composition of the two standard prepared catalysts for MBE hydrogenation is presented in Table 4.2 (Detailed XPS result is shown in Appendix B). The loading of the cube-supported and sphere supported catalyst were 0.041% and 0.014% from AAS result, respectively. Pd surface mass concentrations of both samples were found to be 5 wt% which exceeded their loadings by two orders of magnitude. XPS usually measures top 1-10 nm of samples for surface elemental composition. The high Pd surface concentration indicates Pd enrichment at the catalyst surface. XPS result verified the absence of Cl, B and N in both catalysts, confirming that the washing procedure effectively removed the CTAB cation, chlorine from Pd precursor and sodium borohydride. Br was still detected for both catalysts with Br to Pd surface concentration ratios of 0.2 and 0.8 for cubes and spheres, respectively. These ratios indicated 99.9% of Br^- from surfactant CTAB used to prepare nanoparticles was removed. Br^- ions are known to chemisorb onto the (100) facets of metal crystal and promote their development.[8, 77] Therefore, some Br^- remained on the nanoparticle surface and stabilized them from aggregation.

Table 4.2. Results of elemental surface composition by XPS for sphere-supported catalyst (0.014% Pd loading) and cube supported catalyst (0.041% Pd loading).

peak	Position BE (eV)	Cube, mass conc %	Spheres, mass conc %
Na	1070.44	3.07	1.12
F	686.84	1.3	1.22
O	530.39	45.14	40.28
N	400.89	0.38	0
Pd	335.09	5.43	5.08
C	284.69	15.39	21.75
Cl	205.59	0.09	0.13
B	198.24	0.2	0.34
Br	180.74	0.96	3.39
Al	118.44	28.03	26.13

The corundum support was found to have the BET surface area of 2 m^2/g and pore diameters between 2 and 20 nm (Table 4.3). The detailed pore size distribution is shown in Appendix D. Thus, Pd nanocubes are relatively large, can be located only at the external surface, forming egg-shell structure. According to the XPS results (surface enrichment with Pd), similar catalytic behavior of the cubic and spherical particles, as well as TEM results (Fig. 4.8), the Pd spheres are also located on the external corundum surface.

Table 4.3. BET surface area, mesoporous volume and pore diameters of catalyst support

	BET surface area (m^2/g)	Mesoporous volume (cm^3/g)	Pore diameter average (nm)
$\alpha-Al_2O_3$	2.32	$4.64x10^{-3}$	2-20

4.2.4 XRD analysis

The XRD patterns of pure CTAB, as-synthesized Pd spheres and Pd cubes are shown in Fig. 4.10. The prepared XRD sample of nanocubes was washed with methanol to remove excess CTAB. Five peaks are shown on the nanocube XRD pattern (CTAB peaks are negligibly small), which represents (111), (200), (220), (311), and (222) facets. All of the peaks can be indexed to face-centered cubic (fcc) bulk Pd metal (Joint Committee on Powder Diffraction Standards (JCPDS) card no. 05-0681). The absence of other diffraction peaks other than Pd metal indicates that this material was synthesized successfully as a pure phase. The intensity ratio of peak (111) to (200) was calculated as 1.7 for nanocubes, where as conventional bulk Pd powder shows a ratio of 2.38.[97] This is reasonable since the catalyst contains mostly nanocubes which have the highest amount of (100) faces.

The Pd spheres show almost the same XRD pattern as CTAB. Partially, it is due to the prepared XRD sample contained fairly large amount of CTAB since it was not feasible to isolate unsupported nanospheres from the CTAB without agglomeration. It is known that as the crystal size decreases, the XRD peak gets broader and shorter. The as-synthesized nanospheres are single crystals around 3 nm from HRTEM result. Therefore, XRD reflection is very poor for the Pd nanospheres. As an example, the Pd (111) reflection shows a hump instead of a peak.

Scherrer equation was also used to estimate the average Pd crystal size.[107]

$$d = \frac{K\lambda}{\beta \cos(\theta)} \tag{22}$$

where d is the crystal size in nm; K is the shape factor, a constant usually taken as 0.9; λ is the wavelength of x-rays, nm; β is the line broadening at half the maximum intensity (FWHM) in radians of 2θ; θ is the bragg diffraction angle. A detailed calculation of crystal size is shown in Appendix D. The calculation

yielded an average value of 16.4 nm for Pd cubes excluding the instrumental broadening errors. The calculated crystal size may be smaller or equal to the grain size since there are other factors that contribute to the width of a diffraction peak. From the TEM results, the edge length of nanocubes varies from 15 nm to 23 nm. Therefore, the cubes are most likely single crystals which had been proved in previous study by selected area electron diffraction pattern of a single Pd nanocube.[101]

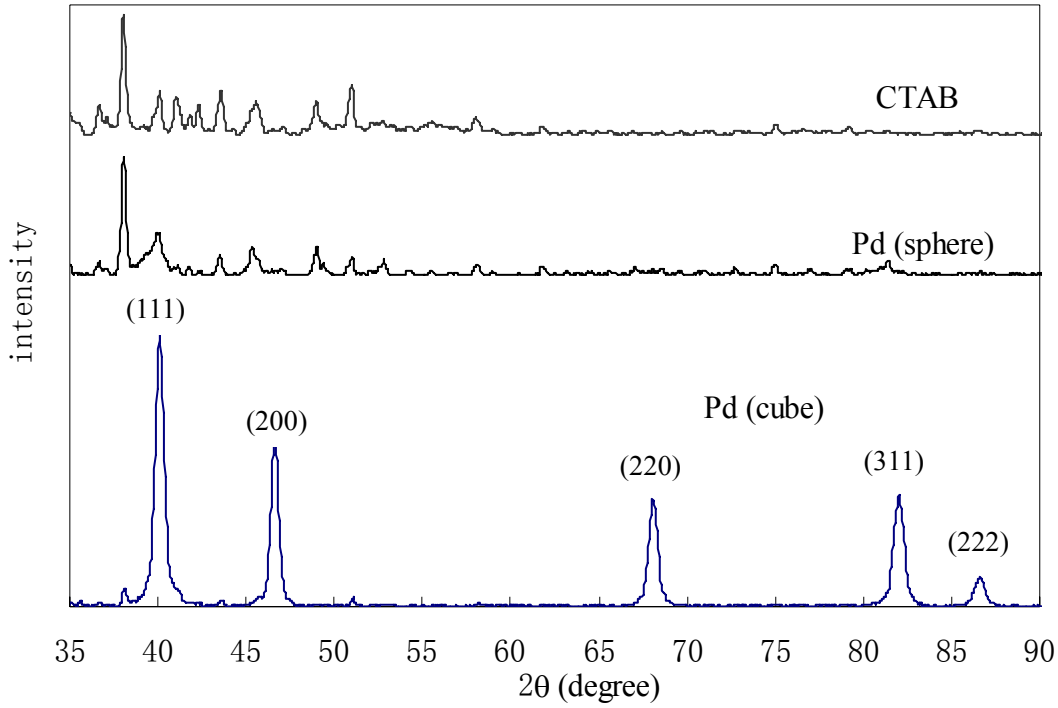

Figure 4.10. XRD patterns of CTAB, as-prepared non-deposited Pd nanospheres and nanocubes.

4.3 Results and discussions on structure sensitivity studies of MBE hydrogenation

4.3.1 Analysis of Heat and Mass transfer

It is critical to make sure the reaction is free of both external and internal mass and heat transfer limitations for a reliable hydrogenation kinetics study. Because the heat capacities and thermal conductivities of the liquid phase is much higher than that of vapor phase, the heat transfer limitations (i.e. temperature gradient between liquid and catalyst surface) are usually negligible in liquid phase reaction as compared to vapor phase reactions.[44] As previously shown for MBY hydrogenation using $Pd/CaCO_3$ catalyst, the difference between bulk liquid and catalyst surface is 0.03 K at 333 K reaction temperature, which is negligibly small.[29] The current study was therefore assumed operating under isothermal conditions.

Next, it is important to prove that reaction rate is not controlled by mass transfer. Typically, stirring speed test is used to check the gas-liquid mass transfer resistance of hydrogen from the gas phase to the bulk liquid phase, and reaction rate remains constant with changing stirring speed indicates absence of external gas-liquid mass transfer limitation.[44] The reactions were carried out with cube-supported catalyst at 313 K, 0.45 MPa absolute H_2 pressure, with 0.69 g MBE in ethanol (0.04M). The stirring speed was varied in the range of 250–1,700 rpm and catalyst loaded in the reactor varied from 0.05 to 0.13 g. Table 4.4 lists the reaction conditions. The reaction rates of the five experiments with cubic Pd nanoparticles were found to be 7.9±0.2 $mol_{H2}/(mol_{Pd}·s)$, indicating the absence of gas-liquid mass transfer limitations under these conditions. It should point out that a low stirring speed as 250 rpm is usually not enough to promote efficient mass transfer. In this case, most likely the stirrer design (hollow gas entrainment

impeller) and natural baffling system in the reactor (a gas-inducing dip tube, a cooling coil and a thermocouple) promoted the mixing. The stirrer manufacture indicates that the gas entrainment impellers operate best in the 800 - 1200 rpm range; therefore, the stirring speed was set to 1200 rpm for the following reactions.

Table 4.4 Reaction conditions for MBE hydrogenation.

Temperature	313 K
Pressure	0.45 MPa
MBE conc.	0.040 M
Agitation	1200 rpm
Total liquid volume	200 cm^3
Solvent used	Ethanol

Liquid-solid external mass transfer

To get the true kinetic data, the diffusion of the reagents from liquid phase to the catalyst surface should not interfere with the reaction kinetics. As MBE (and MBY) hydrogenations are considered fast even at low pressures, the concentration of hydrogen in the liquid phase may be not high enough (due to its low solubility) to ensure sufficiently fast liquid to solid mass transfer of the gas phase reagent. Similarly, the liquid reactant (MBY or MBE) may become a limiting reactant at high conversions, as was shown previously for MBY hydrogenation over $Pd/CaCO_3$ catalyst.[29]

There is no direct way of ensuring the absence of liquid-solid mass transfer limitations,[108] but it can be evaluated using Carberry number.

Carberry number (Ca) is calculated to check the absence of external liquid-solid mass transfer limitations for both hydrogen and MBE. Ca is the ratio

of observed reaction rate to the maximum mass transfer rate[108]:

$$Ca_{LS} = \frac{r_{obs}}{k_{LS} \cdot a_s \cdot C_b} \tag{23}$$

where r_{obs} is the observed reaction rate in mol/s·g_{cat}; k_{LS} is the liquid solid mass transfer coefficient in m/s; a_s is the external specific surface area of catalyst in m^2/g_{cat}; C_b is the bulk concentration of a reagent mol/m^3. The external specific surface area is the calculated from catalyst particle surface area over particle mass:

$$a_s = \frac{A_p}{m_p} \tag{24}$$

where
$$A_P = 4 \cdot \pi \cdot \left(\frac{d_p}{2} \right)^2, \tag{25}$$

and
$$m_P = \frac{4 \cdot \pi \cdot \left(\frac{d_p}{2} \right)^3}{3} \cdot (1-\varepsilon) \cdot \rho_p \tag{26}$$

where d_p is the particle diameter of 150 μm (provided by supplier) and corundum density of 4 g/cm^3. a_s is calculated as 0.01 m^2/g. Henry's law was used to estimate the bulk concentration of hydrogen in ethanol, $C_{H2,b}$, at 0.45 MPa absolute pressure with Henry's law constant of 470 MPa at 313 K.[109] The bulk concentration of MBE was estimated as 36 mol/m^3 at 10% conversion when the reaction rate was determined. The observed reaction rate for the cube- and sphere-supported catalysts were 1.00×10^{-6} and 2.39×10^{-6} mol/(s·g_{cat}), respectively.

Mass transfer coefficient of suspended particles in stirred vessel can be correlated with Sherwood number (*Sh*) which has a 30% standard deviation.[110]

$$k_{Ls} = \frac{Sh \cdot D_{A,B}}{dp} \tag{27}$$

$$Sh = 2 + 0.4 \cdot \left(\frac{N_p \cdot l^5 \cdot n^3 \cdot {d_p}^4 \cdot \rho^3}{V_L \cdot \mu^3} \right)^{\frac{1}{4}} \cdot Sc^{\frac{1}{3}} \quad (28)$$

where Np is the power number estimated as 8.5[111] for the gas entrainment impeller; V_L is the liquid volume in m^3; the ethanol density ρ and ethanol viscosity μ are 772 kg/m^3 and 8.24×10^{-4} pa·s at 313K,[112] respectively. The impeller diameter l is 0.030 m. The reactor operated at 1200 rpm which was 125.7 rad/s for the angular velocity, n. The Schmidt number Sc is defined as

$$Sc = \frac{\mu_B}{\rho_B \cdot D_{A,B}} \quad (29)$$

where $D_{A,B}$ is the molecular diffusivity of component A into component B. Wilke and Chang's correlation can be applied for hydrogen (A) dissolved in ethanol (B):[113]

$$D_{A,B} = 1.1728 \times 10^{-16} \frac{T\sqrt{x_B M_B}}{\mu_B V_A^{0.6}} \quad (30)$$

where T is the reaction temperature of 313 K; x_B is the solvent association factor which is 1.5 for ethanol;[113] M_B is the molecular weight of ethanol as 46.0 g/mol; V_A is hydrogen molar volume at its normal boiling temperature, 0.0286 $m^3/kmol$.[17] $D_{H2,ethanol}$ was estimated as 3.1×10^{-9} m^2/s.

The molecular diffusivity of MBE in ethanol was estimated using Stokes-Einstein equation and assumed to be similar to that of the unsaturated alcohol 3-methyl-1-pentyn-3-ol, $0.8 \cdot 10^{-9}$ m^2/s at 297.5 K.[114] Applying the following equation and ethanol viscosities at 298 and 313 K,[112] $D_{MBE,ethanol}$ was estimated as 1.1×10^{-9} m^2/s.

$$\frac{D_{A,B} \cdot \mu_B}{T} = const \quad (31)$$

A value of the Carberry number less than 0.05 indicates that the rate of diffusion of a reagent at the liquid/solid interface does not affect the reaction

kinetics. Table 4.5 shows the results of the parameters for Ca calculations, each of the *Ca* number satisfies the condition of the absence of liquid-solid mass transfer limitations (*Ca* < 0.05). The errors for Ca are based only on the 30% standard deviation in Sherwood number.

Table 4.5a. Calculations of Carberry number for reaction with cube-supported catalyst.

	H_2	MBE
r_{obs}, mol/s·g_{cat}	1.00×10^{-6}	1.00×10^{-6}
C_b, mol/m^3	16.4	36.0
$D_{in\ ethanol}$, m^2/s	3.12×10^{-9}	1.10×10^{-9}
Sh	87	100
k_{LS}	1.81×10^{-3}	7.36×10^{-4}
$Ca_{L\text{-}S}$	**0.003±0.001 (<0.05)**	**0.004±0.001 (<0.05)**

Table 4.5b. Calculations of Carberry number for reaction with sphere-supported catalyst.

	H_2	MBE
r_{obs}, mol/s·g_{cat}	2.39×10^{-6}	2.39×10^{-6}
C_b, mol/m^3	16.4	36.0
$D_{in\ ethanol,}$ m^2/s	3.12×10^{-9}	1.10×10^{-9}
Sh	87	100
k_{LS}	1.81×10^{-3}	7.36×10^{-4}
$Ca_{L\text{-}S}$	**0.008±0.003 (<0.05)**	**0.009±0.003 (<0.05)**

Internal diffusion limitations

Wheeler-Weisz modulus (M_w)[51] is usually used to evaluate the influence of

pore diffusion on the catalytic reaction.

$$M_W = \frac{r_{obs} \cdot \rho_c \cdot L^2}{D_{eff} \cdot C_S} \tag{32}$$

where r_{obs} is the observed reaction rate; ρ_c is the catalyst density, 4 g/cm^3; L is the characteristic length typically defined as V_p/A;[51] C_s is the reactants' concentrations at the catalyst surface which can be assumed equal to their bulk concentrations since there was no external mass transfer limitation,[17] and D_{eff} is the effective diffusivity. Hydrogen concentration was determined by Henry's Law. The effective diffusivity D_{eff} was estimated as $D_{eff}=0.1 \cdot D_{2\,1}$, m^2/s.[108]

Under the above assumptions, M_W for the cube-supported catalyst was estimated as 0.5 and 0.6 for hydrogen and MBE, respectively, and 1.2 and 1.5 for the sphere-supported catalyst, indicating severe internal mass transfer limitations (>0.15).[51] However, the characteristic length L is considerably lower due to their egg-shell structure. It can be assumed close to 0 for both catalysts as discussed in section 4.2.3, resulting in zero Wheeler-Weisz modulus. We intentionally selected corundum for the catalyst support as it a nearly non-porous material. The above results indicated the absence of internal mass transfer limitations for reaction with sphere-supported catalyst due to its low characteristic length. Consequently, the chosen reaction conditions allow intrinsic kinetic studies.

4.3.2 Typical MBE reaction behavior

Typical kinetic curve of MBE hydrogenation carried out at constant hydrogen pressure is present in Fig. 4.11. Sphere catalyst shows much stronger activity than the cube catalyst. Hydrogen is consumed very fast in the first 3 minutes due to the hydrogen dissolution in ethanol. Then hydrogen consumption in both cases slows down and increases linearly with time indicating zero order with MBE. This can be explained only if C_{MBE} in Eqn (12) cancels out due to $K_{MBE}C_{MBE} >>$

$1+K_{MBA}C_{MBA}+K_H^{1/2}C_{H2}^{1/2}$ and first power in denominator instead of second power. This could be possible if two types of active sites existed on catalyst surface. However, it was not a purpose of the current work to perform kinetic modeling.

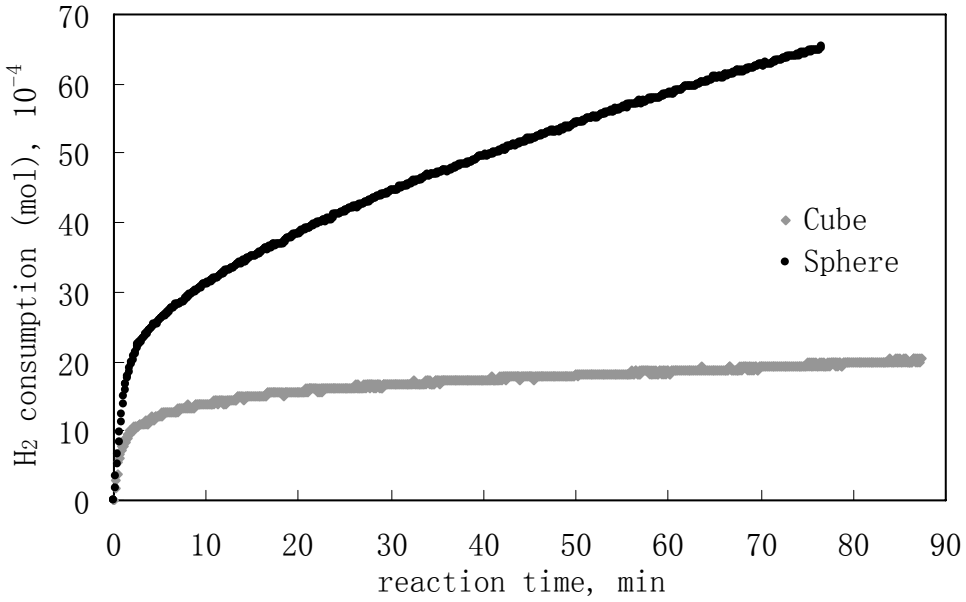

Figure 4.11. Hydrogen consumption as a function of reaction time for MBE hydrogenation with cube-supported (0.13% Pd loading) and sphere-supported (0.02% Pd loading) catalyst. Reaction condition: 0.45 MPa absolute pressure, 313K, 1,200 rpm, 0.04 M MBE, 200 mL ethanol, MBE-to-Pd molar ratio of 8,300.

4.3.3 Turnover frequencies (TOFs)

In the current study, reaction rates, TOFs and apparent activation energies were all determined at 10% conversion of MBE. As the shape of anisotropic particle can change in catalytic reactions due to Ostwald ripening,[9, 106, 115] shape and size of initially loaded cubic nanoparticles should be known at 10% conversion to correlate the surface statistics with the activity. As the reaction rates at 1 hr reaction time were found to have the same values as the rates at 10%

conversion, the surface statistics of the cubes after 1 h reaction is used to calculate the TOF. The size and shape of the cubic particles was discussed in section 4.1.3.

Both spheres and cubes nanoparticles show good monodispersity; consequently, the surface statistics can be applied from the known statistics of f.c.c. metal crystals of cubic and cuboctahedral shapes.[5, 7] A cube with an average two-dimensional size of 19x21 nm was found to have similar surface statistics as an equivalent cube with 20 nm edge length within 5% error. For simplicity, the following calculations are based on an ideal cube with 20 nm edge length. Fig. 4.12 shows the dispersion and related surface atom statistics of both nanoparticles. Dispersion is defined as the fraction of atoms of a material exposed to the surface, expressed as $D=N_s/N_t$. Dispersion is important is heterogeneous catalysis, since only surface atoms are able to play a role in catalytic surface reactions. From Fig. 4.12, the dispersion of spheres is 6 times higher than that of cubes. Cuboctahedrons are enclosed by (111) and (100) facets, whereas all the six faces of cubes are enclosed by (100) planes. The relative amount of (100) atoms with respect to the total and surface atoms is 6 and 98% for the cubes, respectively, and 4 and 11% for the spheres.

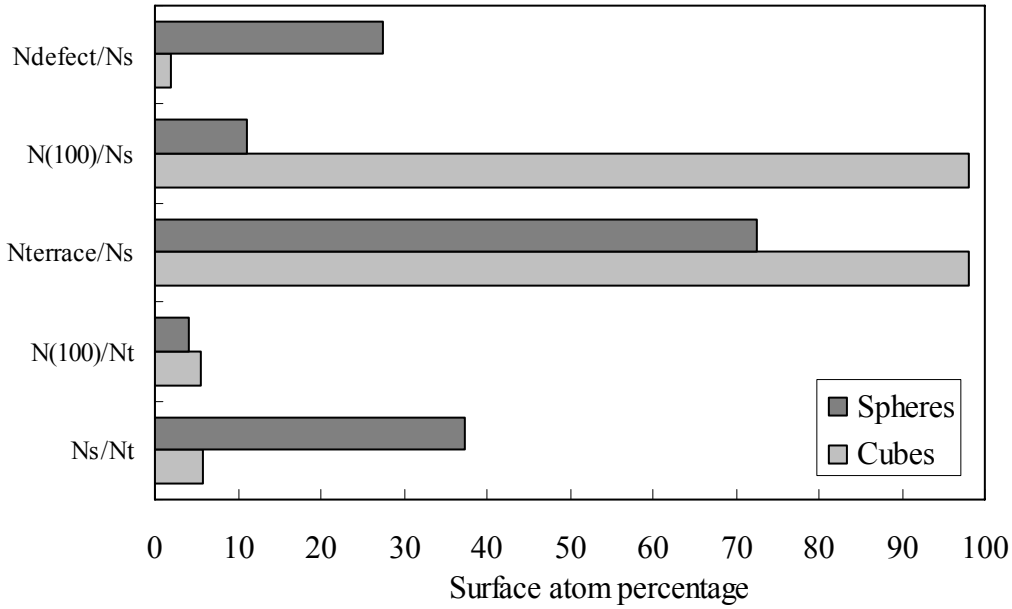

Figure 4.12. Surface atom statistics of the average synthesized cubes and spheres. N_S denotes number of surface atoms; N_T – total atoms; $N_{terrace}$ –atoms on (100) and (111) facets; $N_{(100)}$ – atoms on (100) facets, and N_{defect} – atoms on vertices and edges.

The nanoparticles are supported on the α-Al_2O_3, which means not all surface atoms are available for reactions. To calculate TOFs, one plane of (111) for sphere and one plane of cube were assumed to be attached to the catalyst support. Leaching is also considered into the calculations. The leached nanoparticles are considered as unsupported particles, which mean all the surface atoms are exposed. As discussed in AAS result, 34±9 % of Pd leached during the reaction with cubes, and 42% during the reaction with spheres.

Detailed calculations of TOF are shown in Appendix E both for spheres and cubes. For reactions at 313 K, the TOFs per total surface atoms were calculated as 2.59±0.07 s^{-1} for the cubes of 20 nm, while for the spheres of 3 nm as 3.87±0.02 s^{-1}. This shows the TOF does not increase with the increasing size of nanoparticle due to the elimination of steric limitations. As an opposite case, a study showed that the TOFs increased with increasing average nanoparticle size for

2-methyl-2-propen-1-ol and crotyl alcohol hydrogenations over Pd spheres of 2.6 - 5.1 nm diameters.[13]

Some catalytic studies of well-defined metal nanoparticles correlate TOFs with the nanoparticle surface statistics.[31] In the present study, TOF was also calculated as per all kinds of surface atoms on cubes and spheres in order to find out any particular atoms are single active sites for MBE hydrogenation. If TOFs calculated per number of specific surface atoms do not change with the surface composition, these atoms are assumed as active sites.[12, 25, 116] Therefore, if any surface atom shows the same TOFs of both cube and sphere, this kind of atoms should be the active sites. Table 4.6 lists the TOFs calculation results and shows no TOF values match between cube and spheres; consequently, none of the specific atom kinds can be considered as single active sites. This demonstrates that spheres possess at least two types of active sites, one being (100) atoms similar to the cubes, and the another one including (111) atoms and/or nanoparticle vertex and edge atoms, which possesses higher activity than (100) atoms. Various active sites were proposed in literature for allyl alcohol hydrogenation, such as terrace atoms of Pd spheres of 1.5 – 1.9 nm diameter[12] or defect sites (vertex and edge atoms) of Pd spheres of 2.6 - 5.1 nm diameter.[13] The latter low-coordination sites are generally known to display higher reactivity than flat terraces for catalysis;[117] however, in hydrogenations, too strong adsorption of a reactant to the atoms of low coordination number leads to their diminishing activity.[19] It should be noted that (100) atoms on 3 nm spherical particles can display different activities as (100) atoms on 20 nm cubes due to size effect.[12]

Table 4.6. TOF calculations per specific atoms on the cube and sphere surfaces according to the surface statistics.[7]

	Sphere	cube
Reaction rate[#], mol H_2/(molPd·min)	80.4±0.3	7.90±0.2
TOF**, mol H_2/(molPd$_{surf\ atm}$·s)	3.87±0.02	2.59±0.07
TOF$_{(100)}$**, mol H_2/(molPd$_{(100)}$·s)	31.99±0.06	2.64±0.07
TOF$_{(111)}$**, mol H_2/(molPd$_{(111)}$·s)	5.84±0.02	N/A
TOF$_{terrace}$**, mol H_2/(molPd$_{terrace}$·s)	4.94±0.02	2.64±0.07
TOF$_{defect}$**, mol H_2/(molPd$_{defect}$·s)	13.09±0.05	133±3

[#] Reaction conditions: 313 K, 0.45 MPa absolute pressure, 1,200 rpm, 0.04 M MBE, 200 mL ethanol, MBE-to-Pd molar ratio of 8,300. The reaction rate and TOF values are within 3% experimental error.

** The values are calculated based on the assumption that these specific atoms are single active sites; different TOFs for the sphere and cubes prove that none of the atoms types are active sites.

In the present study, the catalysts were prepared using the same stabilizer agent and following the same washing procedure in order to minimize the effect of any impurities. The XPS analysis shows both catalysts contain Br^- residuals from CTAB with surface Br-to-Pd weight ratios of 0.2 and 0.7 for cubes and spheres, respectively. It is known that Br^- adsorbs selectively on (100) faces stabilizing nanoparticles against agglomeration and promoting cube formation,[8, 77, 97] but at the same time, it may also lead to active site poisoning. From surface statistics, 98% surface atoms of cube are (100) surface atoms, which is almost 9 times higher than that of spheres (Fig. 4.12). If the (100) surface atoms are completely poisoned by Br^-, the cube particles should be at least 9-fold less active than that of spheres, which is not the case probably due to MBE competitive

adsorption under reaction conditions or Br- leached to ethanol during reaction. This hypothesis is supported by the fact that Ostwald ripening of (100)-atom rich cubes occurs during the reaction indicating weakened stabilization. Even if Br^- influences the activity of (100) planes, the effect would be similar for these planes located on spheres and cubes. However, the Br^- effect cannot be underestimated and the reported TOFs of MBE hydrogenation should be used with precaution for any Br-free catalysts.

4.3.4 Calculation of apparent activation energy

The observed energy of activation for the formation of MBA has been determined from the Arrhenius plot as shown in Fig. 4.13, in which the logarithm of the reaction rates against the reciprocal of the temperature has been plotted. The reaction rates were used instead of rate constants as the rates were determined at the same 10% conversion, i.e., the same MBE and MBA concentrations. The apparent activation energies were determined as 17±3 kJ/mol for the spheres and 23±3 kJ/mol for the cubes. Detailed calculation is shown in Appendix F. The calculations were based on 9 experiments for the spheres and 11 for the cubes; the errors were calculated using "linest" function in Excel. The line fitting function "linest" calculates the statistics for a straight line using the "least squares" method. The experiments were performed in the temperature range of 303-317 K at constant hydrogen pressure. Similar activation energy result has been reported as 17 kJ/mol for an olefinic alcohol hydrogenation over Lindar catalyst containing spherical Pd nanoparticles poisoned with lead acetate.[41]

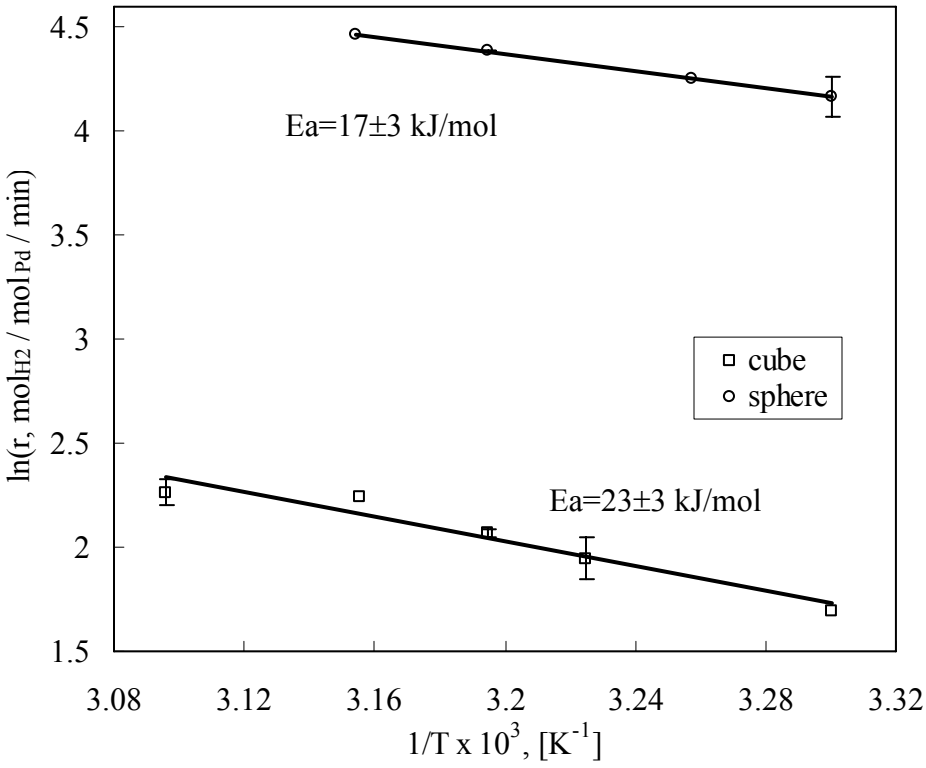

Figure 4.13. Arrhenius plots and activation energies of MBE hydrogenation with Pd spheres (0.0195±0.0005% Pd loading) and cubes (0.11 ±0.02% Pd loading) based on the rates at the same MBE concentration (10% conversion). Reaction conditions: 0.45 MPa absolute pressure, 1,200 rpm, 0.04 M MBE, 200 mL ethanol, MBE-to-Pd molar ratio of 8,300.

Higher apparent activation energy for the cubes correlates with their lower activity as compared to nanospheres. The adsorption equilibrium constants and/or heats of adsorption of both MBE and MBA on (100) surfaces of cubes are different from those of surface atoms of spheres. Variation of adsorption equilibrium constants and heats of adsorption with crystallographic orientation is a well-established phenomenon in heterogeneous catalysis.[117] Adsorption energies depend strongly on the local structure of the surface. It has also been observed that adsorption energies on polycrystalline surfaces (such as those of

spheres) are significantly higher than on the most stable planes (111) or (100) of single crystals, perhaps because of the stronger interaction of adsorbates, such as hydrogen, with surface defects.[117]

4.3.5 A hypothetical most active nanoparticle

As discussed in this study, (100) surface atoms are not the only active sites in MBE hydrogenation over Pd spherical nanoparticles. Previous studies also pointed out the activity of all terrace atoms or (111) surface atoms in unsaturated alcohol hydrogenations.[12-13, 19, 25] Thus, between (111) surface atoms and defect atoms, the former is assumed to be the second type active sites. Considering that the activity (100) atoms on the spherical particles is 2.64 s^{-1} (Table 4.6), the defect atoms are non-active, the activity of (111) atoms of a 3.0 nm spherical particle can be calculated using surface statistics (Fig. 4.12) and TOF per all terrace atoms (Table 4.6). The estimated activity of each (111) surface atom was 5.36 s^{-1}. Under these assumptions, tetrahedral Pd nanoparticles with only (111) atoms as terrace atoms should be the most active in MBE hydrogenation. Fig. 4.14 shows activity per total Pd atoms for hypothetical tetrahedral Pd nanoparticles, assuming that each terrace (111) atom has an activity of 5.36 s^{-1}. As seen, the nanoparticle with 10 atoms on the rib (~ 3 nm rib length) would possess the highest activity per overall Pd loading of 164 $mol_{H2}/(mol_{Pd} \cdot min)$ as opposed to 80 $mol_{H2}/(mol_{Pd} \cdot min)$ for a sphere of 3 nm diameter (Table 1). To verify the hypothesis, one would need to synthesize Pd tetrahedral particles stabilized by CTAB (as a stabilizer may influence the activity). However, as for now, the selective synthesis of such small Pd tetrahedrons in the presence of CTAB has not been achieved yet, and only larger anisotropic particles with mixed shapes were reported.[118-119] Further developments in nanotechnology are required to achieve desirable nanostructures with advanced catalytic properties.

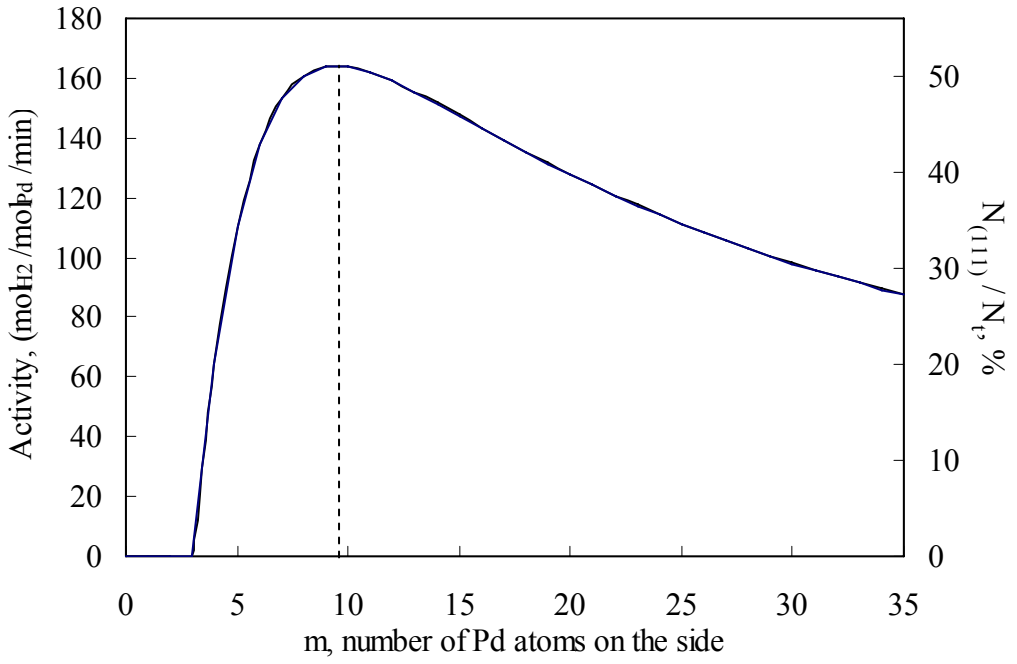

Figure. 4.14. Activity (per total Pd atoms) and corresponding percentage of (111) atoms for hypothetical tetrahedral Palladium nanoparticles with assumed activity of each terrace atom as 5.36 s^{-1}.

4.4 Results and discussions on MBY hydrogenation

The main objective in the hydrogenation of alkynes is to achieve the highest possible alkene selectivity. Bond and Wells[120] interpreted the selectivity of alkyne hydrogenation over transitional metals to depend on two factors: intrinsic reaction rate constants for the hydrogenations of alkyne and alkene (kinetic factor) and the thermodynamic factor, which is related to the relative strength of adsorption of alkyne and alkene.[11] Considering the overall reaction of MBY hydrogenation over the same metal Pd, the cube catalyst should show higher MBE selectivity due to its lower activity for alkene hydrogenation. So, the same catalysts (cube and sphere) were used for MBY hydrogenation to verify this hypothesis.

4.4.1 Typical catalytic behavior

The typical kinetic curves of the MBY semi-hydrogenation using cube-supported and sphere-supported catalysts carried out at constant hydrogen pressure are both shown in Fig. 4.15. For the both catalysts, the semi-hydrogenation of MBY to MBE (C≡C to C=C) is the main reaction. It can be seen from the MBE curve that the reaction proceeds through two separate stages. The desired product MBE concentration increases rapidly in the initial stage and reaches the maximum when almost all the MBY is consumed. Then in the second stage, MBE concentration starts to decrease because of the consumption from the consecutive hydrogenation of MBE to MBA as MBY has used up. However, the reaction rate of the second stage is much lower compare with the main reaction as can be seen from the slop of the concentration curve at the two stages. The intermediate MBE is formed selectively as long as MBY exists. Due to the known higher adsorption equilibrium constant of alkynes as compared to alkenes (by two orders of magnitude[19]), the catalyst surface is covered mostly with MBY. The strongly adsorbed MBY prevents readsorption of the produced MBE and, as a result, effectively stops further hydrogenation of olefinic alcohol to saturated alcohol. MBA appears at the very beginning of the reaction, confirming the presence of a parallel path of the direct MBY hydrogenation to MBA, which is typical for Pd catalysts in alkyne hydrogenations.[29] Sphere-containing catalyst with 0.027±0.001% Pd loading shows higher activity as compared to the cube-containing catalyst with 0.041±0.004% Pd loading as seen from Fig. 4.15.

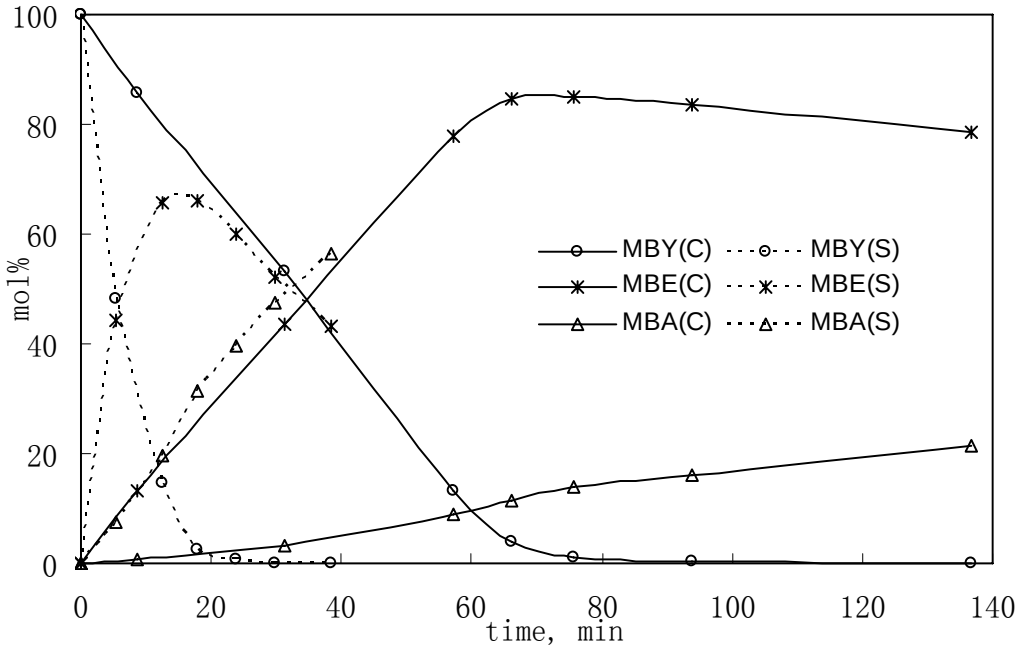

Figure 4.15. Product distributions in hydrogenation of MBY over cube-supported (C, 0.041±0.004% Pd loading) and sphere-supported (S, 0.027% Pd loading) catalysts as a function of reaction time. Symbols represent experimental data, lines are guides for eye. Experimental conditions: 313 K, 0.45 MPa pressure, 1,200 rpm, 0.041 M MBE, 200 mL ethanol, MBE-to-Pd molar ratio of 10,600.

4.4.2 Comparison of selectivity between spheres and cubes

Fig. 4.16 shows the product selectivity and yield as a function of conversion for reactions with sphere and cube supported catalyst under the same reaction conditions. Cube nanoparticles show higher selectivity than the spherical particles at all conversions. Moreover, the selectivity of spheres declines while the reaction proceeds, while it stays almost constant for cubes up to 95% conversion. The maximum yield of alkene is 85% at a conversion of 99% for cubes, versus 66% maximum yield at the MBY conversion of 97% for the spheres.

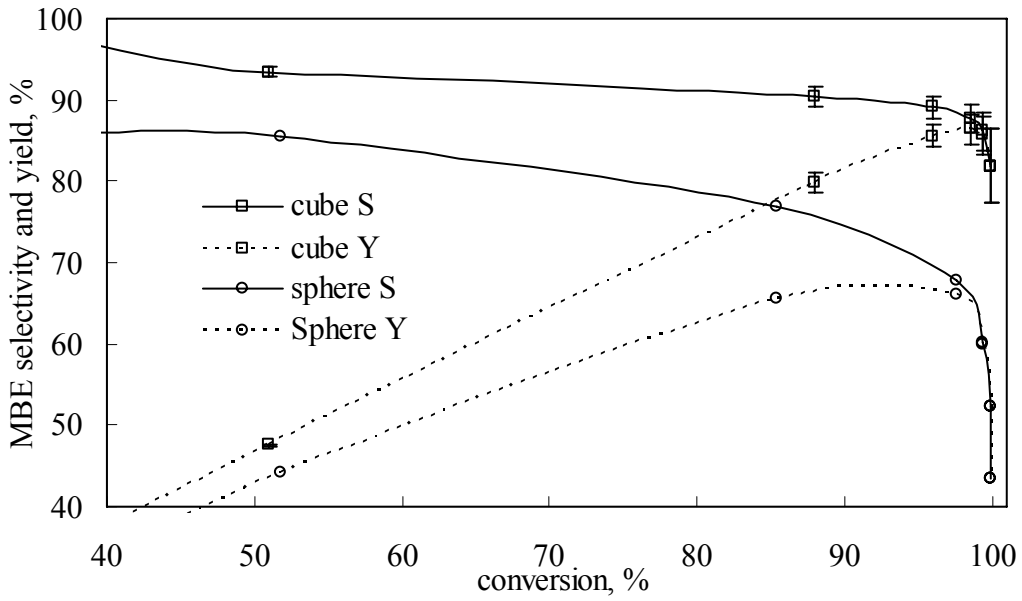

Figure 4.16. Typical product selectivity and yield as a function of conversion over sphere and cube supported catalyst. (S stands for selectivity; Y stands for yield.) Reaction conditions: refer Fig 4.15.

Reactions for sphere-supported and cube-supported catalyst were also carried out at different temperatures over a range of 303 K to 320 K. The selectivity vs. conversion plots are presented in Fig. 4.17. The corresponding initial reaction rate, MBE yield and selectivity at 20% and 95% conversions are shown in Table 4.7. The initial product selectivity (at 20% conversion) is around 94% for the cubes and 89% for the spheres. The product selectivity at 95% conversion for the reactions with nanocubes does not vary with temperature being 89%, while in the case of nanospheres it drops by 5% for a 13-degree temperature increase.

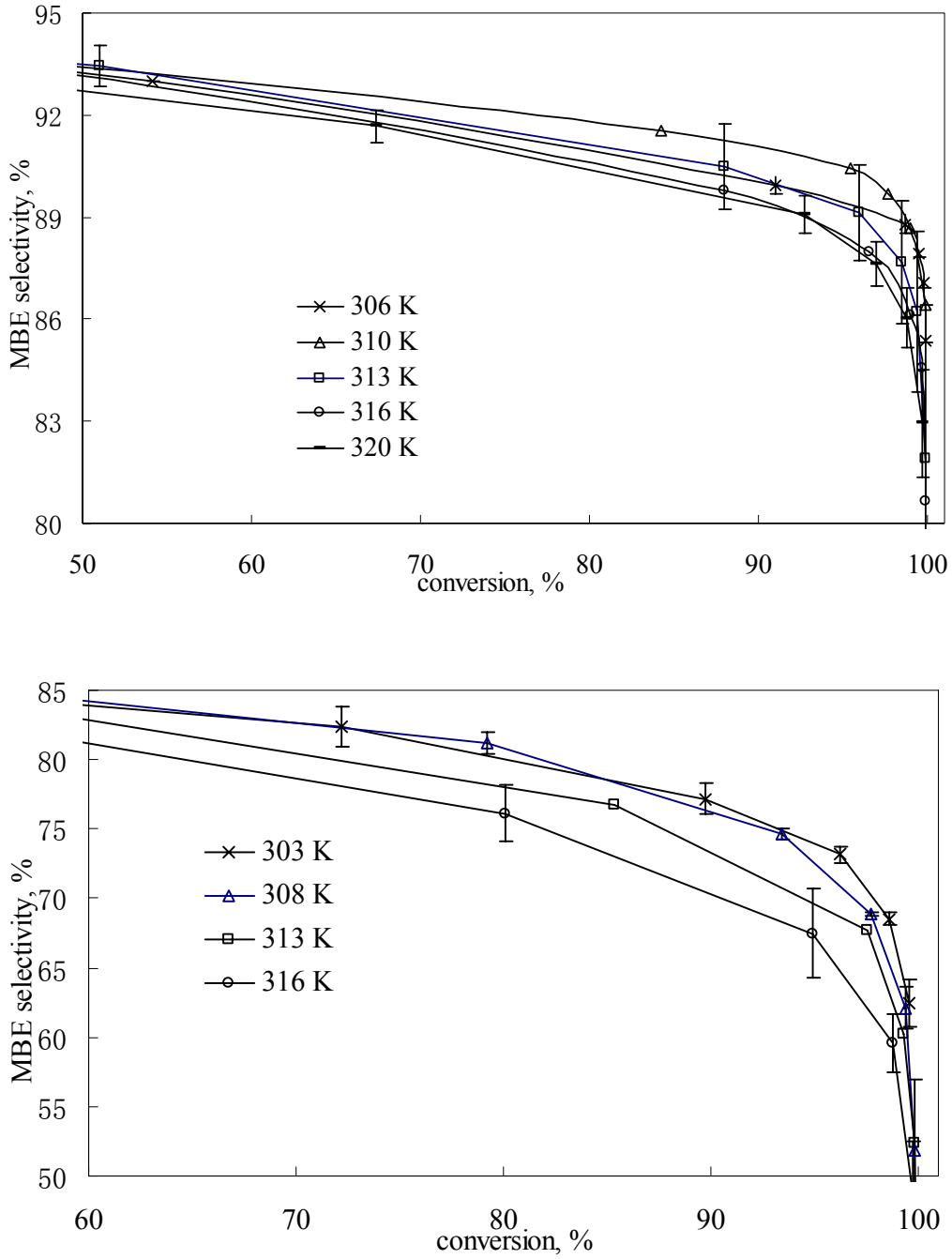

Figure 4.17. Catalyst selectivity varying with temperature: cube-supported catalyst (up), sphere-supported catalyst (down). For other than temperature reaction conditions see Fig. 4.15.

Table 4.7a. Initial reaction rate, product yield, and selectivity of sphere-supported catalysts at different temperatures.

	Sphere-supported catalyst			
Temperature, K	303	308	313	316
Initial reaction rate, mol/min/mol$_{Pd}$	692±18	853±36	998	1018±29
Max. product yield, %	69.7±1.7	69.8±0.2	66.1	64.1±3.1
Initial product select. at 20% conversion	88.2	90.0	89.0	89.5
Product selectivity at 95% conversion	73.3±1.6	72.5±0.23	69.6	67.4±3.1

Table 4.7b. Initial reaction rate, product yield, and selectivity of cube-supported catalysts at different temperatures.

	Cube-supported catalyst				
Temperature, K	306	310	313	316	320
Initial reaction rate, mol/min/mol$_{Pd}$	116±9	151	173±7	219	210±34
Max. product yield, %	87.5±0.3	87.8	86.4±1.3	85.3	84.3±0.1
Initial product select. at 20% conversion	94.7±0.6	94.2	94.6±0.8	94.3	94.3±0.1
Product Selectivity at 95% conversion	89.3±0.3	90.4	89.1±1.4	88.1	88.4±0.7

The metal dispersion of the synthesized sphere and cube are 37.4 % and 5.7 %, respectively. Some previous studies indicate that catalyst with lower dispersion ensure better selectivities for alkene formation,[19, 121-122] whereas in other cases no effect was observed.[19, 123-124] It is not easy to compare the results from other studies directly since different substrates were used under different reaction conditions.

Thus, the cube-containing catalyst allows higher selectivity to MBE at all

conversions and higher MBE yield as compared to the sphere-containing catalyst under all studied reaction conditions. The question remains whether this phenomena is due to the higher intrinsic selectivity of (100) planes of cubes as compared to mixed surfaces of the spheres, or the observed structure sensitivity is apparent. Mass transfer effects are known to lead to decreased selectivity in MBY hydrogenation,[29] thus, they were addressed as discussed below.

4.4.3 Mass transfer limitations

The gas-liquid mass transfer was found not be affected by the stirring speed above 250 rpm (section 4.3.1). The internal liquid-solid mass transfer can be considered negligible to the egg-shell catalyst structures. Thus, only external liquid-solid mass transfer effects for dissolved hydrogen and MBY should be evaluated.

Carberry number is calculated to estimate the influence of external liquid-solid mass transfer on the MBY catalytic hydrogenation. In current study, hydrogen was present at steady low concentration. As the reaction proceeds towards the end of the reaction, alkyne substrate can become a limiting reactant. The mass transfer limitations of hydrogen and MBY were both estimated at the initial reaction conditions (20% conversion) and the reaction peak. The calculations were based on the reactions at 313K, 0.45 MPa and 1200 rpm stirring speed. The initial hydrogen consumption was assumed to be all contributed to the MBY converted to MBE, since the selectivity of MBA close to 10% for 20% conversion of MBY.

The Carberry numbers are presented in Table 4.8. Carberry number less than 0.05 indicate that liquid-solid mass transport limitations can be neglected. The errors for Ca are based only on the 30% standard deviation in Sherwood number. For reactions using cube catalyst, hydrogen diffusion will not affect the reaction

kinetics. The Carberry number of MBY may get slightly larger than 0.05 considering the errors, indicates there may be mass transfer limitation of MBY. Especially as the reaction proceeds to the peak, the low concentration of MBY may become a problem and limit the overall reaction rate. For reactions with sphere catalyst, the Carberry numbers of both hydrogen and MBY are greater than 0.05 indicating the reaction is limited by liquid to solid mass transfer. The Carberry number of MBY at reaction peak is much larger than others.

It should be pointed out that the estimation of mass transfer limitation with the Carberry number is not accurate. The mass transfer coefficients estimated by an empirical correlation have a standard deviation of 30%. There is also an uncertainty in the calculated specific surface area, because the exact geometry of the particle is not known and the particles were assumed as nonporous where as the BET result showed an average pore size of 2-20 nm.

Table 4.8. Results of calculation of Carberry numbers for initial reaction rates. Experimental conditions: 313 K, 0.45 MPa pressure, 1,200 rpm, 0.041 M MBE, 200 mL ethanol, MBE-to-Pd molar ratio of 10,600.

	cube	sphere
$-R_{H2}$, mol/(gcat·s)	1.11×10^{-5}	4.22×10^{-5}
$-R_{Y}$, mol/(gcat·s)	1.11×10^{-5}	4.22×10^{-5}
$C_{H2,b}$, mol/m^3	16.4	16.4
$C_{Y,b}$, mol/m^3	32.8	32.8
Ca_{H2}	0.037±0.013	0.142±0.048
Ca_{Y}	0.046±0.015	0.175±0.059

In conclusion, the cube-containing nanocatalyst exhibits its intrinsic initial

activity and initial selectivity in MBY hydrogenation under current conditions, while the activity and selectivity of the spherical particles is influenced by liquid-solid mass transfer of both hydrogen and MBY.

4.4.4 Intrinsic and apparent TOFs

The intrinsic initial TOF of MBY hydrogenation can be determined for the cube-containing catalyst. Since the supported catalyst was employed in the MBY hydrogenation, one plane of the cube was assumed to be blocked by attaching to the catalyst support. The leached particles were considered as unsupported, which means all the active sites are available. From the AAS result, 3.3±0.03% of Pd leached during the reaction. The initial TOFs per total surface atoms were calculated as 60.2±3.4s^{-1} for the cubes of 20 nm for reactions at 313 K. The value is 23 times higher than the TOF of the cubes in the MBE hydrogenation under the same conditions, which proves that the cubes with 98% of all surface atoms belonging to (100) planes, are intrinsically more selective towards MBY hydrogenation to MBE vs. MBE hydrogenation to MBA.

A similar calculation for the sphere-containing catalyst results in the value of 50.1 s^{-1}, taking into consideration 12% Pd leaching from the support. However, this value is an apparent TOF, affected by the mass transfer limitations. If enough hydrogen and MBY are supplied to the catalyst surface per unit time to support the kinetic regime, this value can be both higher or lower depending on the mechanism of the catalytic reaction and adsorption constants (as MBY and hydrogen concentration appear both in the nominator and denominator of a possible rate equation (Eqn.13).

4.4.5 Apparent activation energies

The observed apparent activation energies for the formation of alkene were determined from the Arrhenius plot shown in Fig. 4.18 by plotting the logarithm of the initial reaction rate against the reciprocal of the temperature. The apparent activation energies were determined as 24±3 kJ/mol for the spheres and 38±6 kJ/mol for the cubes. The detailed calculation is shown in Appendix G. The experiments were performed in a temperature range of 303 K to 320 K at a constant hydrogen pressure of 0.45 MPa. The data were obtained based on 9 experiments for the cubes and 10 for the spheres; the errors were calculated using "linest" function in Excel. The values are based on the reaction rates at the same MBE concentration (20% conversion).

The apparent activation energy for the cubes can be referred as the apparent activation energy for the kinetic regime. The energy (38±6 kJ/mol) is much higher than that of MBE hydrogenation (23±6 kJ/mol), indicating that higher temperature should result in improved selectivities. Note that the trend can not be observed in Fig. 4.17 (selectivity vs. conversion at temperatures 306-320 K) because the reaction becomes mass transfer limited at high conversions (refer to Ca in Table 4.8), and the mass transfer effect becomes more pronounced at higher temperatures, as the external mass transfer activation energy is in the range of 5 – 15 kJ/mol.[47]

The activation energy for the spheres (24±3 kJ/mol) is lower than that for the cubes, which reflects the presence of external mass transfer limitations. The mass transfer effect can also be claimed responsible for selectivity decrease with temperature increase for the reactions with spheres as shown in Fig. 4.17. If the reaction is limited by MBY mass transfer, its concentration at the catalyst surface becomes lower as compared to the kinetic regime, so more sites will be occupied by MBE as compared to MBY-occupied sites for the kinetic regime, resulting in

lower selectivity. The effect is more pronounced at higher temperatures due to higher intrinsic activation energy as compared to the mass transfer activation energy.

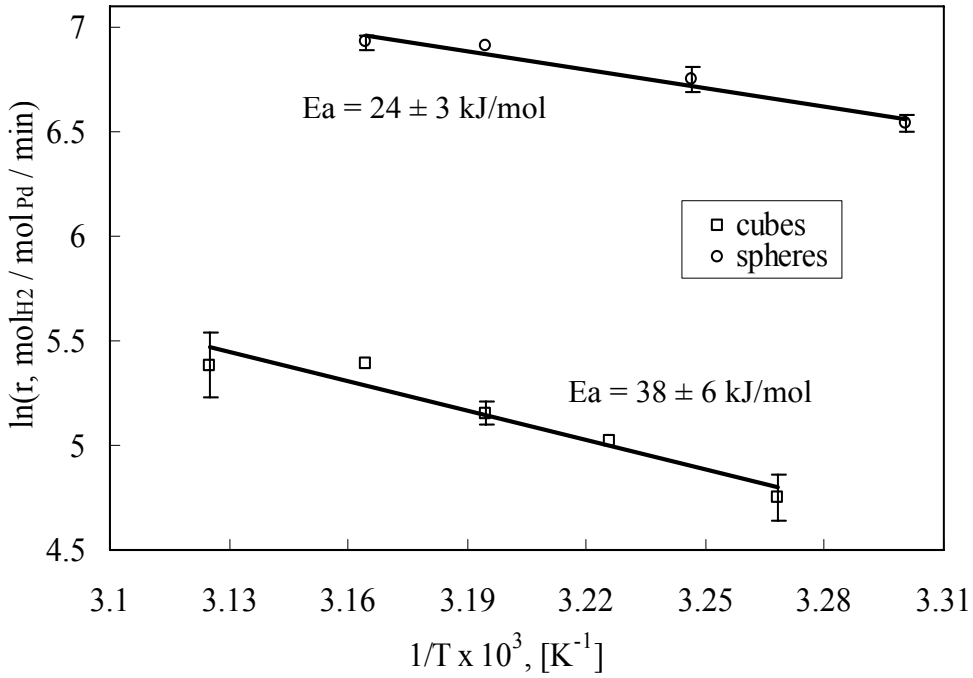

Figure 4.18. Arrhenius plots and activation energies of MBY hydrogenation with Pd spheres (0.027±0.001% Pd loading)and cubes (0.041±0.004% Pd loading) based on the rates at the same MBY concentration (20% conversion). For other than temperature reaction conditions see Fig. 4.15.

Thus, the observed structure sensitivity of MBY hydrogenation over spherical and cubic nanoparticles is apparent, and the comparison of intrinsic activities and selectivities cannot be made for these reaction conditions. The study shows the importance of liquid-solid mass transfer effect evaluation in studying structure sensitivity of catalytic reactions.

Chapter 5. Conclusions

Monodisperse Pd nanocubes of 20 nm rib length and Pd nanospheres of 3.0 nm diameter were synthesized in the presence of CTAB and used in both 2-methyl-3-buten-2-ol and 2-methyl-3-butyn-2-ol hydrogenations to study their structure sensitivity.

The following conclusions can be drawn from the olefinic alcohol hydrogenation:

- The studied alkene hydrogenation reaction was proved to proceed in the kinetic regime under studied reaction conditions; thus, intrinsic turnover frequencies could be determined.
- Turnover frequencies calculated per all surface atoms are 2.58 s^{-1} for the cubes and 3.86 s^{-1} for the spheres at 313 K. This indicates that (100) atoms of cubes comprising ~98% of all surface atoms have lower activity than other surface atoms of the spheres, composed of atoms on (111), (100) terraces and edges and vertices. The MBE hydrogenation reaction is, thus, structure sensitive.
- Apparent activation energies are 23±3 kJ/mol for the cubes and 17±3 kJ/mol for the spheres, indicating likely different equilibrium adsorption constants and heats of adsorption of MBE on the surfaces of cubes and spheres.
- Assuming that only (100) atoms are active sites of the cubes, and both (111) and (100) atoms are active sites of the spheres, TOFs for (100) atoms and (111) atoms are 2.63 and 5.36 s^{-1}, respectively. A hypothetical most active nanoparticle would be a tetrahedron whose terrace atoms are only (111) atoms; its activity is predicted

to be twice higher per total Pd loading as compared to a spherical particle of the same size.

The following conclusions are drawn from the acetylenic alcohol hydrogenation:

- Cube catalyst showed higher selectivity to the olefinic alcohol as compared to the spheres at all conversions; the maximum MBE yield at 313 K is 85% for the cubes vs. 66% for the spheres.
- Evaluation of the external liquid-solid mass transfer limitations showed that the reaction catalyzed by cubes proceeds in the kinetic regime at low conversions, while the sphere-catalyzed reaction is mass transfer limited at all conversions, indicating that the observed structure sensitivity is apparent.
- Apparent activation energies are 38±6 kJ/mol for the cubes under kinetic regime and 24±3 kJ/mol for the spheres under mass transfer limited regime.
- The study reveals the reason of the observed structure sensitivity of MBY hydrogenation in the presence of cubic and spherical nanoparticles, which is the effect of mass transfer limitations.

Overall, the study shows the applicability and limitations of the use of nanoparticles for structure sensitivity studies in catalysis.

Chapter 6. Outlook

Nanostructures of various shapes and sizes have become a powerful tool in revealing the reaction active sites since the surface crystal facets and the number of atoms located at the edges or corners can be determined from nanoparticles' shape and size. Structure-sensitive catalytic reactions, such as carbon-carbon multiple bond hydrogenations, turn out to be strongly depend on nanoparticle shape. Although there are large numbers of work on the application of palladium nanoparticles in catalysis, few reports deal with their active sites. Future work in this area could allow design of even more efficient nanocatalysts. In the future, it is still important to develop and improve methods to synthesize nanoparticles with defined size and shape in order to study reaction structure sensitivity, especially tetrahedrons enclosed by four (111) facets as they are supposed to be the most active particles.

Endnotes:

1. A version of section 4.3 has been published: Ma, R. and Semagina, N., Journal of Physical Chemistry C, 2010. 114(36): p. 15417-15423.

References:

1. Kung, H.H. and Kung, C.M., eds. *Nanotechnology and heterogeneous catalysis*. Nanotechnology in Catalysis ed. B. Zhou, et al. Vol. 3. 2007, Springer - Verlag.
2. Wachs, I.E. and Fitzpatrick, L.E., *Characterization of catalytic materials*. Materials characterization series. 1992, Boston, Greenwich, Conn.: Butterworth-Heinemann; Manning. 202 p.

3. Cushing, B.L., Kolesnichenko, V.L., and O'Connor, C.J., *Recent advances in the liquid-phase syntheses of inorganic nanoparticles.* Chemical Reviews, 2004. **104**(9): p. 3893-3946.
4. Narayanan, R. and El-Sayed, M.A., *Catalysis with transition metal nanoparticles in colloidal solution: Nanoparticle shape dependence and stability.* Journal of Physical Chemistry B, 2005. **109**(26): p. 12663-12676.
5. Semagina, N. and Kiwi-Minsker, L., *Recent advances in the liquid-phase synthesis of metal nanostructures with controlled shape and size for catalysis.* Catalysis Reviews-Science and Engineering, 2009. **51**(2): p. 147-217.
6. Ma, R. and Semagina, N., *Nanoparticle shape effect study as an efficient tool to reveal the structure sensitivity of olefinic alcohol hydrogenation.* Journal of Physical Chemistry C, 2010. **114**(36): p. 15417-15423.
7. Vanharde.R and Hartog, F., *Statistics of surface atoms and surface sites on metal crystals.* Surface Science, 1969. **15**(2): p. 189.
8. Xia, Y., et al., *Shape-controlled synthesis of metal nanocrystals: simple chemistry meets complex physics?* Angewandte Chemie-International Edition, 2009. **48**(1): p. 60-103.
9. Narayanan, R. and El-Sayed, M.A., *Effect of colloidal nanocatalysis on the metallic nanoparticle shape: The Suzuki reaction.* Langmuir, 2005. **21**(5): p. 2027-2033.
10. Tsung, C.K., et al., *Sub-10 nm platinum nanocrystals with size and shape control: catalytic study for ethylene and pyrrole hydrogenation.* Journal of the American Chemical Society, 2009. **131**(16): p. 5816-5822.
11. Nishimura, S., *Handbook of heterogeneous catalytic hydrogenation for organic synthesis*. 2001, New York: J. Wiley. P. 29, P64, P148.
12. Wilson, O.M., et al., *Effect of Pd nanoparticle size on the catalytic hydrogenation of allyl alcohol.* Journal of the American Chemical Society, 2006. **128**(14): p. 4510-4511.
13. Bhattacharjee, S., Dotzauer, D.M., and Bruening, M.L., *Selectivity as a function of nanoparticle size in the catalytic hydrogenation of unsaturated alcohols.* Journal of the American Chemical Society, 2009. **131**(10): p. 3601-3610.
14. Narayanan, R. and El-Sayed, M.A., *Effect of colloidal catalysis on the nanoparticle size distribution: Dendrimer-Pd vs PVP-Pd nanoparticles catalyzing the Suzuki coupling reaction.* Journal of Physical Chemistry B, 2004. **108**(25): p. 8572-8580.
15. Telkar, M.M., et al., *Shape-controlled preparation and catalytic activity of metal nanoparticles for hydrogenation of 2-butyne-1,4-diol and styrene oxide.* Applied Catalysis a-General, 2004. **273**(1-2): p. 11-19.
16. Lee, H., et al., *Morphological control of catalytically active platinum nanocrystals.* Angewandte Chemie-International Edition, 2006. **45**(46): p. 7824-7828.
17. Vannice, M.A., *Kinetics of catalytic reactions*. 2005, New York: Springer. xii, 240 p.
18. Palina, N., *Novel magnetic nanoparticles: Size and surfactant effects on geometric and electronic structure, probed using X-ray Absorption Spectroscopy*, in *Physikalisches Institut*. 2005, Bonn University: Germany. p. 119.
19. Molnár, Á., Sárkány, A., and Varga, M., *Hydrogenation of carbon-carbon multiple bonds:*

chemo-, regio- and stereo-selectivity. Journal of Molecular Catalysis A: Chemical, 2001. **173**(1-2): p. 185-221.

20. Davis, S.M., Zaera, F., and Somorjai, G.A., *Surface-structure and temperature-dependence of N-hexane skeletal rearrangement reactions catalyzed over platinum single-crystal surfaces - marked structure sensitivity of aromatization.* Journal of Catalysis, 1984. **85**(1): p. 206-223.
21. Shaikhutdinov, S.K., et al., *Particle size effects in adsorption and reaction of ethene and hydrogen on palladium model catalysts.* Abstracts of Papers of the American Chemical Society, 2001. **221**: p. U359-U359.
22. Moss, R.L., et al., *Structure and activity of supported metal-catalysts: 8. chemisorption and benzene hydrogenation on palladium-silica catalysts.* Journal of Catalysis, 1979. **58**(2): p. 206-219.
23. Ceyer, S.T., *The unique chemistry of hydrogen beneath the surface: Catalytic hydrogenation of hydrocarbons.* Accounts of Chemical Research, 2001. **34**(9): p. 737-744.
24. Ortiz-Soto, L., Monnier, J., and Amiridis, M., *Structure-sensitivity of propylene hydrogenation over cluster-derived bimetallic Pt-Au catalysts.* Catalysis Letters, 2006. **107**(1-2): p. 13-17.
25. Semagina, N., et al., *Synthesis of monodispersed palladium nanoparticles to study structure sensitivity of solvent-free selective hydrogenation of 2-methyl-3-butyn-2-ol.* Journal of Catalysis, 2007. **246**(2): p. 308-314.
26. Astruc, D., *Heterogeneous catalysis*, in *Organometallic Chemistry and Catalysis*. 2007, Springer Berlin Heidelberg. p. 457-486.
27. Chorkendorff, I. and Niemantsverdriet, J.W., *Concepts of modern catalysis and kinetics*. 2 ed. 2007, Weinheim Germany: Wiley-VCH. xvii, 452 p.
28. Le Page, J.F., Cosyns, J., and Courty, P., et al., *Applied heterogeneous catalysis: design, manufacture, use of solid catalysts*. 1987, Paris: Editions Technip. 9.
29. Bruehwiler, A., et al., *Three-phase catalytic hydrogenation of a functionalized alkyne: Mass transfer and kinetic studies with in situ hydrogen monitoring.* Industrial & Engineering Chemistry Research, 2008. **47**(18): p. 6862-6869.
30. Che, M. and Bennett, C.O., *The Influence of particle-size on the catalytic properties of supported metals.* Advances in Catalysis, 1989. **36**: p. 55-172.
31. Semagina, N., et al., *Structured catalyst of Pd/ZnO on sintered metal fibers for 2-methyl-3-butyn-2-ol selective hydrogenation (vol 251, pg 213, 2007).* Journal of Catalysis, 2008. **255**(1): p. 138-138.
32. McNaught, A.D., Wilkinson, A., and International Union of Pure and Applied Chemistry., *Compendium of chemical terminology : IUPAC recommendations*. 2nd ed. 1997, Oxford England ; Malden, MA, USA: Blackwell Science. vii, 450 p.
33. Besson, M. and Gallezot, P., *Deactivation of metal catalysts in liquid phase organic reactions.* Catalysis Today, 2003. **81**(4): p. 547-559.
34. Ratke, L. and Voorhees, P.W., *Growth and coarsening : Ostwald ripening in material*

processing. Engineering materials. 2002, Berlin ; New York: Springer. xi, 295 p.

35. Narayanan, R. and El-Sayed, M.A., *Effect of catalysis on the stability of metallic nanoparticles: Suzuki reaction catalyzed by PVP-palladium nanoparticles.* Journal of the American Chemical Society, 2003. **125**(27): p. 8340-8347.
36. Thathagar, M.B., et al., *Palladium nanoclusters in Sonogashira cross-coupling: A true catalytic species?* Advanced Synthesis & Catalysis, 2005. **347**(15): p. 1965-1968.
37. Thathagar, M.B., ten Elshof, J.E., and Rothenberg, G., *Pd nanoclusters in C-C coupling reactions: Proof of leaching.* Angewandte Chemie-International Edition, 2006. **45**(18): p. 2886-2890.
38. Astruc, D., *Palladium nanoparticles as efficient green homogeneous and heterogeneous carbon-carbon coupling precatalysts: A unifying view.* Inorganic Chemistry, 2007. **46**(6): p. 1884-1894.
39. Phan, N.T.S., Van Der Sluys, M., and Jones, C.W., *On the nature of the active species in palladium catalyzed Mizoroki-Heck and Suzuki-Miyaura couplings - Homogeneous or heterogeneous catalysis, a critical review.* Advanced Synthesis & Catalysis, 2006. **348**(6): p. 609-679.
40. Zhao, F.Y., et al., *Recyclable homogeneous/heterogeneous catalytic systems for Heck reaction through reversible transfer of palladium species between solvent and support.* Journal of Catalysis, 2000. **194**(2): p. 479-483.
41. Bruehwiler, A., *Selective hydrogenation of an alkyne with lindlar catalysts: mass transfer, kinetic study, and catalyst characterization*, in *Ecole Polytechnique Federale de Lausanne, Lausanne, Switzerland*. 2007.
42. Aramendia, M.A., et al., *Optimization of the selective semihydrogenation of phenylacetylene with supported palladium systems.* Applied Catalysis, 1990. **63**(2): p. 375-389.
43. Yu, Z.K., Liao, S.J., and Xu, Y., *Facile hydrodebromination of organic bromides with dihydrogen and polymer-anchored palladium catalyst under mild conditions.* Reactive & Functional Polymers, 1996. **29**(3): p. 151-157.
44. Singh, U.K. and Vannice, M.A., *Kinetics of liquid-phase hydrogenation reactions over supported metal catalysts - a review.* Applied Catalysis a-General, 2001. **213**(1): p. 1-24.
45. Joó, F., *Hydrogenation*, in *Aqueous Organometallic Catalysis*. 2002, Springer Netherlands. p. 47-148.
46. Linke, W.F. and Seidell, A., *Solubilities of inorganic and metal-organic compounds.* American Chemical Society, 1958. **1**: p. 1075.
47. Satterfield, C.N., *Mass transfer in heterogeneous catalysis*. 1981, Huntington, N.Y.: R. E. Krieger Pub. Co. xvi, 267 p.
48. Moulijn, J.A., Leeuwen, P.W.N.M.v., and Santen, R.A.v., *Catalysis : an integrated approach to homogeneous, heterogeneous and industrial catalysis*. Studies in surface science and catalysis 79. 1993, Amsterdam ; New York: Elsevier. xviii, 460 p.
49. Hardacre, C., et al., *Comparison of mass transfer effects in the heterogeneously catalysed hydrogenation of phenyl acetylene in heptane and an ionic liquid.* Chemical Engineering

Science, 2006. **61**(21): p. 6995-7006.

50. Struijk, J., et al., *Partial liquid-phase hydrogenation of benzene to cyclohexene over ruthenium catalysts in the presence of an aqueous salt solution: 1. preparation, characterization of the catalyst and study of a number of process variables.* Applied Catalysis a-General, 1992. **83**(2): p. 263-295.
51. Moulijn, J.A., Tarfaoui, A., and Kapteijn, F., *General aspects of catalyst testing.* Catal. Today, 1991. **11**: p. 1-12.
52. Fahlman, B.D., *Materials Chemistry*. Vol. 1. 2007, Mount Pleasant: Springer. p. 282 – 283.
53. Kogel, J.E. and Society for Mining Metallurgy and Exploration (U.S.), *Industrial minerals & rocks : commodities, markets, and uses*. 7th ed. 2006, Littleton, Colo.: Society for Mining, Metallurgy, and Exploration. xvi, 1548 p.
54. Leslie-Pelecky, D.L. and Rieke, R.D., *Magnetic properties of nanostructured materials.* Chemistry of Materials, 1996. **8**(8): p. 1770-1783.
55. Ying, J.Y. and Sun, T., *Research needs assessment on nanostructured catalysts.* Journal of Electroceramics, 1997. **1**(3): p. 219-238.
56. Koch, C.C., *Materials synthesis by mechanical alloying.* Annual Review of Materials Science, 1989. **19**: p. 121-143.
57. Astruc, D., *Nanoparticles and catalysis*. 2007, Weinheim: Wiley-VCH. P.60.
58. Henglein, A., *Colloidal palladium nanoparticles: Reduction of Pd(II) by H-2; PdcoreAushellAgshell particles.* Journal of Physical Chemistry B, 2000. **104**(29): p. 6683-6685.
59. Turkevic.J and Kim, G., *Palladium - preparation and catalytic properties of particles of uniform size.* Science, 1970. **169**(3948): p. 873-&.
60. J. Turkevich, *Colloidal gold. Part 1: historical and preparative aspects, morphology and structure.* Gold Bull, 1985(18): p. 86.
61. Lamer, V.K. and Dinegar, R.H., *Theory, production and mechanism of formation of monodispersed hydrosols.* Journal of the American Chemical Society, 1950. **72**(11): p. 4847-4854.
62. Lamer, V.K., *Nucleation in phase transitions.* Industrial and Engineering Chemistry, 1952. **44**(6): p. 1270-1277.
63. Watzky, M.A. and Finke, R.G., *Transition metal nanocluster formation kinetic and mechanistic studies. A new mechanism when hydrogen is the reductant: Slow, continuous nucleation and fast autocatalytic surface growth.* Journal of the American Chemical Society, 1997. **119**(43): p. 10382-10400.
64. Besson, C., Finney, E.E., and Finke, R.G., *A mechanism for transition-metal nanoparticle self-assembly.* Journal of the American Chemical Society, 2005. **127**(22): p. 8179-8184.
65. Burda, C., et al., *Chemistry and properties of nanocrystals of different shapes.* Chemical Reviews, 2005. **105**(4): p. 1025-1102.
66. Corain, B., Schmid, G., and Toshima, N., *Metal nanoclusters in catalysis and materials science : the issue of size control*. 1st ed. 2008, Amsterdam ; Boston: Elsevier. xi, 458 p.

67. Pachon, L.D. and Rothenberg, G., *Transition-metal nanoparticles: synthesis, stability and the leaching issue.* Applied Organometallic Chemistry, 2008. **22**(6): p. 288-299.
68. Reetz, M.T., Winter, M., and Tesche, B., *Self-assembly of tetraalkylammonium salt-stabilized giant palladium clusters on surfaces.* Chemical Communications, 1997(2): p. 147-148.
69. Teranishi, T. and Miyake, M., *Size control of palladium nanoparticles and their crystal structures.* Chemistry of Materials, 1998. **10**(2): p. 594-600.
70. Puntes, V.F., Krishnan, K.M., and Alivisatos, A.P., *Colloidal nanocrystal shape and size control: The case of cobalt.* Science, 2001. **291**(5511): p. 2115-2117.
71. Berhault, G., et al., *Seed-mediated synthesis of Pd nanocrystals: Factors influencing a kinetic- or thermodynamic-controlled growth regime.* Journal of Physical Chemistry C, 2007. **111**(16): p. 5915-5925.
72. Jana, N.R., Gearheart, L., and Murphy, C.J., *Seeding growth for size control of 5-40 nm diameter gold nanoparticles.* Langmuir, 2001. **17**(22): p. 6782-6786.
73. Chang, G., Oyama, M., and Hirao, K., *Facile synthesis of monodisperse palladium nanocubes and the characteristics of self-assembly.* Acta Materialia, 2007. **55**(10): p. 3453-3456.
74. Murphy, C.J. and Jana, N.R., *Controlling the aspect ratio of inorganic nanorods and nanowires.* Advanced Materials, 2002. **14**(1): p. 80-82.
75. Nikoobakht, B. and El-Sayed, M.A., *Evidence for bilayer assembly of cationic surfactants on the surface of gold nanorods.* Langmuir, 2001. **17**(20): p. 6368-6374.
76. Xiong, Y.J. and Xia, Y.N., *Shape-controlled synthesis of metal nanostructures: The case of palladium.* Advanced Materials, 2007. **19**(20): p. 3385-3391.
77. Sau, T.K. and Murphy, C.J., *Room temperature, high-yield synthesis of multiple shapes of gold nanoparticles in aqueous solution.* Journal of the American Chemical Society, 2004. **126**(28): p. 8648-8649.
78. Smith, D.K. and Korgel, B.A., *The Importance of the CTAB surfactant on the colloidal seed-mediated synthesis of gold nanorods.* Langmuir, 2008. **24**(3): p. 644-649.
79. Nikoobakht, B. and El-Sayed, M.A., *Preparation and growth mechanism of gold nanorods (NRs) using seed-mediated growth method.* Chemistry of Materials, 2003. **15**(10): p. 1957-1962.
80. Eriksson, S., et al., *Preparation of catalysts from microemulsions and their applications in heterogeneous catalysis.* Applied Catalysis a-General, 2004. **265**(2): p. 207-219.
81. Capek, I., *Preparation of metal nanoparticles in water-in-oil (w/o) microemulsions.* Advances in Colloid and Interface Science, 2004. **110**(1-2): p. 49-74.
82. Lisiecki, I. and Pileni, M.P., *Synthesis of copper metallic clusters using reverse micelles as microreactors.* Journal of the American Chemical Society, 1993. **115**(10): p. 3887-3896.
83. Wang, C.C., Chen, D.H., and Huang, T.C., *Synthesis of palladium nanoparticles in water-in-oil microemulsions.* Colloids and Surfaces a-Physicochemical and Engineering Aspects, 2001. **189**(1-3): p. 145-154.

84. Boutonnet, M., Lögdberg, S., and Elm Svensson, E., *Recent developments in the application of nanoparticles prepared from w/o microemulsions in heterogeneous catalysis.* Current Opinion in Colloid & Interface Science, 2008. **13**(4): p. 270-286.
85. Esumi, K., *Dendrimers for nanoparticle synthesis and dispersion stabilization.* Colloid Chemistry Ii, 2003. **227**: p. 31-52.
86. Astruc, D., Lu, F., and Aranzaes, J.R., *Nanoparticles as recyclable catalysts: The frontier between homogeneous and heterogeneous catalysis.* Angewandte Chemie - International Edition, 2005. **44**(48): p. 7852-7872.
87. Diallo, A.K., et al., *"Homeopathic" catalytic activity and atom-leaching mechanism in Miyaura-Suzuki reactions under ambient conditions with precise dendrimer-stabilized Pd nanoparticles.* Angewandte Chemie-International Edition, 2007. **46**(45): p. 8644-8648.
88. Li, Y. and El-Sayed, M.A., *The effect of stabilizers on the catalytic activity and stability of Pd colloidal nanoparticles in the Suzuki reactions in aqueous solution.* Journal of Physical Chemistry B, 2001. **105**(37): p. 8938-8943.
89. Crooks, R.M., et al., *Dendrimer-encapsulated metal nanoparticles: Synthesis, characterization, and applications to catalysis.* Accounts of Chemical Research, 2001. **34**(3): p. 181-190.
90. Briant, C.E., et al., *Synthesis and X-ray structural characterization of the centered Icosahedral gold cluster compound [Au13(Pme2ph)10cl2](Pf6)3 - the realization of a theoretical prediction.* Journal of the Chemical Society-Chemical Communications, 1981(5): p. 201-202.
91. Vandervelden, J.W.A., et al., *Gold clusters containing bidentate phosphine-ligands - preparation and X-ray structure Iivestigation of [Au5(Dppmh)3(Dppm)](No3)2 and [Au13(Dppmh)6](No3)N.* Recueil Des Travaux Chimiques Des Pays-Bas-Journal of the Royal Netherlands Chemical Society, 1981. **100**(4): p. 148-152.
92. Wen, F., et al., *Preparation of Pt-13 clusters in the presence of trialkylaluminium.* Applied Organometallic Chemistry, 2005. **19**(7): p. 827-829.
93. Toshima, N., et al., *Various ligand-stabilized metal nanoclusters as homogeneous and heterogeneous catalysts in the liquid phase.* Applied Organometallic Chemistry, 2001. **15**(3): p. 178-196.
94. Sau, T.K. and Murphy, C.J., *Seeded high yield synthesis of short Au nanorods in aqueous solution.* Langmuir, 2004. **20**(15): p. 6414-6420.
95. Bisson, L., et al., *Formation of palladium nanostructures in a seed-mediated synthesis through an oriented-attachment-directed aggregation.* Chemistry of Materials, 2009. **21**(13): p. 2668-2678.
96. Fan, F.R., et al., *An effective strategy for room-temperature synthesis of single-crystalline palladium nanocubes and nanodendrites in aqueous solution.* Crystal Growth & Design, 2009. **9**(5): p. 2335-2340.
97. Xiong, Y.J., et al., *Synthesis and mechanistic study of palladium nanobars and nanorods.* Journal of the American Chemical Society, 2007. **129**(12): p. 3665-3675.
98. Xiong, Y.J., et al., *Understanding the role of oxidative etching in the polyol synthesis of*

Pd nanoparticles with uniform shape and size. Journal of the American Chemical Society, 2005. **127**(20): p. 7332-7333.

99. Gole, A. and Murphy, C.J., *Seed-mediated synthesis of gold nanorods: Role of the size and nature of the seed.* Chemistry of Materials, 2004. **16**(19): p. 3633-3640.
100. Boutonnet, M., Kizling, J., and Stenius, P., *The preparation of monodisperse colloidal metal particles from micro-emulsions.* Colloids and Surfaces, 1982. **5**(3): p. 209-225.
101. Niu, W.X., et al., *Seed-mediated growth of nearly monodisperse palladium nanocubes with controllable sizes.* Crystal Growth & Design, 2008. **8**(12): p. 4440-4444.
102. Liu, M.Z. and Guyot-Sionnest, P., *Mechanism of silver(I)-assisted growth of gold nanorods and bipyramids*. Journal of Physical Chemistry B, 2005. **109**(47): p. 22192-22200.
103. Baletto, F. and Ferrando, R., *Structural properties of nanoclusters: Energetic, thermodynamic, and kinetic effects.* Reviews of Modern Physics, 2005. **77**(1): p. 371-423.
104. Barreteau, C., Desjonqueres, M.C., and Spanjaard, D., *Theoretical study of the icosahedral to cuboctahedral structural transition in Rh and Pd clusters.* European Physical Journal D, 2000. **11**(3): p. 395-402.
105. Navaladian, S., et al., *A rapid synthesis of oriented palladium nanoparticles by UV irradiation.* Nanoscale Research Letters, 2009. **4**(2): p. 181-186.
106. Narayanan, R. and El-Sayed, M.A., *Catalysis with transition metal nanoparticles in colloidal solution: nanoparticle shape dependence and stability.* J. Phys. Chem. B, 2005. **109**(26): p. 12663-12676.
107. Patterson, A.L., *The Scherrer formula for x-ray particle size determination.* Physical Review, 1939. **56**(10): p. 978-982.
108. Crezee, E., et al., *Three-phase hydrogenation of D-glucose over a carbon supported ruthenium catalyst-mass transfer and kinetics.* Applied Catalysis a-General, 2003. **251**(1): p. 1-17.
109. Purwanto, et al., *Solubility of hydrogen, carbon monoxide, and 1-octene in various solvents and solvent mixtures.* Journal of Chemical and Engineering Data, 1996. **41**(6): p. 1414-1417.
110. Sano, Y., Yamaguchi, N., and Adachi, T., *Mass transfer coefficients for suspended particles in agitated vessels and bubble columns.* J. Chem. Eng. Japan, 1974(7): p. 255-261.
111. Bates, R.L., Fondy, P.L., and Corpstei.Rr, *An examination of some geometric parameters of impeller power.* Industrial & Engineering Chemistry Process Design and Development, 1963. **2**(4): p. 310-&.
112. Assael, M.J. and Polimatidou, S.K., *Measurements of the viscosity of alcohols in the temperature-range 290-340-K at pressures up to 30 Mpa.* International Journal of Thermophysics, 1994. **15**(1): p. 95-107.
113. Wilke, C.R. and Chang, P., *Correlation of diffusions coefficients in dilute solutions.* AIChE J. , 1955(1): p. 264-270.
114. Bakker, J.J.W., et al., *Enhancement of catalyst performance using pressure pulses on*

macroporous structured catalysts. Industrial & Engineering Chemistry Research, 2007. **46**(25): p. 8574-8583.

115. Narayanan, R. and El-Sayed, M.A., *Effect of colloidal nanocatalysis on the metallic nanoparticle shape: the Suzuki reaction.* Langmuir, 2005. **21**: p. 2027-2033.
116. Le Bars, J., et al., *A catalytic probe of the surface of colloidal palladium particles using Heck coupling reactions.* Langmuir, 1999. **15**(22): p. 7621-7625.
117. Zaera, F., *Probing catalytic reactions at surfaces.* Progress in Surface Science, 2001. **69**(1-3): p. 1-98.
118. Berhault, G., et al., *Preparation of nanostructured Pd particles using a seeding synthesis approach - Application to the selective hydrogenation of buta-1,3-diene.* Appl. Catal. A, 2007. **327**: p. 32-43.
119. Piccolo, L., et al., *Tuning the shape of nanoparticles to control their catalytic properties: selective hydrogenation of 1,3-butadiene on Pd/Al2O3.* Phys. Chem. Chem. Phys., 2008. **10**: p. 5504-5506.
120. Bond, G.C. and Wells, P.B., *The mechanism of the hydrogenation of unsaturated hydrocarbons on transition metal catalysts.* Advances in Catalysis, 1964. **15**: p. 91-226.
121. Kitamura, T., Sugeta, M., and Sakata, G., *Liquid phase selective hydrogenation reaction of methylacetylene and propadiene in propylene over moderately dispersed palladium catalysts*, in *Science and Technology in Catalysis 1998*, H. Hattori and K. Otsuka, Editors. 1999, Elsevier Science Publ B V: Amsterdam. p. 427-430.
122. Duca, D., Liotta, L.F., and Deganello, G., *Selective hydrogenation of phenylacetylene on pumice-supported palladium catalysts.* Journal of Catalysis, 1995. **154**(1): p. 69-79.
123. Duca, D., Liotta, L.F., and Deganello, G., *Liquid-phase hydrogenation of phenylacetylene on pumice supported palladium catalysts.* Catalysis Today, 1995. **24**(1-2): p. 15-21.
124. Tessier, D., Rakai, A., and BozonVerduraz, F., *Palladium-alumina catalysts: Precursor, support and dispersion effects in selective hydrogenation.* Bulletin De La Societe Chimique De France, 1996. **133**(6): p. 637-642.

Appendix

Appendix A: TEM results for reproduced nanoparticles

Spherical nanoparticles S1 were synthesized in the presence of CTAB by fast reduction with sodium borohydride. Figure A1 shows the TEM image of spherical nanoparticles ("seeds"). The diameters of the spheres are around 3.0 nm which is very similar to the previous result (3.0±0.4 nm, Fig. 4.1). Therefore, the spherical nanoparticles are highly reproducible.

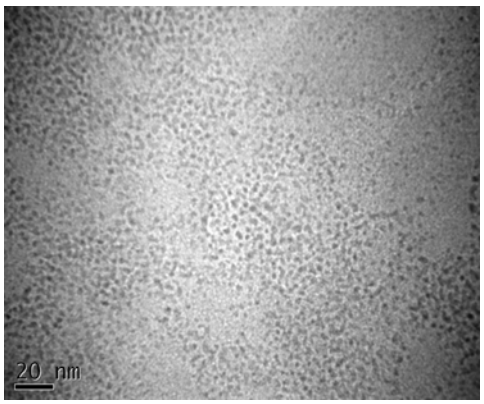

Figure A1. TEM image of sphere nanoparticles (S1).

Larger sphere nanoparticles were produced by step growth method. The nanoparticle synthesis from the first growth step (S2) was repeated. The sample contained larger particles ~7 nm but not spherical which is consistent with the previous TEM result. The consecutive growth steps for larger particles (S3-S5) were not repeated since the first step already failed to result spherical nanoparticles.

Nanoparticles were prepared a few more times following two similar microemulsion methods S6 and S7 (Fig. A2). Fig. A2a shows large agglomeration of nanoparticles and Fig. A2b shows both small particles (shapeless, ~10 nm) and big agglomerations. These TEM results for the repeated particles were consistent with their previous results (Fig 4.3).

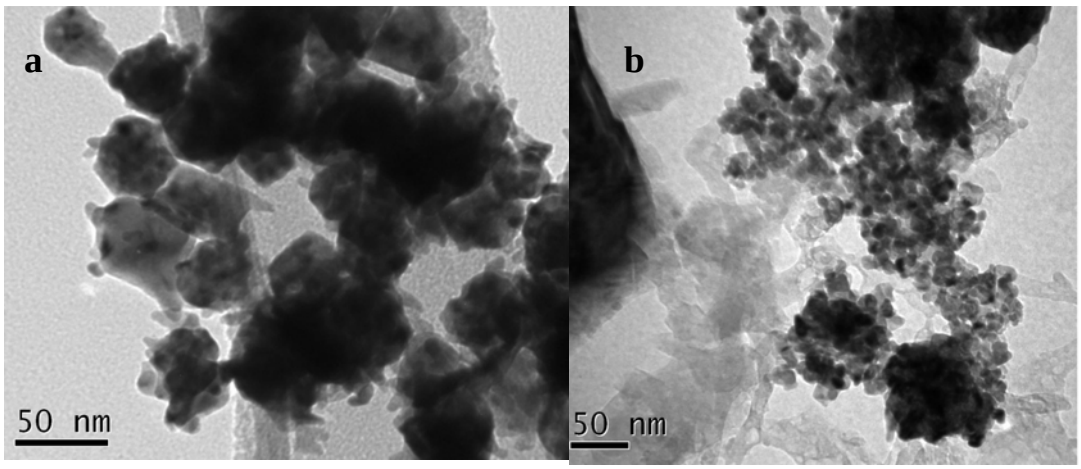

Figure A2. TEM images of Pd nanoparticles prepared from microemulsion methods: seed from S6 (a), seed from S7 (b).

Palladium nanocubes S11 (Fig. A3) were reproduced by reduction of H_2PdCl_4 with ascorbic acid in the presence of CTAB at 95 ^oC. The repeated synthesis also showed nearly monodispersed nanocubes with well-defined shapes. The size of these nanoparticles varies from 15 to 27 nm, but mostly around 21 nm. A few sphere-like and truncated cube particles were produced, while no agglomeration was observed. These results are consistent with previous TEM study; therefore, the direct synthesis of nanocubes by AA at 95 ^oC is highly reproducible.

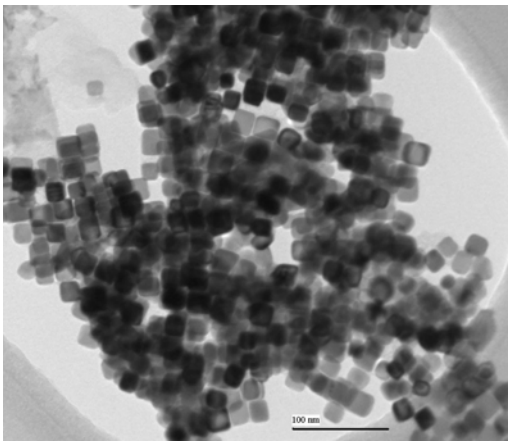

Figure A3. TEM image of Palladium cubes (S11) from direct synthesis.

Appendix B: Detailed XPS analysis result

Table B1. Quantification report on the surface composition of fresh catalyst: cube supported catalyst (0.041% Pd loading).

Peak	Position BE (eV)	FWHM (eV)	Raw Area (CPS)	RSF	Atomic Mass	Atomic Conc %	Mass Conc %
Na 1s	1070.44	2.70	43562.2	1.685	22.99	2.45	3.07
F 1s	686.84	5.76	13339.7	1.000	19.00	1.26	1.30
O 1s	530.39	3.54	423393.2	0.780	16.00	51.72	45.14
N 1s	400.89	1.47	2438.3	0.477	14.01	0.50	0.38
Pd 3d	335.09	3.44	51314.4	5.356	106.53	0.93	5.43
C 1s	284.69	3.25	66592.2	0.278	12.01	23.50	15.39
Cl 2p	205.59	0.40	440.8	0.891	35.46	0.05	0.09
B 1s	198.24	2.45	540.9	0.159	10.82	0.34	0.20
Br 3p	180.74	2.66	2828.0	1.279	79.91	0.22	0.96
Al 2s	118.44	3.30	81718.6	0.426	26.98	19.04	28.03

Table B2. Quantification report on the surface composition of fresh catalyst: sphere-supported catalyst (0.014% Pd loading).

Peak	Position BE (eV)	FWHM (eV)	Raw Area (CPS)	RSF	Atomic Mass	Atomic Conc %	Mass Conc %
Na 1s	1070.09	2.53	13896.7	1.685	22.99	0.88	1.12
F 1s	688.24	3.58	10956.2	1.000	19.00	1.16	1.22
O 1s	530.39	3.21	330270.5	0.780	16.00	45.42	40.28
N 1s	1486.71	0.00	0.0	0.000	14.01	0.00	0.00
Pd 3d	335.09	4.40	41967.0	5.356	106.53	0.86	5.08
C 1s	284.69	2.88	82237.7	0.278	12.01	32.67	21.75
Cl 2p	199.99	1.12	514.5	0.891	35.46	0.06	0.13
B 1s	197.19	1.77	816.7	0.159	10.82	0.57	0.34
Br 3p	181.79	3.22	10163.8	1.279	79.91	0.89	3.39
Al 2s	118.09	3.25	66591.0	0.426	26.98	17.47	26.13

Appendix C: BET report on pore size distribution of catalyst support

Analysis gas: Nitrogen Sample weight: 0.201g Adsorbate (DRP): Nitrogen Analysis time: 589.1 min

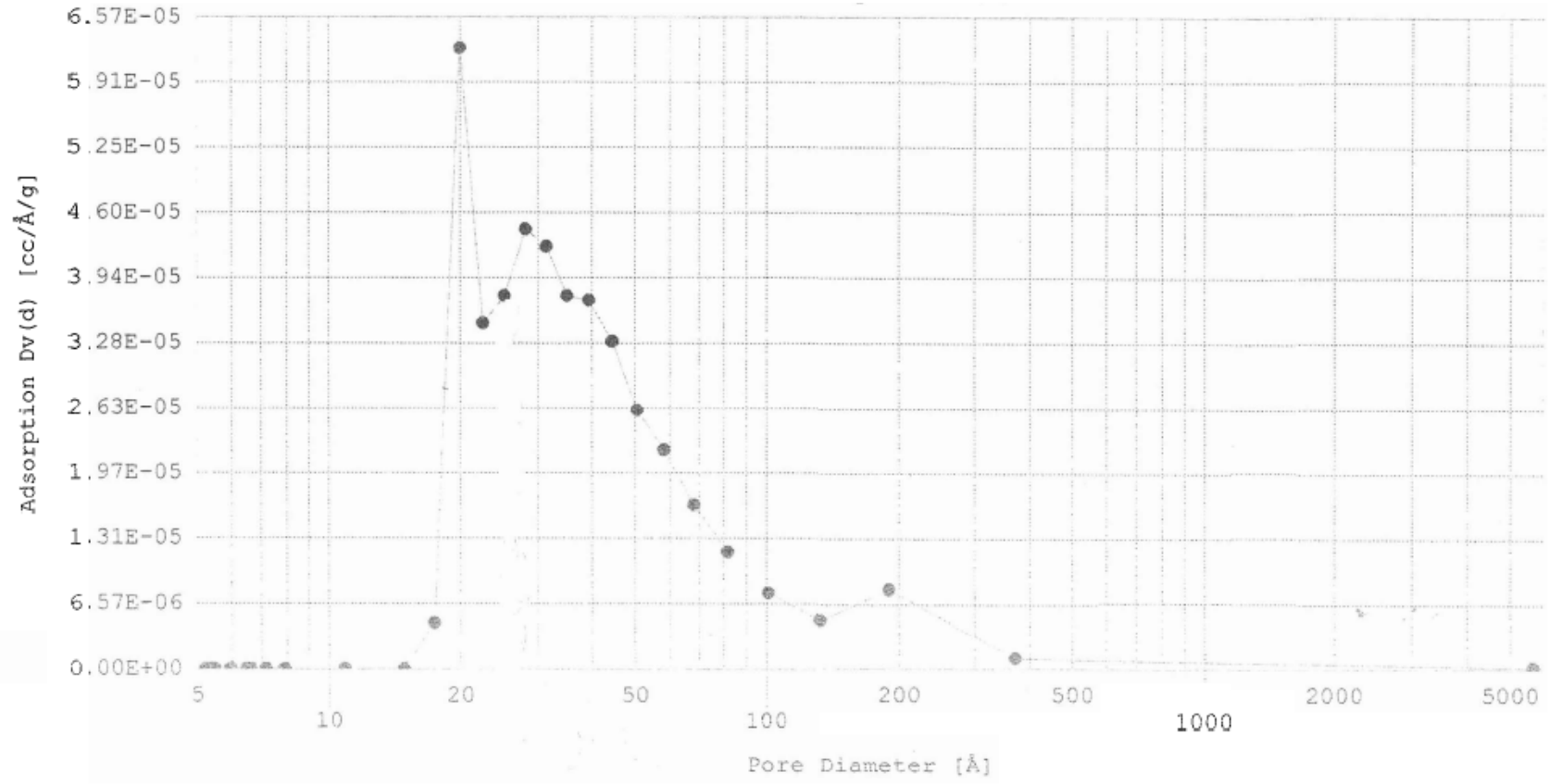

Appendix D: Crystal size calculations

Crystal size of cube nanoparticle is calculated using Scherrer equation (refer to section 4.2.4) based on information obtained from XRD result.

$$d = \frac{K\lambda}{\beta \cos(\theta)}$$

Table D1. Crystal size calculation for cube nanoparticle.

Peak	40.15	46.65	68.05
K	0.9	0.9	0.9
λ, nm	0.154	0.154	0.154
β	0.009106	0.00949	0.009745
θ	20.08	23.33	0.45
d, nm	**16.2**	**15.9**	**17.2**

By taking the average of the crystal size calculated at three different diffraction peaks, the average crystal size is around 16.4 nm for the cube nanoparticle.

Appendix E: TOF calculations

Surface statistics is based on the formula provided in Van Hardeveld and Hartog's paper.[E1]

TOF calculations for sphere

Surface atoms calculation of a f.c.c. cuboctahedron

m	N_T	N_S	$N(C_8^{4,5})$
2	38	32	0
3	201	122	6
4	***586***	272	24
5	***1289***	482	54
6	2406	752	96
7	4033	1082	150

For m>3

$N_t = 16m^3-33m^2+24m-6$

$N_s = 30m^2-60m+32$

$N_{(100)} = 6(m-2)^2$

$N_{(111)} = 8(3m^2-9m+7)$

$N_{terrace} = 6(m-2)^2+8(3m^2-9m+7)$

$N_{defect} = 12(m-2)+24(m-2)+24$

Pd atom diameter d_{at}= 0.274 nm

Sphere nanoparticle diameter d_{sph}= 3.08 nm (from TEM result)

d_{rel}= 11.24

$$d_{rel} = \frac{d_{sph}}{d_{at}}$$

Total atom, N_T= ***1052.7***

$$d_{rel} = 1.105 \times N_T^{1/3}$$

m= **5** from cubo-octahedron surface atom statistics

For a cuboctahedron with m=5

Nt	1289		
Ns	482		
$N_{(100)}$	54	$N_{(100)}/N_S$	0.112
Ns/Nt	**0.374**	$N_{(100)}/N_t$	0.042
$N_{(111)}$	296	$N_{terrace}/Ns$	0.726

$N_{terrace}$	350		N_{defect}/Ns	0.274
N_{defect}	132			
Ns	421	If one (111) plane is in contact with support.		
Ns/Nt	**0.327**			

Consider 42% of Pd leached out during the reaction

Ns/Nt	**0.347**	
Rate	80.4	mol H_2/(molPd·min) at 40°C
TOF	232.0	mol H_2/(mol$Pd_{surf\ atom}$·min)
TOF	**3.87**	mol H_2/(mol$Pd_{surf\ atm}$·s)
$TOF_{(100)}$	31.99	mol H_2/(mol$Pd_{(100)}$·s)
$TOF_{(111)}$	5.84	mol H_2/(mol$Pd_{(111)}$·s)
$TOF_{terrace}$	4.94	mol H_2/(mol$Pd_{terrace}$·s)
TOF_{defect}	13.09	mol H_2/(molPd_{defect}·s)

TOF calculations for cubes

Surface statistics for a cube with edge 20nm

width m	51.91	**52**	For m>3
Nt	546364		$N_t = 4m^3-6m^2+3m$
Ns	31214		$N_s = 12m^2-24m+14$
Ns/Nt	0.0571		$N_{(100)} = 6(m-1)^2+6(m-2)^2$
$N_{(100)}$	30606		$N_{terrace} = N_{(100)}$
N_{defect}	608		$N_{defect} = 12(m-2)+8$
$N_{(100)}/N_S$	0.981		
$N_{terrace}/Ns$	0.981		
N_{defect}/Ns	0.019		

Consider 34% of Pd leached out during the reaction, and one plane is in contact with support

leached Ns/Nt	0.019	Final Ns/Nt	**0.051**
Suppoted Ns/Nt	0.031	$N_{(100)}/N_t$	**0.050**
Rate	7.90	mol H_2/(molPd*min) at 40^oC	
TOF	155.37	mol H_2/(molPd$_{surf\ atom}$*min)	
TOF	**2.59**	mol H_2/(molPd$_{surf\ atm}$*s)	
TOF$_{(100)}$	**2.64**	mol H_2/(molPd$_{(100)}$*s)	
TOF$_{terrace}$	**2.64**	mol H_2/(molPd$_{terrace}$*s)	
TOF$_{defect}$	**132.94**	mol H_2/(molPd$_{defect}$*s)	

Reference:
E1. Van Hardeveld, R.; Hartog, F., The Statistics of Surface Atoms and Surface Sites on Metal Crystals. Surf. Sci. 1969, 15, 189-230

Appendix F: Apparent activation energy calculation for MBE reaction.

Arrhenius Law: $$k = A \cdot \exp(\frac{-E_a}{R \cdot T})$$

Rearrange as, $$\ln(k) = (-E_a) \cdot \frac{1}{R \cdot T} + \ln(A)$$

To compare the catalysts and reactions and different temperatures, we always used reaction rate at the same conversion (the same MBE and MBA concentrations), thus, the reaction rate can be used in the Arrhenius law to calculate apparent activation energies instead of the rate constants.

Table F1. Experimental results from cube-supported catalyst.

Exp	T, K	r, $mol_{MBE}/mol_{Pd}/min$	1/(T·R), mol/J	ln r
1	303	5.44	0.0003970	1.695
2	310	6.53	0.0003879	1.877
3	310	7.52	0.0003879	2.017
4	313	8.07	0.0003843	2.088
5	313	7.71	0.0003843	2.043
6	313	7.95	0.0003843	2.074
7	313	8.06	0.0003843	2.087
8	313	7.78	0.0003843	2.052
9	317	9.39	0.0003796	2.240
10	323	10.05	0.0003724	2.308
11	323	9.20	0.0003724	2.219

LINEST function in Excel was used to find the slope and its error as Ea = 22.9 ± 3 kJ/mol for MBE reaction with cube-supported catalyst.

Table F2. Experimental results from sphere-supported catalyst.

Exp	T, K	r, $mol_{MBE}/mol_{Pd}/min$	1/(T·R), mol/J	ln r
1	303	67.37	0.0003970	4.210
2	303	71.47	0.0003970	4.269
3	303	63.83	0.0003970	4.156
4	303	56.68	0.0003970	4.038
5	307	70.53	0.0003918	4.256
6	313	80.18	0.0003843	4.384
7	313	80.56	0.0003843	4.389
8	313	80.67	0.0003843	4.390
9	317	86.90	0.0003794	4.465

Apparent activation energy was found as Ea = 17 $\pm$ 3 kJ/mol for reaction with sphere-supported catalyst.

Appendix G: Apparent activation energy calculation for MBY hydrogenation

Table G1. Experimental results from cube-supported catalyst.

Exp	T, K	r, $mol_{MBY}/mol_{Pd}/min$	1/(T·R), mol/J	ln r
1	306	125.29	0.0003931	4.831
2	306	106.60	0.0003931	4.669
3	310	151.32	0.0003880	5.019
4	313	166.14	0.0003843	5.113
5	313	179.94	0.0003843	5.193
6	316	219.21	0.0003806	5.390
7	320	195.15	0.0003759	5.274
8	320	243.21	0.0003759	5.494

LINEST function in Excel was used to determined the slope and its error. Ea = 38 ± 6 kJ/mol for MBY reaction with cube-supported catalyst.

Table G2. Experimental results from sphere-supported catalyst.

Exp	T, K	r, $mol_{MBY}/mol_{Pd}/min$	1/(T·R), mol/J	ln r
1	303	709.83	0.0003970	6.565
2	303	673.15	0.0003970	6.512
3	308	888.80	0.0003905	6.790
4	308	817.01	0.0003905	6.706
5	313	997.88	0.0003843	6.906
6	316	1046.58	0.0003806	6.953
7	316	989.40	0.0003806	6.897

Ea = 24 ± 3 kJ/mol for MBY reaction with sphere-supported catalyst.